SPACE INFRARED TELESCOPE FACILITY
WIDE FIELD AND DIFFRACTION LIMITED ARRAY CAMERA
(IRAC)

Grant NAG2-316

Final Report

For the period 1 September 1984 through 31 October 1987

Principal Investigator

Dr. Giovanni G. Fazio

April 1988

Prepared for
National Aeronautics and Space Administration
Ames Research Center
Moffett Field, California 94035

Smithsonian Institution
Astrophysical Observatory
Cambridge, Massachusetts 02138

The Smithsonian Astrophysical Observatory
is a member of the
Harvard-Smithsonian Center for Astrophysics

The NASA Technical Officer for this grant is Mr. Ruben Ramos, Mail Code 244-15, National Aeronautics and Space Administration – Ames Research Center, Moffett Field, California 94035

ABSTRACT

This is the final report under Grant NAG2-316 "A Wide-Field and Diffraction-Limited Array Camera (IRAC)," Dr. Giovanni Fazio, Principal Investigator. The camera is capable of two-dimensional photometry in either a wide-field (5 arcminute field of view) or diffraction-limited (1.25 arcminute field of view) mode over the wavelength range from 2 to 30μm with a possible extension to 120μm. Under this grant the Smithsonian Astrophysical Observatory (SAO), in conjunction with the Ames Research Center (ARC), Goddard Space Flight Center (GSFC), the University of Arizona (UA), and the University of Rochester (UR), with support from Santa Barbara Research Center (SBRC), developed a new "low-doped" indium antimonide detector for 1.8$-$5.0μm, tested and optimized detectors for the entire 1.8$-$30μm range, developed and tested beamsplitters for the 1.8$-$30μm range, and performed tradeoff studies of the camera's optical system.

This report presents data on the performance of InSb, Si:In, Si:Ga, and Si:Sb array detectors bump-bonded to a multiplexed CMOS readout chip of the source-follower type (SBRC's CRC-228) at SIRTF operating backgrounds ($\leq 1 \times 10^8$ ph/cm^2/sec) and temperatures (4$-$12°K). Some results at higher temperatures are also presented for comparison to SIRTF temperature results. Data are also presented on the performance of IRAC beamsplitters at room temperature at both 0° and 45° angle of incidence and on the performance of the all-reflecting optical system baselined for the camera.

CONTENTS

CONTENTS (Cont.)

FIGURES

CONTENTS (Cont.)

CONTENTS (Cont.)

TABLES

SPACE INFRARED TELESCOPE FACILITY
WIDE FIELD AND DIFFRACTION LIMITED INFRARED ARRAY CAMERA
(IRAC)

Smithsonian Astrophysical Observatory
Goddard Space Flight Center
Ames Research Center
University of Arizona
University of Rochester

FINAL REPORT
for the period
1 September 1984 through 31 October 1987
Grant NAG2-316

1.0 INTRODUCTION

This final report is submitted in accordance with the requirements of Grant NAG2-316 for technology development in support of a "Wide-Field and Diffraction-Limited Array Camera" for SIRTF. The camera is capable of two-dimensional photometry in either a wide-field (5 arcminute field of view) or diffraction-limited (1.25 arcminute field of view) mode in three bands over the wavelength range from 1.8 to 30μm with the possible addition of a fourth band from 60 to 120μm.

The camera will be applied to a number of fundamental scientific problems, most of which cannot be addressed in any other way. Two of the most important are galaxy formation during the early stages of the Universe and the search for the "missing mass" in galactic halos. These would provide an important advance in our understanding of the formation and dynamics of galaxies and of the total mass density in the Universe. Other scientific goals include determining the nature of the energy sources in active galactic nuclei and measuring the properties of clusters of galaxies, understanding star formation processes and evolution, both in our galaxy and nearby galaxies, observing the late stages of stellar evolution, determining the abundance distribution of heavy elements in our galaxy and in nearby galaxies, dust around stars, and studying the distribution of dust and gases in comets. The camera will also be applied to follow-up studies on IRAS sources and be used to assess the optical performance and operational characteristics of the SIRTF telescope and spacecraft platform.

The goals of this research were to 1) Develop an improved InSb array detector for Band I (1.8$-$5.3μm); 2) Evaluate the performance of existing array

detectors under SIRTF backgrounds ($\leq 1 \times 10^8$ ph/cm^2/sec) and temperatures (4°–12°K) in all three bands; 3) Optimize the operation of the arrays in all three bands by the adjustment of parameters such as bias points, operating temperatures and clocking methods; 4) Demonstrate that SIRTF performance specifications, particularly read noise and dark current, could be met; 5) Develop and evaluate the performance of infrared beamsplitters for the IRAC instrument; and 6) Prepare a preliminary optical analysis for the camera.

For Band I, two detector materials, Si:In and InSb, were evaluated. The Si:In detector array was a standard Hughes-Carlsbad product. The InSb detectors were of both standard (1.1×10^{15}/cm^3) and reduced (1.7×10^{14}/cm^3) doping concentration. Standard-doped detectors were available from a standard SBRC product line; the "low-doped" detectors were fabricated by SBRC under this research program. "Low-doped" InSb was evaluated because it promised a factor of two reduction in detector capacitance and, hence, a factor of two improvement in read noise over normal InSb. While standard InSb has proven disappointing when operated below 50°, the low-doped InSb program has yielded arrays with promising performance. At 8°K exceptionally low (aA level) dark currents were demonstrated and the anticipated factor of two improvement in read noise achieved.

For Band II (5.3–14μm) and Band III (14–30μm), Si:Ga and Si:Sb detectors were chosen for evaluation respectively. These were developed under earlier programs. Excellent results, results very close to and in some cases exceeding initial SIRTF/IRAC performance requirements, have been achieved with these arrays, although concern remains about their behavior in the radiation environment of space.

The readout system for the detector arrays was the SBRC CRC-228 direct readout (DRO) n-channel multiplexer, a 58 × 62 pixel readout array with 76μm source-follower unit cells which allow random access to any of the 3,596 pixels in the array. One of these hybridized arrays is shown in Figure 1-1.

A simplified diagram of the multiplexer circuit is shown in Figure 1-2. Seven row and seven column address lines plus other control signals allow random access to the 1,798 detector pairs ("unit cells") within the array. The array is read out in parallel as two interlaced 58 × 31 subarrays, each with its own readout source-follower circuit. Sampling can be performed with or without the application of a software-controllable reset pulse, allowing either destructive or non-destructive readout (NDRO).

The Infrared Array Camera must reimage the infrared sky in three bands simultaneously. A pair of wideband dichroic beamsplitters operating in series reflect energy in the first band (1.8–5.3μm, Beamsplitter 1) then in the second band (5.3–14.0μm, Beamsplitter 2) while passing energy in the third band (14–30μm). Both beamsplitters require wide-band multilayer coatings and presented a technological challenge in the development of the instrument. As a result of this research,

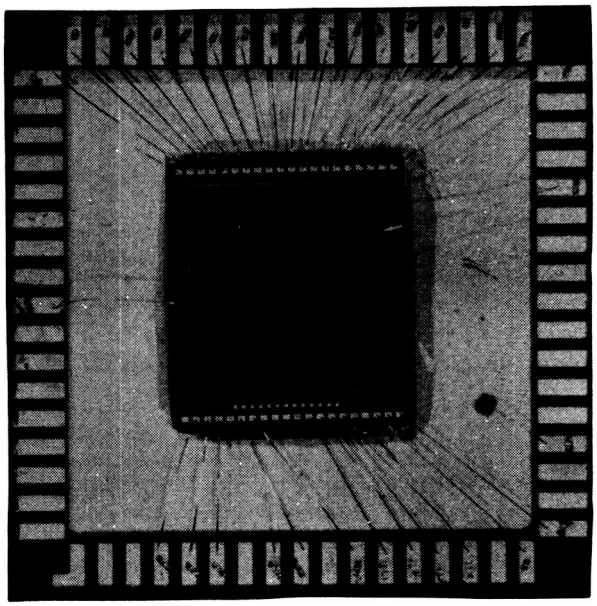

Figure 1–1. 58 × 62 DRO Infrared Detector Array

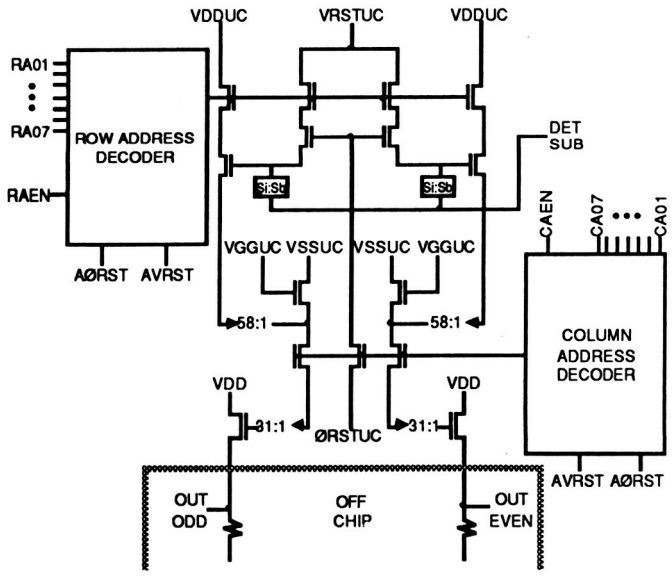

Figure 1–2. Schematic Diagram of Multiplexer Unit Cell

the technology for these beamsplitters can now be said to be well in hand.

Beamsplitter goals for the IRAC instrument were developed in conjunction with the Optical Coating Laboratory, Inc. (OCLI), Santa Rosa, California. OCLI subsequently fabricated and tested one set of multilayer coated beamsplitters on cadmium telluride (CdTe) substrates which were further tested at the University of Arizona.

Optical constraints imposed on the camera by IRAC scientific requirements include the necessity of independent wide-field (5.0 arcmin FOV) and diffraction-limited (1.25 arcmin FOV) modes and a resolution in both modes better than 75μm, with the system operating at less than 10° kelvin. Although no new technology will be required to meet the optical or thermal constraints, the camera will test the state of the art. Accordingly, optical analyses were undertaken as a part of this research to identify areas of concern and to select the optimum optical configuration.

Optical design requirements and tradeoff parameters were established jointly by SAO, UA and GSFC. Refractive-reflective and all-reflective optical designs were considered. An all-reflective design was selected for the baseline optical system because of the freedom from chromatic aberration it provides.

Development of hardware and software to test the arrays at SIRTF backgrounds and temperatures in support of this research constituted an important part of this effort. Although equipment details differ, the facilities at ARC, GSFC and UR are similar in purpose and design. Each consists of a dewar capable of operating at LN_2 and LHe temperatures to cool the array under test and flood it with IR through a selection of filters. Read and drive circuits interface the array with the computer systems to control the array and read out data. These systems implement a wide range of signal processing modes and clocking schemes, provide for NDRO capability and direct addressing of pixel pairs, provide direct control of the test conditions and record, process and display image data in a variety of formats.

The Smithsonian Astrophysical Observatory (SAO), with Dr. Giovanni Fazio as Principal Investigator, held overall responsibility for performance under the Grant, provided scientific direction, program management and support to SIRTF project activities, including the SIRTF Science Working Group (SWG). Dr. Judith Pipher at the University of Rochester (UR) tested and evaluated the InSb and Si:In Band I arrays. Mr. Gerald Lamb (Co-I) of Goddard Space Flight Center (GSFC) tested the Si:Ga Band II array initially and Dr. Craig McCreight (Co-I) at Ames Research Center (ARC) repeated and extended the tests later. Dr. McCreight also tested and evaluated the Si:Sb array for Band III. Dr. William Hoffmann (Co-I) of the University of Arizona (UA) tested and evaluated the OCLI beamsplitters and collaborated with GSFC in developing and evaluating optical designs for the camera. Optical design work at GSFC was carried out by Mr. Peter Maymon.

Dr. Daniel Gezari (Co-I) was Instrument Scientist during this period. Work at SBRC was the responsibility of, in order, Dr. B. T. Yang, Mr. Donald Campbell, Ms. Mary Hewitt and Mr. Robert Feitt.

This report summarizes the results of this research. Detailed results are available in the references.

2.0 INSTRUMENT DESCRIPTION

The Infrared Array Camera images the sky on solid-state array detectors in three bands which are nominally, Band I: 1.8−5.3μm, Band II: 5.3 − 14μm, and Band III: 14−30μm. A fourth band of 60−120μm is under consideration. Beamsplitters provide simultaneous viewing in each of these bands. The camera operates at two magnifications one of which provides diffraction-limited imaging and the other optimized wide-field imaging. A magnification change mechanism moves the appropriate optical elements to change the plate scale at the detectors and filter wheels provide a selection of infrared filters in each band.

The major elements of the IRAC are the Optical/Mechanical Subsystem, the Thermal Subsystem, the Calibration Subsystem, the Focal Plane Array Detector (FPAD) Subsystem, the Instrument Control and Data Processor (ICDP) Subsystem, and the Power Subsystem (Figure 2-1).*

The Optical/Mechanical Subsystem consists of all optical elements, the optical bench, and related mechanisms. A schematic of the optical subsystem may be found in Figure 2-2. All of these elements are mounted on a common optical bench which is bolted directly to the SIRTF Multiple Instrument Chamber (MIC) reference mounting interface. IRAC is assigned one 120° sector of the MIC and will utilize a single position on the SIRTF tertiary mirror.

The Thermal Subsystem includes all temperature control surfaces and materials, heaters and related control electronics.

The Calibration Subsystem contains all infrared reference sources, their power supplies and their control circuits. Internal calibrators will be provided for array detector flat fielding and radiometric calibration.

The FPAD Subsystem includes the detector arrays for each wavelength band; associated power supplies; drive electronics, read electronics, and A/D converters; and the cryogenic, mechanical, thermal and electrical interfaces with the instrument. In order to assume optimal thermal control of the detector arrays, they will be mounted directly to the independently-accessible 2°K and 7°K stations in the MIC. Independent thermal control can be applied directly to each detector assembly if necessary. Arrays in all three bands are baselined to use 75μm pixels. Band I will have 128 × 128 elements; Bands II and III 64 × 64 elements. Signal buffers will be required to drive the signal cable between the cold array and warm electronics circuits. These buffers will be attached to the 7°K station. Low-doped InSb detectors are baselined in Band I; Si:Ga and Si:Sb in Bands II and III

*Figures and text in this section are current to the date this report was prepared.

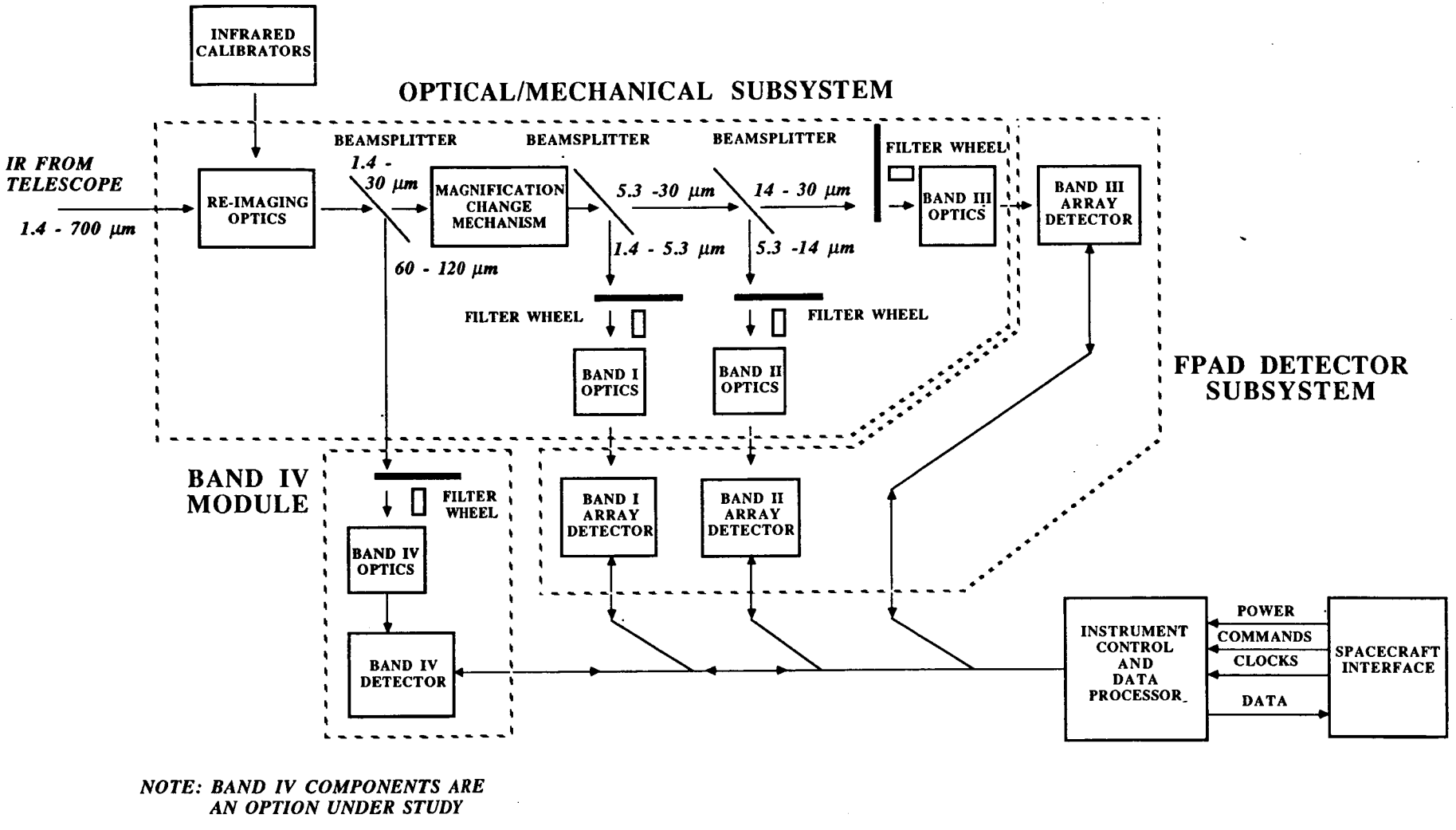

Figure 2- 1. Infrared Array Camera Functional Block Diagram

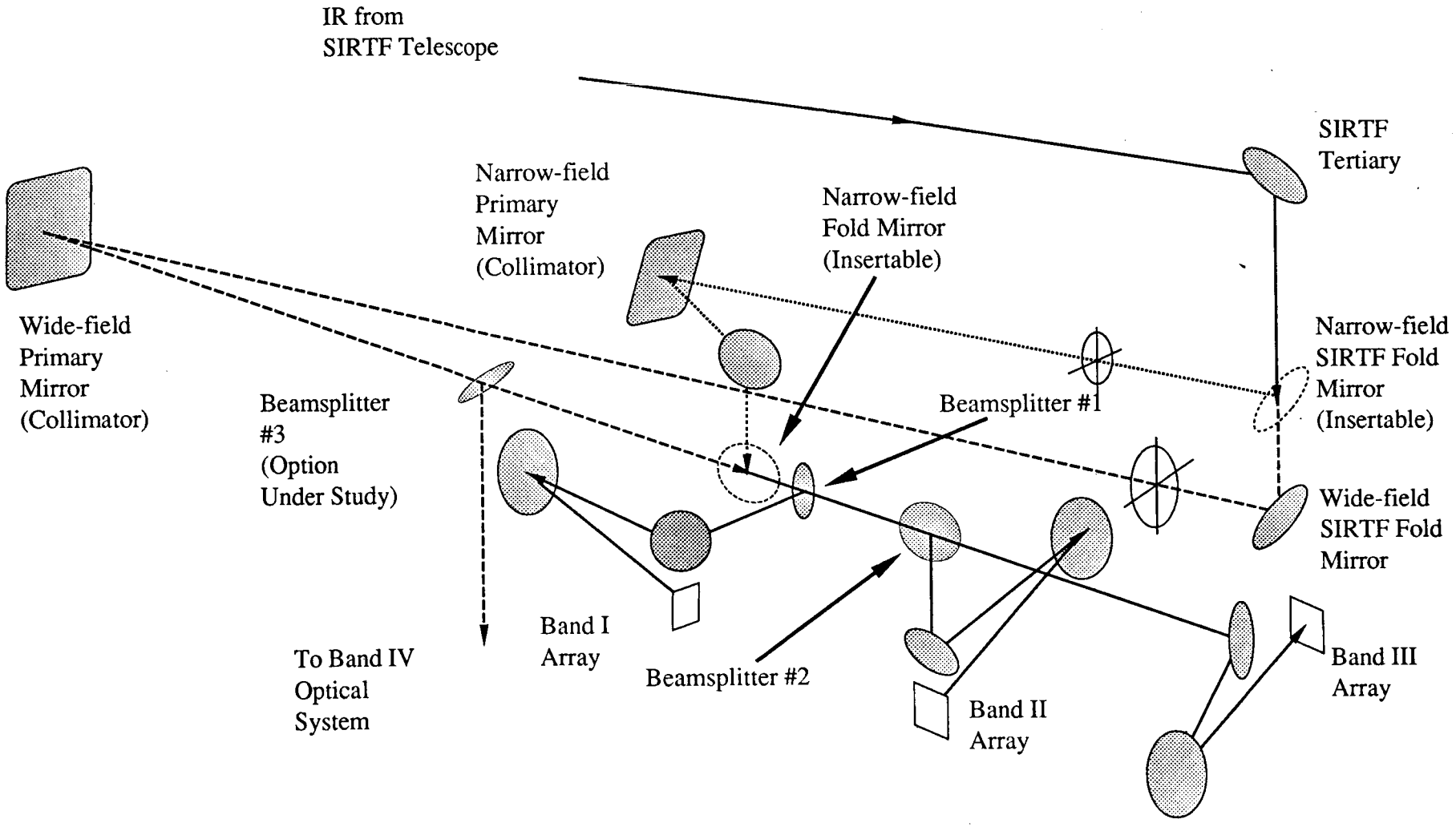

Figure 2–2

SPACE INFRARED TELESCOPE
FACILITY
INFRARED ARRAY CAMERA

OPTICAL SCHEMATIC

KEY

Wide-field Mode Only
Narrow-field Mode Only
Both Modes

respectively.

The ICDP Subsystem consists of all instrument control and mode change logic, command and telemetry formatting circuits and spacecraft interfaces, data accumulators, data processors, housekeeping monitors, and FPAD control circuits and interfaces. The ICDP will provide control signals to the FPAD in the form of read enable and address commands, gain settings, and regulated power supply voltages and take data in the form of digital signal level words. All data processing, data formatting and mode control will be handled by the ICDP. A digital interface is baselined between the FPAD Subsystem and the ICDP Subsystem.

The Power Subsystem conditions spacecraft power and supplies filtered power to the rest of the instrument.

3.0 BAND I ARRAY DETECTOR RESEARCH

3.1 Introduction

Santa Barbara Research Center fabricated and tested both standard-doped and low-doped InSb arrays and Hughes-Carlsbad provided a Si:In array, all of which were subsequently tested at the University of Rochester. This section summarizes SBRC and UR test results and discusses work on detector capacitance measurement, QE variation across the arrays and evaluation of alternate clocking schemes carried out at UR as a part of the test program.

One standard-doped InSb array, two low-doped InSb arrays and one Si:In array were tested and characterized by UR. SBRC tested a total of four low-doped InSb arrays. The standard-doped InSb array and one low-doped InSb array were procured under separate funding. These arrays have a useful wavelength range of $1.8-5.3\mu m$ and a peak response at $3.5\mu m$. Tests were performed over a range of temperatures to evaluate the performance of the arrays parametrically in a search for the optimum operating conditions. Summary data from tests run at both SBRC and UR are presented in Table 3-1.

3.2 Summary of Test Results

3.2.1 Standard-Doped InSb Array FPA17

The standard-doped InSb array (FPA17) was tested at 51°K, 47°K, 41°K, 36°K, and 8°K to explore array performance as a function of temperature[1]. Operating at 40°K, FPA17 had a read noise of 900 e^- and a dark current of 100 aA. Quantum efficiency varied widely across the array from 0.4 to 33% in a manner suggestive of the unexplained dramatic low temperature falloff in QE seen in some standard- and low-doped InSb arrays and described by SBRC[2] and others. At 8°K, this array showed the impressive drop in dark current expected at the lower operating temperature. The dark current was measured to be 5 aA at 8°K; read noise was 600 e^-. Unfortunately QE also dropped dramatically to $0.2-2\%$ across the array.

Histograms of quantum efficiency, dark current and read noise for the device are shown in Figure 3-1. The zero bias capacitance for the device is assumed to be 1pF; at 150mV bias, the capacitance is taken to be 0.77pF.

Figure 3-2 shows the variation in quantum efficiency across the array at three temperatures, 51°K, 41°K, and 8°K, and clearly demonstrates the extreme falloff seen as the temperature is lowered.

Array Designator:	FPA17		SCA001			SCA002		
Type:	Standard InSb		Low-doped InSb			Low-doped InSb		
Tested by:	Rochester	Rochester	SBRC	Rochester	Rochester	SBRC	Rochester	Rochester
Test Temperature (°K)	~40	8	<10	31	8	<10	6 - 7	10
Dark Current (aA)	100	5	36	<30*	---	2100	0.2	---
Read Noise (e-)	900	600	---	600	---	392	200 - 300	200 - 300
Detector Capacitance (pF)	1.0	1.0	0.53	0.63	0.55	0.57	0.55	0.55
Quantum Efficiency (%)	0.4 - 33	0.25 - 2.0	56	25 - 68	2 - 40	42	---	28 - 40
Operability (%)	---	---	>98	---	---	>98	---	---
NEP (Watts/Root-Hz))	---	---	2.20E-17	---	---	1.50E-17	---	---
Responsivity Uniformity (%)	---	---	56	---	---	38	---	---
Well Size (e-)	---	---	1.50E+05	---	---	>1.5E+05	---	---
AR Coated	No	No	No	No	No	No	No	No

Array Designator:	RH2		RH4	W12			IRD	Contract
Type:	Low-doped InSb		Low-doped InSb	Si:In (2 V bias)	(2 V bias)	(-55.9V bias)	Req'mt	Goals
Tested by:	SBRC	SBRC	SBRC	Rochester	Rochester	Rochester	(SAO)	(SAO)
Test Temperature (°K)	7 - 10	15	7 - 10	30	8	8	<10	<10
Dark Current (aA)	6.5	44.5	6.0	15	0.5	---	<1.6	25 max.
Read Noise (e-)	346	480	329	150	60	---	<10	100 max.
Detector Capacitance (pF)	0.65	0.65	0.65	0.07#	0.07#	0.07#	---	---
Quantum Efficiency (%)	51	77.3	51	1.06	0.11	5.1	60 min.	60 min.
Operability (%)	>97	---	>98	---	---	---	99.5 min.	85 min.
NEP (Watts/Root-Hz))	5.06E-18	4.00E-18	3.29E-18	---	---	---	---	---
Responsivity Uniformity (%)	37	---	---	21	---	---	5% max	20% max
Well Size (e-)	>1.5E+05	1.47E+06	>1.5E+05	---	---	---	>5E+05	>1E+05
AR Coated	Yes	Yes	Yes	No	No	No	---	---

Table 3–1. Band I Array Test Data and Design Goals

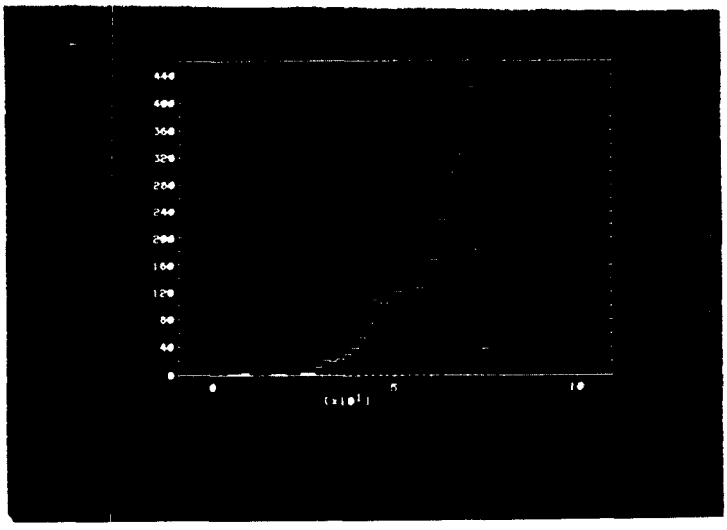

(a) Histogram of quantum efficiency measurements for FPA 17. T = 51K; looking at a 295K blackbody, through a 3.3 μm filter. VBIAS = 150 mV; VGATE = -2.5 V. Pixels at left are dead. Quantum efficiency in %.

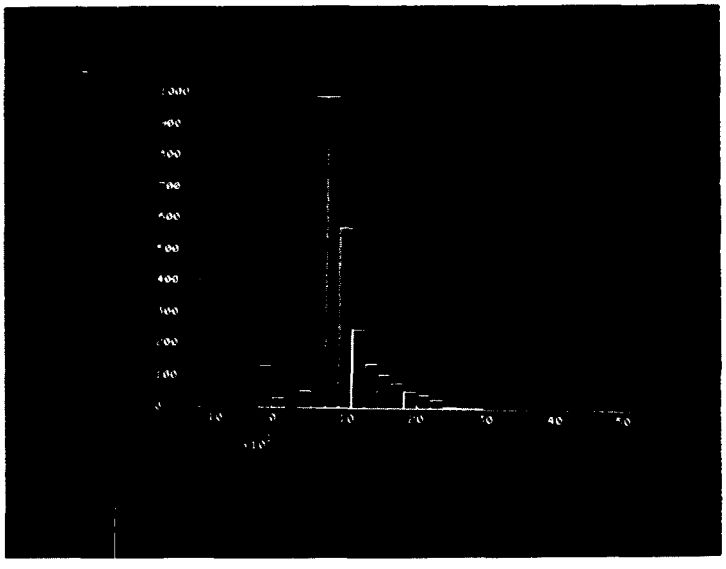

(b) Histogram of dark current, at 8K on FPA 17. Other parameters include VGATE = -2.5 V, VBIAS = 150 mV, 36 microsec/pixel pair read rate. Dark current in electrons/sec. Pixels at left are dead.

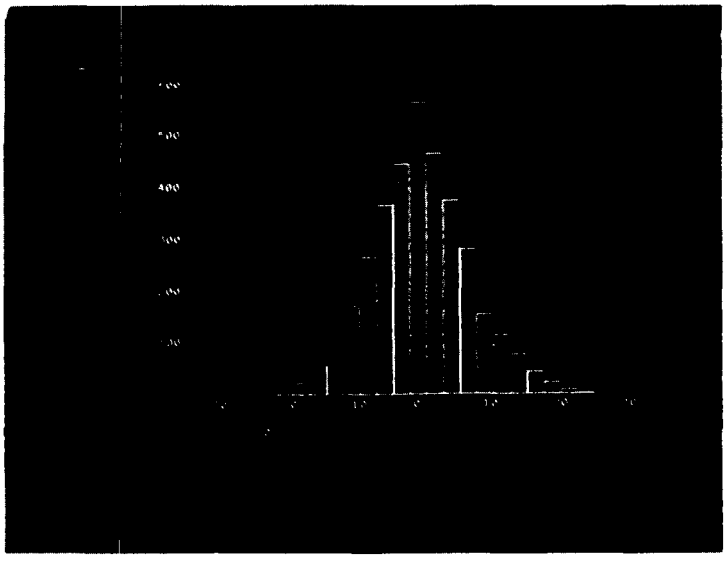

(c) Histogram of two subtracted CDS frames, in electrons, on FPA 17. T = 8K, VGATE = -2.5 V; VBIAS = 150 mV. RMS Noise is given by HWHM/$\sqrt{2}$.

Figure 3-1. Histograms of Quantum Efficiency, Dark Current and Read Noise for FPA17

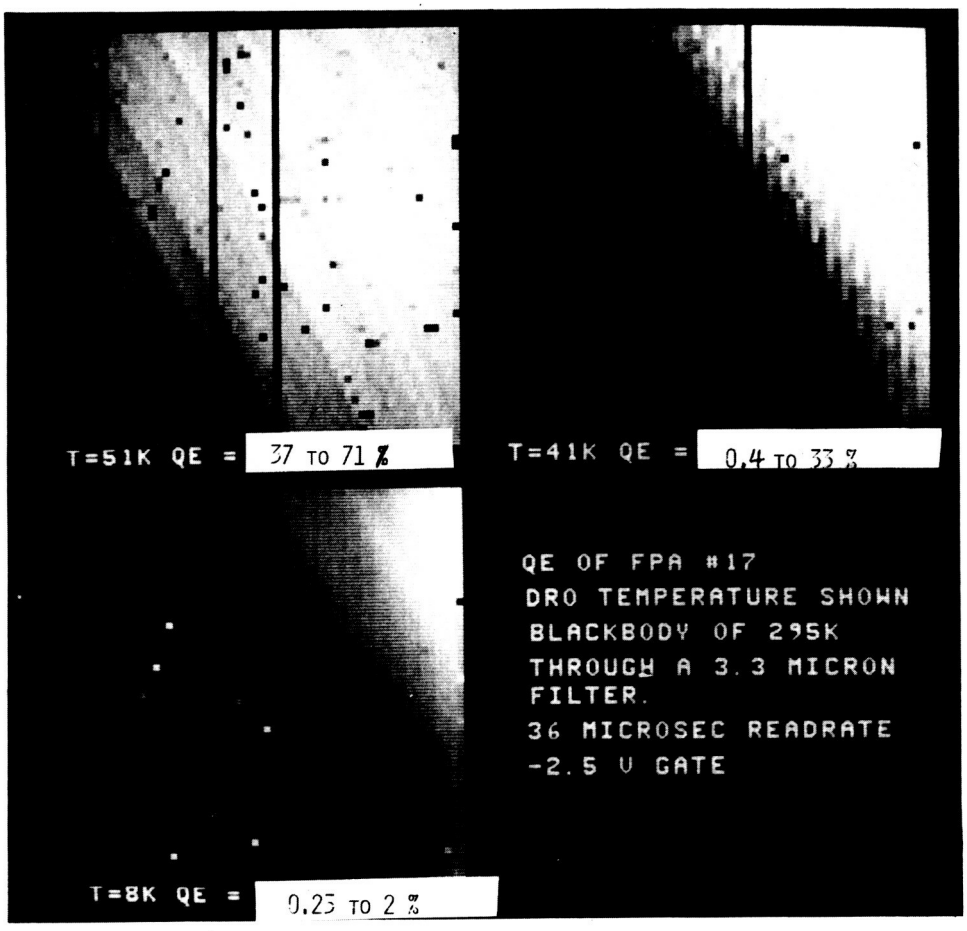

Figure 3–2. FPA17 Variation of Quantum Efficiency

The dark current variation across FPA17 at 4°K is shown in Figure 3-3. The upper left-hand image is the result of a 240-second exposure to a cold dark slide (CDS) at 150mV bias. The upper right-hand image is the result of exposing the array to the same dark side for one-twelfth of a second. Differencing the two yields a dark current display with instrumental effects removed (lower left). Note that the dark current is higher by a factor of three along the lower left and lower right edges relative to the center. At 50mV bias, the dark current shows further randomization as shown in the lower right-hand image.

Noise on FPA17 is shown in Figure 3-4. The left-hand figure is a typical frame taken at 3.3μm and 51°K. Subtraction of two consecutive 3.3μm exposures results in the image of the upper right indicating uniform noise properties across the array.

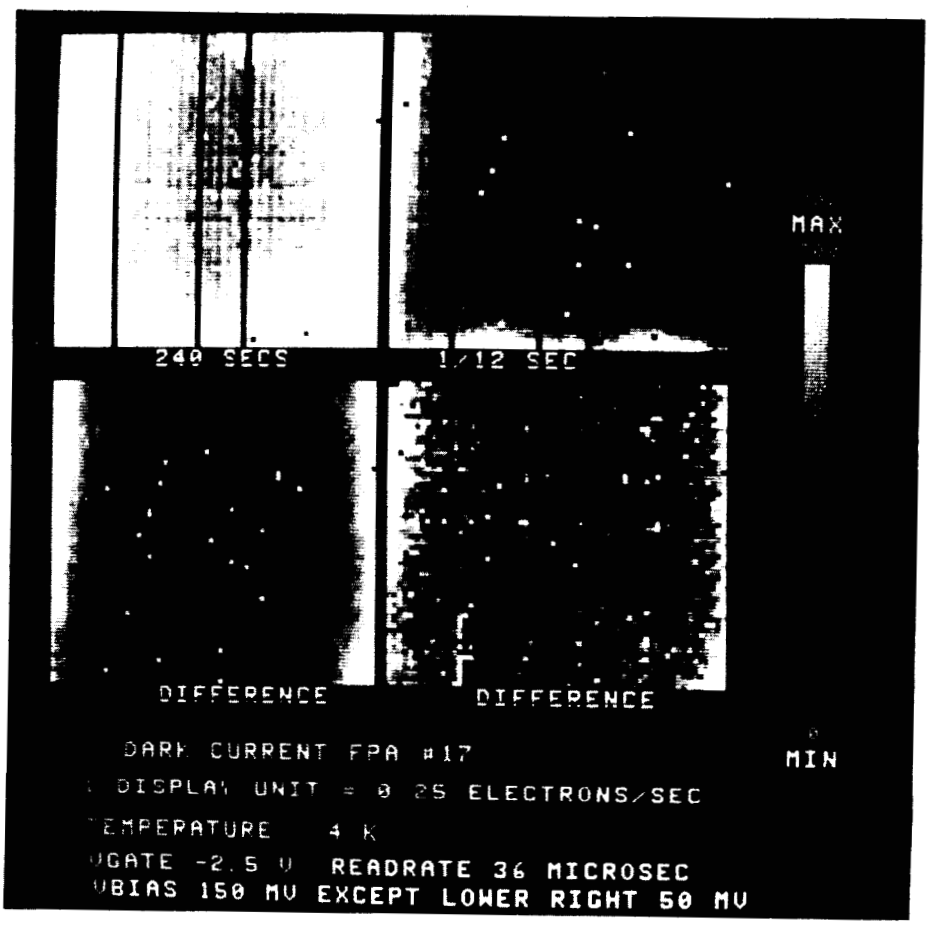

Figure 3–3. Dark Current of FPA 17

Figure 3–4. Noise on FPA 17 at 3.3μm and 51°K

3.2.2 Low-Doped InSb Array SCA001

SCA001, the first of the two low-doped InSb arrays studied[3] was operated at 31°K with a measured read noise of 600 e^-, a dark current of 30 aA, across the central portion of the array, and QE's of 25–68% across the array. The histograms taken in this array are shown in Figure 3-5. All values are based on a calculated detector capacitance of 0.63pF, the value appropriate for operation above freeze-out which occurs between 20°–30°K. Below freeze-out, the proper value is 0.55pF. (See Section 3.3, below.) At 8°K, the QE dropped to 2–40% across the array. The dark current was highest on the lower right portion of the array (Figure 3-6), a characteristic also noted by SBRC.[2] A secondary "hot spot," one not observed by SBRC, was also seen in the upper left portion of the array. The hot spot in the lower right portion of the array is due to the relatively high power output MOSFETs located near that area. When VDD is decreased from 5V to 1V the resultant dark current in that corner decreases. This effect was ultimately determined to be caused by a dewar wiring error, not by a malfunctioning array.

Also seen are small undulations on top of and parallel to the gross variation which are referred to as "tree rings." The gross variations may be due to a carrier lifetime or mobility problem in the high-doped InSb, and the "tree rings" due to variations in the doping.

Read noise distribution across SCA001 may be seen in Figure 3-8. Note how readouts later in time improve, an effect which is not yet fully understood.

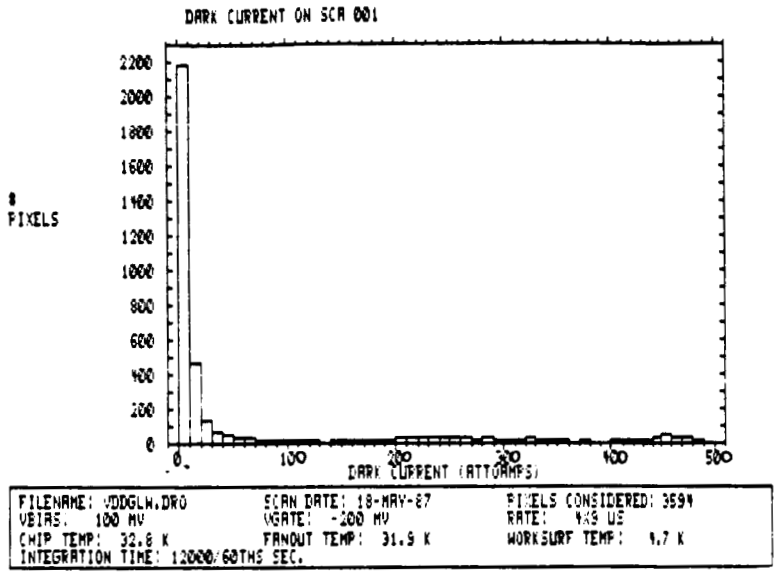

(a) Dark current histogram for SCA001. For the central part of array the mean dark current is 6 aA.

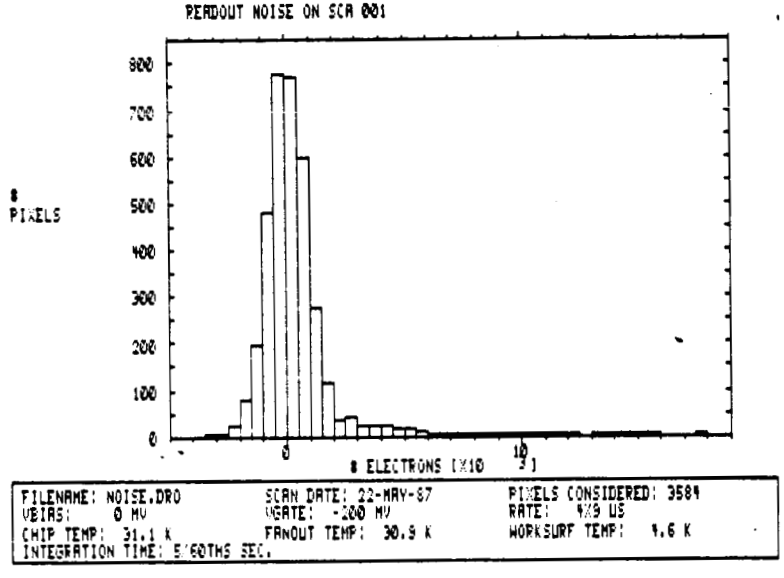

(b) Histogram of the spread in pixel values in a difference of two consecutive readouts of SCA001 at 31K looking at the cold dark slide.

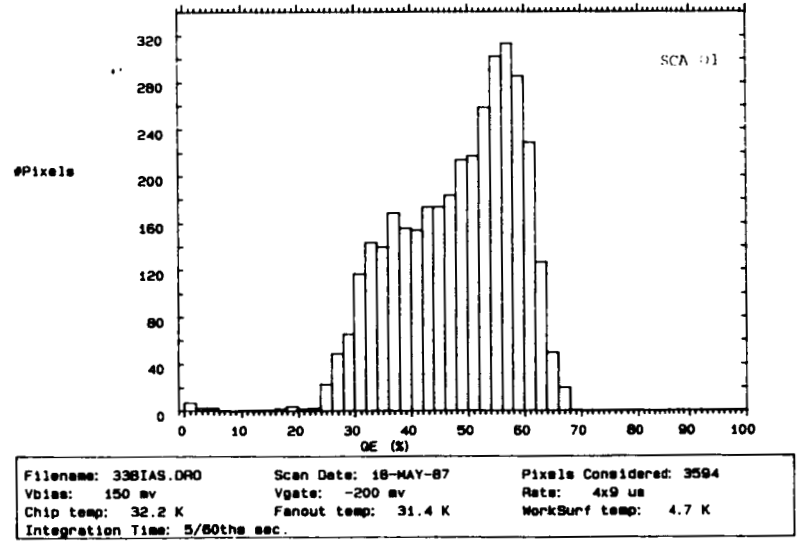

(c) Histogram of quantum efficiency measurements at 31K. Assumed zero bias capacitance was 0.63pF. Illumination through narrow-band 3.3μm filter; room irradiance.

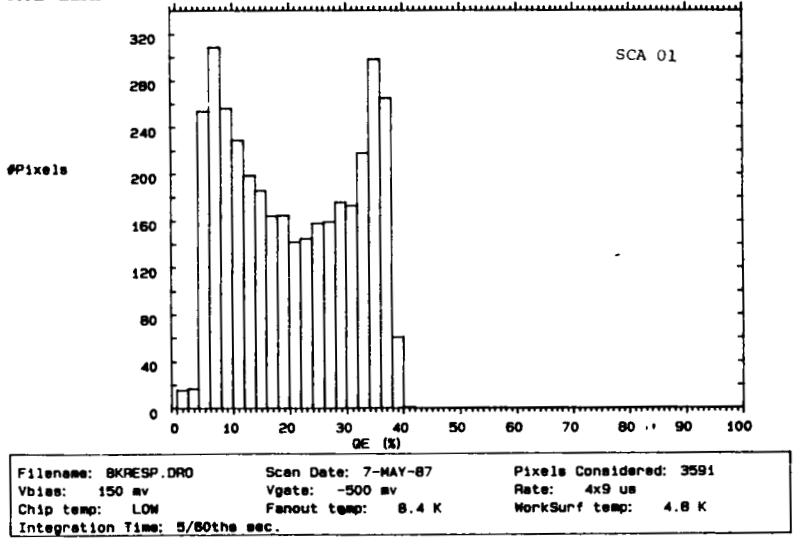

(d) Histogram of quantum efficiency measurements at 8K. Other conditions as above; assumed zero bias capacitance was 0.55pF.

Figure 3-5. Histograms of SCA001 Performance at 4.7°K.

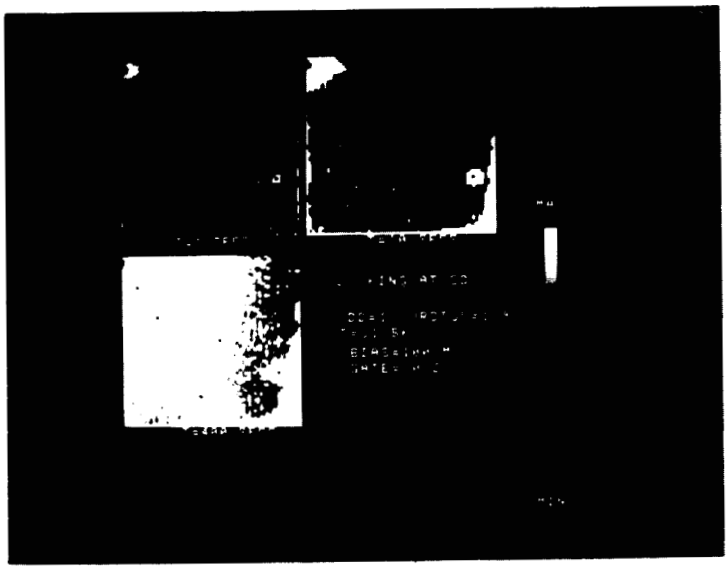

Figure 3–6. Dark Current in SCA001 as a Function of Integration Time

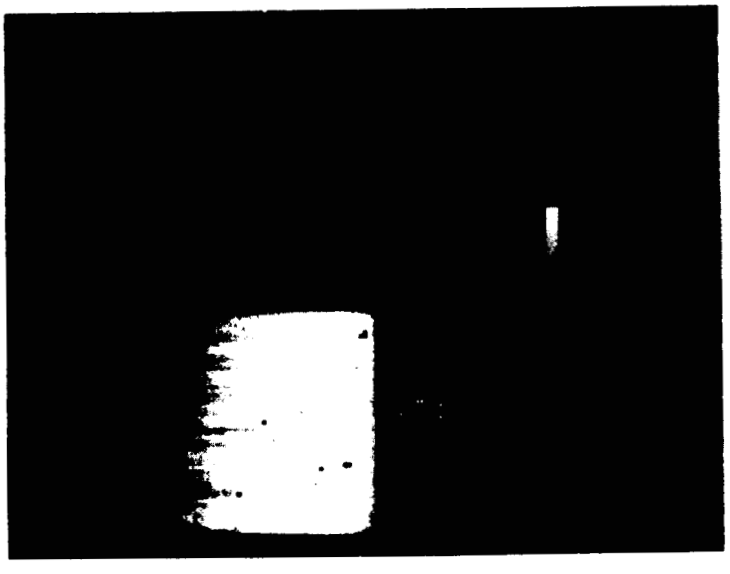

Figure 3–7. Gray Scale Representation of Quantum Efficiency of SCA001

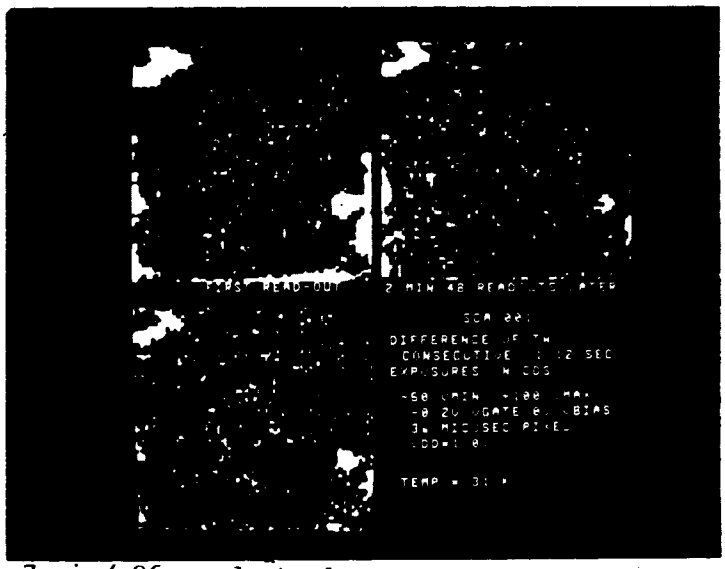

7 min/ 96 readouts later

Figure 3–8. Difference of Two Consecutive Readouts in SCA001 as a Function of Time

3.2.3 Low-Doped InSb Array SCA002

SCA002 has, to date, yielded better results than any of the other Band I arrays tested by UR.[3] Dark current at 6°K is an impressively low 1.3 e^-/s or 0.2 aA. The QE at 10°K is an acceptable 40% in the upper left portion of the array assuming a detector capacitance of 0.55pF. Read noise was 200−300 e^- at both 6−7°K and 10°K and essentially the same from 83 ms to 500 s integration time.

Histograms of quantum efficiency and dark current in SCA002 at 7−10°K may be found in Figure 3-9. Figure 3-10 compares the gray scale representation of quantum efficiency of SCA001 and SCA002. Note that while the tree ring structure is evident in both arrays, SCA002 does not show the extreme falloff across the array evidenced by SCA001.

The gray scale representation of dark current and noise reveals a good degree of uniformity (Figure 3-11) across the array with no hot spots evident.

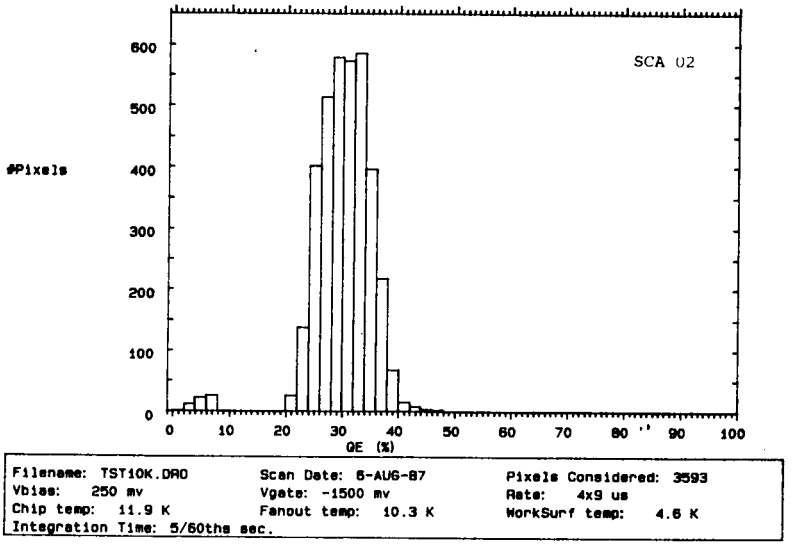

(a) Quantum efficiency of SCA002 at 10K and 3.3μm

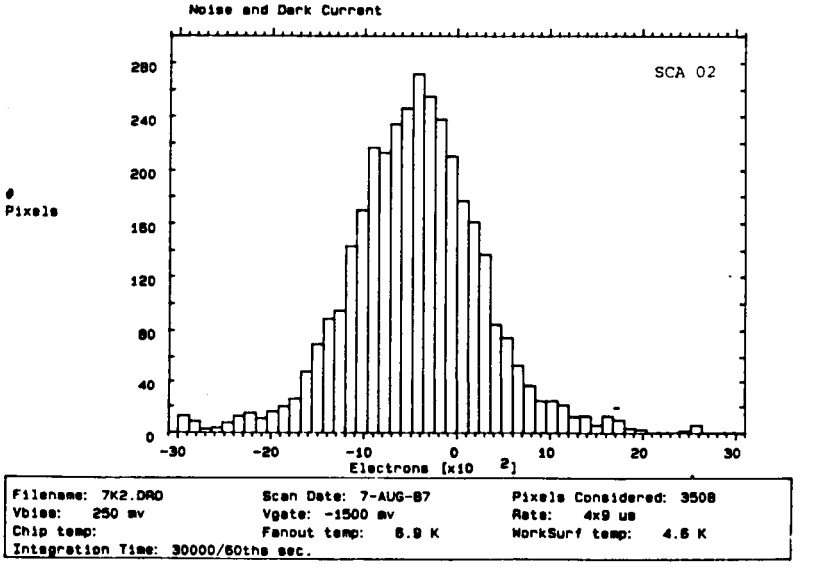

(b) Dark charge in SCA002 after 500 sec. The spread in the measurements corresponds to approximately 300 e^- RMS noise.

Figure 3-9. Histograms of SCA002 Performance at 4.5°K

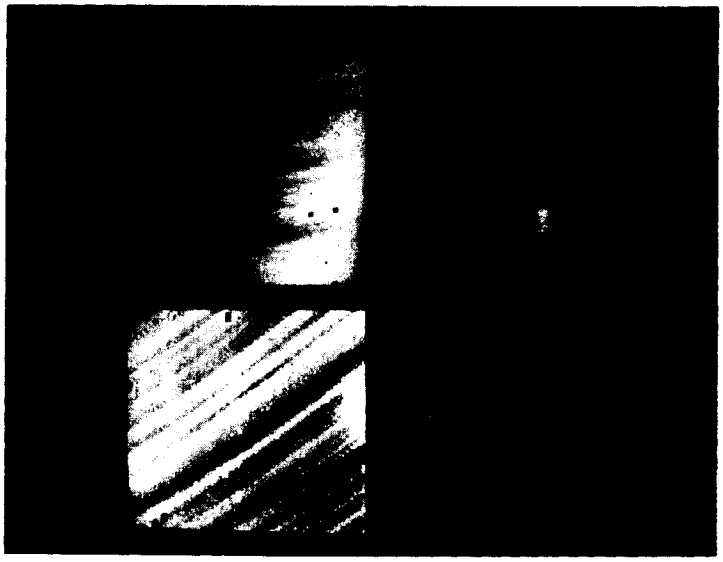

Figure 3–10. Gray Scale Comparison of Quantum Efficiencies of SCA001 and SCA002

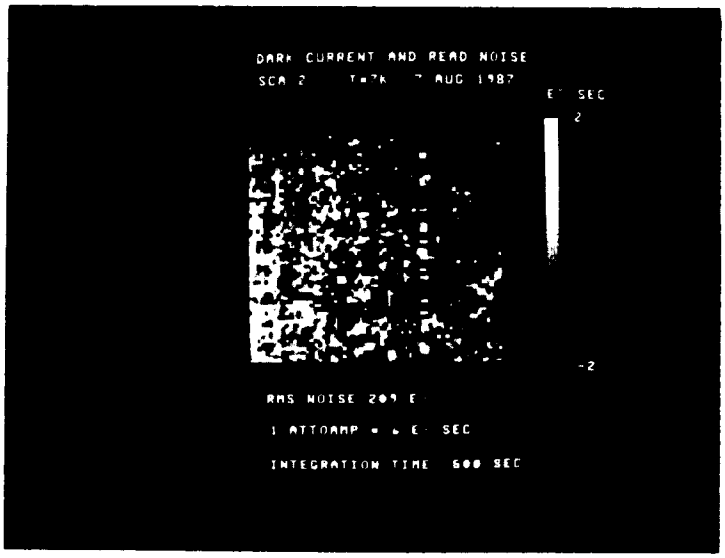

Figure 3–11. Gray Scale Representation of Dark Current/Noise Data

3.2.4 Low-Doped InSb Array RH2

RH2, also a low-doped InSb array, was tested by SBRC[2] prior to delivery. At 10°K the device showed a dark current of 7.33 aA (burst mode) and a read noise of 345 e^- based on an assumed detector capacitance of 0.65pF. (SBRC and UR estimates of detector capacitance differ by approximately 0.1pF, see paragraph 3.3 below.) QE was 47.3% with a sigma of 25% across the array. This array, and RH4, described in the next section, are both AR-coated. Responsivity uniformity was 37% across the array. Operability greater than 97% was achieved. NEP was measured as 4.61×10^{-18} W and the dynamic range was 12.2×10^5 e^-. At 15°K, this array showed the expected significant increases in dark current (to 44.5 aA) and read noise (to 480 e^-). QE also increased significantly to 77.3% (29.3% 1 σ variation) while dynamic range and NEP were little changed from their 10°K values. Histograms supporting these figures are given in Appendix A. Figure 3-12 shows the variation with detector bias of quantum efficiency, NEP, read noise and dark current of RH2. Gray scale photographs of signal response and dark current are shown in Figure 3-13. Signal response shows a "cool" spot in the lower left-hand corner, two column defects of unknown origin and a diagonal defect due, possibly, to a crack in the InSb detector board.

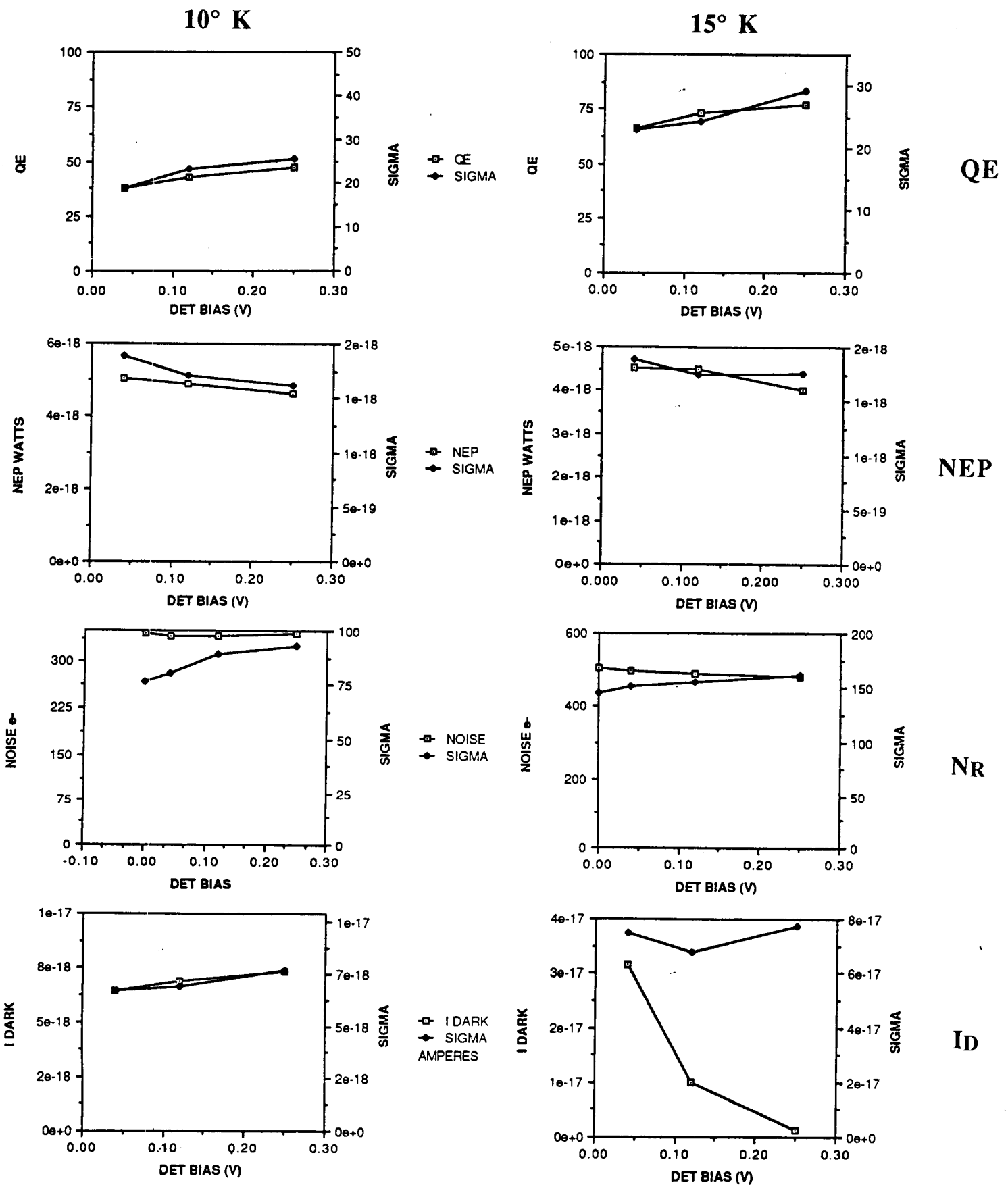

Figure 3-12. Low-Doped InSb Detector RH2 Quantum Efficiency, NEP, Read Noise, and Dark Current as a Function of Detector Bias at 10° K and 15°K

RH2 Signal Response Scale: $\pm 2\sigma$ from the Mean

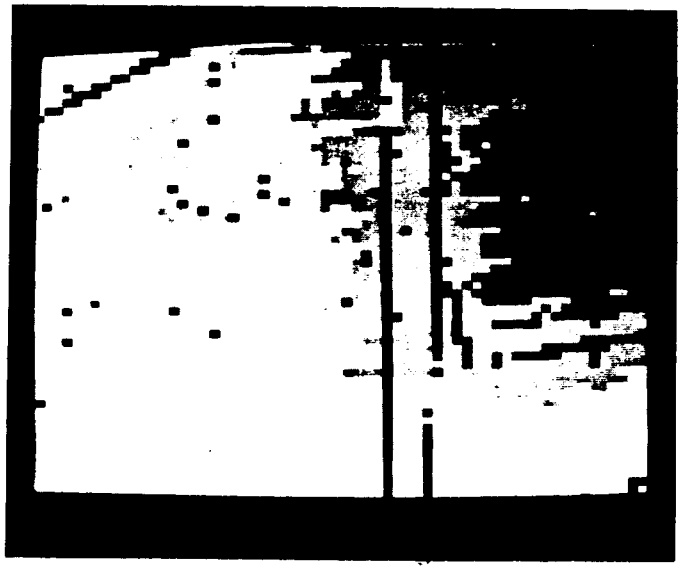

RH2 Dark Current Scale: $\pm 2\sigma$ from the Mean

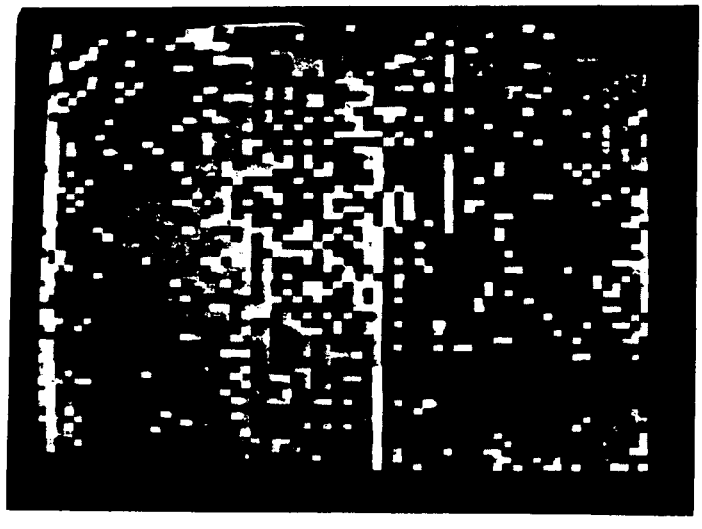

Figure 3-13. RH2 Gray Scale Signal Response and Dark Current

3.2.5 Low-Doped InSb Array RH4

RH4, also low-doped InSb, showed very similar performance to RH2 except that the QE was significantly higher in tests by SBRC[2]: 61.3% (12.6% 1 σ variation) and the responsivity uniformity much better at 21%. Histograms for RH4 are given in Appendix B and the data plotted as a function of detector bias at 10K in Figure 3-14. Dark current (burst mode) is a low 9.34 aA at 0.12V bias, read noise is 331 e^- and NEP is 3.68×10^{-18} at the same point. Quantum efficiencies, NEP, and read noise are remarkably constant as bias is increased from 0.04V to 0.25V. Dark current increases by about 50% over the same range.

Figure 3-15 shows gray scale plots of signal response and dark current. The excellent uniformity seen in the histograms in Appendix B is also clearly shown in the signal response plot in this figure, the only anomaly being a diagonal line of low response across the face of the array which is attributed to a crack in the detector board. Dark current gray scale response is seen to be similarly uniform in the same figure.

Of the low-doped InSb arrays tested under this program, RH4 initially appeared, by far, to be the best array. Unfortunately, the device, in subsequent tests, developed a "salt-and-pepper" appearance due to the development of high dark current in about 500 pixels, the cause of which is unknown. RH2 shows no such behavior, but is far less uniform overall and has a column defect causing the loss of almost two entire columns.

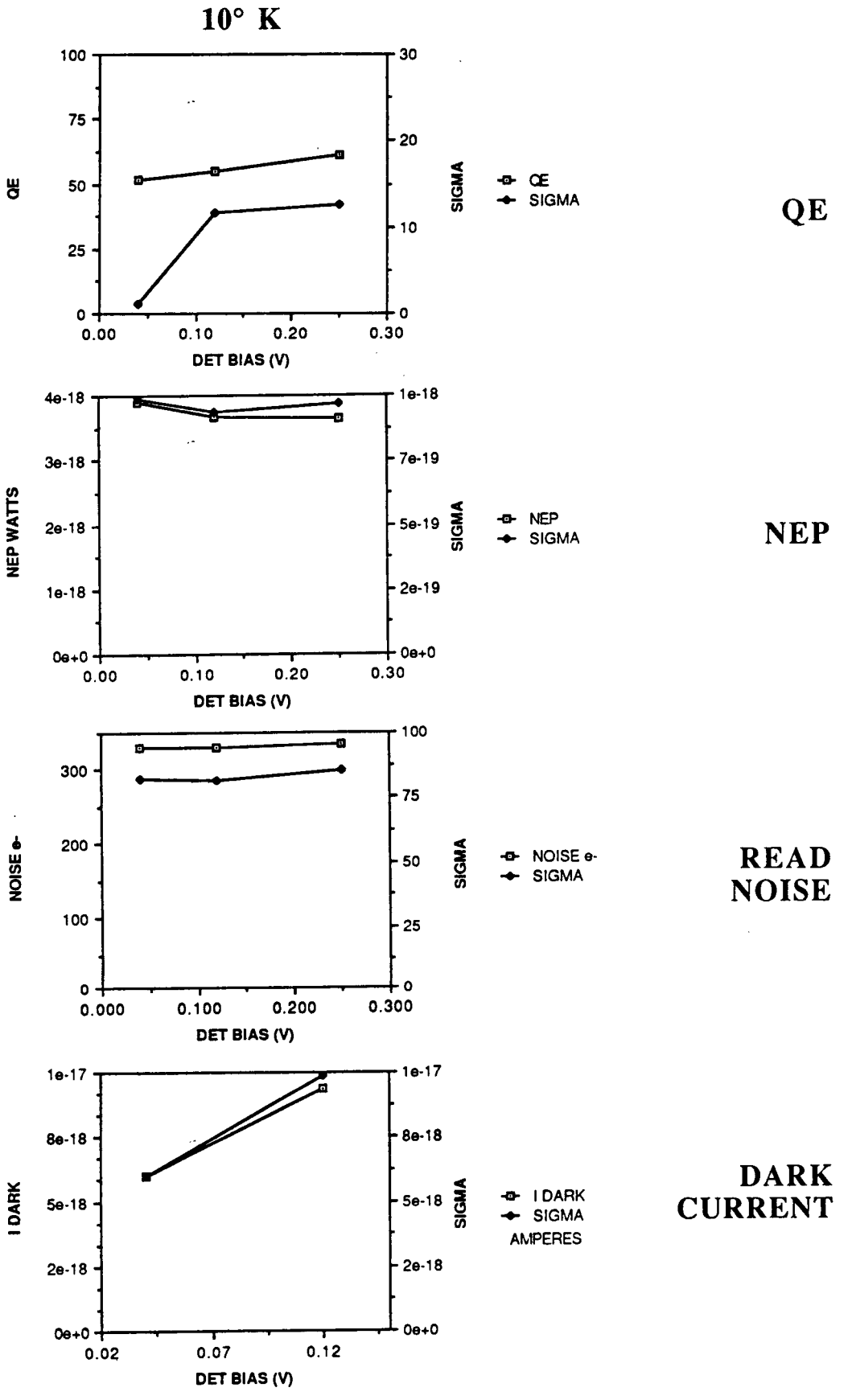

Figure 3-14. Low-Doped InSb Detector RH4 Quantum Efficiency, NEP, Read Noise, and Dark Current as a Function of Detector Bias at 10° K

RH4 Signal Response Scale: $\pm 2\sigma$ from the Mean

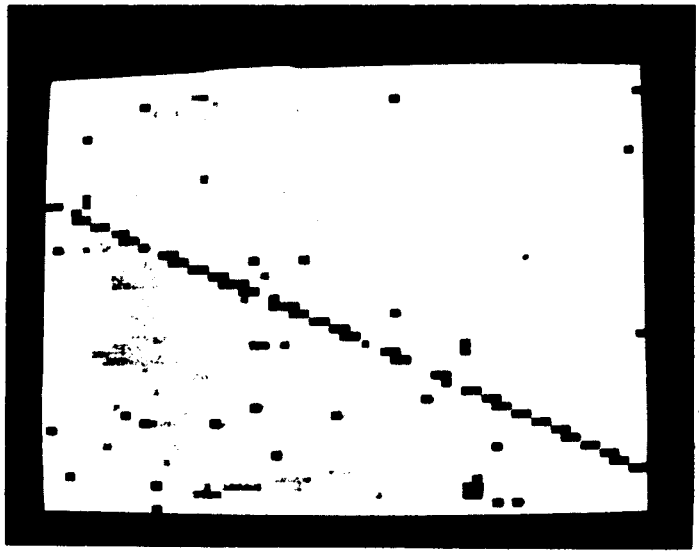

RH4 Dark Current Scale: $\pm 2\sigma$ from the Mean

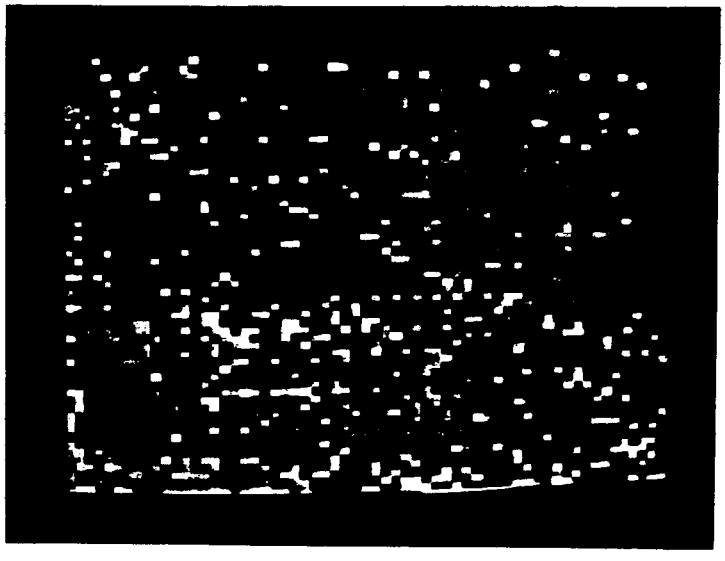

Figure 3-15 RH4 Gray Scale Signal Response and Dark Current

3.2.6 Hughes-Carlsbad Si:In Array

The Si:In array from Hughes-Carlsbad has been tested by UR[3] over the range from 50°K to 8°K and with biases from -55.9V to +4V. At 30°K with a bias of +2V, measurements yielded a dark current of 15 aA, a read noise of 150 e^-, and a quantum efficiency–photoconductive gain product (QExg) of 1.06%. At 8°K and a bias of -55.9V, far closer to the proper operating bias of about 100V, the measurements yielded a dark current of 0.5 aA, a read noise of 60 e^-, and a QExg of 5.1%. While the low dark current and read noise of the Si:In array are very attractive, the low QE and high operating bias are not and further work must be done at higher biases to fully evaluate the performance of this array in the SIRTF application.

The variation in the quantum efficiency–photoconductive gain product for the Si:In array at 13°K is shown in the gray scale representation in Figure 3-16.

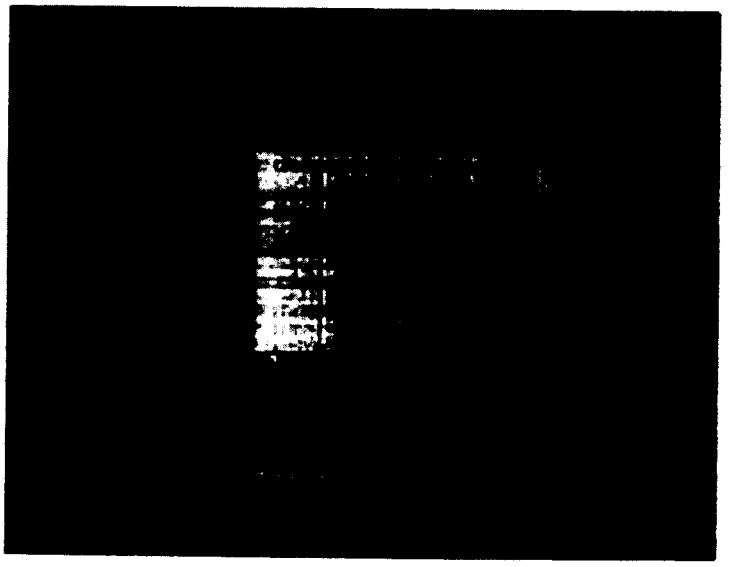

Figure 3–16. Variation in Quantum Efficiency–Photoconductive Gain Product in Si:In Array at 13°K.

3.3 Low-Doped InSb Detector Capacitance Measurements

UR developed estimates for the various components which comprise the total detector capacitance in InSb:[2] zero bias diode capacitance, sense node (DRO gate node) capacitance and gate overlap capacitance, based on a combination of calculated and measured data. The diode capacitance varies inversely with the square root of applied bias; the sense node capacitance and gate overlap capacitance are fixed capacitances. The estimates in the following table are for diodes in a CRC-228 array at 8°K (i.e., below freeze-out).

University of Rochester Zero-Bias InSb Detector Capacitance Estimates

Zero-Bias Diode Capacitance	0.42±0.03pF
Sense Node Capacitance	0.07pF
Gate Overlap Capacitance	0.06pF
TOTAL	0.55pF

This value (0.55pF) was used in calculating the performance values presented by UR in Table 3-1 and compares well with the value of 0.57pF measured by SBRC using the "noise-squared vs. signal" method on SCA002 at 8.1°K. Other measurements, including one direct measurement of the capacitance of 44 diodes in parallel on a fanout board, yielded values in the range 0.68pF to 0.75pF. Taking the known variables into consideration, UR estimates the uncertainty in their calculation of total zero bias detector capacitance to be about 0.1pF.

3.4 QE Falloff Across Array and With Temperature

All of the InSb arrays show variations in QE across the array and QE falloff with decreasing temperature. Sometimes, these variations are quite extreme, such as the 2–40% variation seen in SCA001 at 8°K. This array showed far less variation at 31°K (25–68%). The worst variations were seen by UR in FPA17, the standard-doped array, 0.4–33% at 31°K and 0.25–2% at 8°K (Figure 3-2); the least variations in SCA002, 28–40% at 10°K (Figure 3-10). Arrays RH2 and RH4 showed variations in QE of 29.3% and 12.6%, respectively in measurements by SBRC[2]. None of these variations are fully explained. SBRC[2] has postulated that

the variations across SCA001 and SCA002 at a given temperature are due to detector thickness variations across the array, and blackbody source misalignment.

Consideration of these QE variations at UR have led to the conclusion that the measured detector thickness variations across SCA001 can only partially account for the observed QE variations and, based on a measurement technique that precludes misalignment of the blackbody, misalignment can explain none of it. UR concludes that the observed QE variations must be due to contamination of the InSb[3]. Further work on this question will be done in the follow-on IRAC Definition Phase Contract.

3.5 Effect of Clocking Changes on Array Performance

Nine different clocking schemes were tried at UR to search for the method that would yield the lowest read noise within IRAC power dissipation limits.[3] All of the nine were variations on the double-correlated sampling technique. Changes in pulse widths and variations in the use of the enable and reset signals were tried; all gave essentially the same read noise (250 e^- operating with the detectors shorted).

3.6 Spectral Response of InSb

The spectral response of an AR-coated low-doped InSb array of identical design to those discussed above was tested at 77°K. The test data are presented in Table 3-2 and plotted in Figure 3-17. Of importance to QE measurements at 2.35μm is that the response is down 19% at this wavelength compared to its peak at 3.5μm. Between 2 and 5μm, the shape of the response curve is largely determined by the AR-coating. Beyond 5μm, the detector cutoff dominates. The cutoff wavelength decreases slightly with temperature.

μm	Resp	μm	Resp	μm	Resp
2.0	0.73	3.4	1.00	4.8	0.88
2.1	0.74	3.5	1.00	4.9	0.87
2.2	0.76	3.6	0.98	5.0	0.87
2.3	0.81	3.7	0.98	5.1	0.85
2.4	0.86	3.8	0.96	5.2	0.85
2.5	0.88	3.9	0.96	5.3	0.81
2.6	0.92	4.0	0.96	5.4	0.78
2.7	0.92	4.1	0.96	5.5	0.76
2.8	0.95	4.2	0.95	5.6	0.43
2.9	0.94	4.3	0.93	5.7	0.12
3.0	0.96	4.4	0.92	5.8	0.03
3.1	0.94	4.5	0.91	5.9	0.00
3.2	0.96	4.6	0.90	6.0	0.00
3.3	0.96	4.7	0.89		

Table 3–2. Relative Spectral Response of an Anti-Reflection Coated InSb Array at 77°K

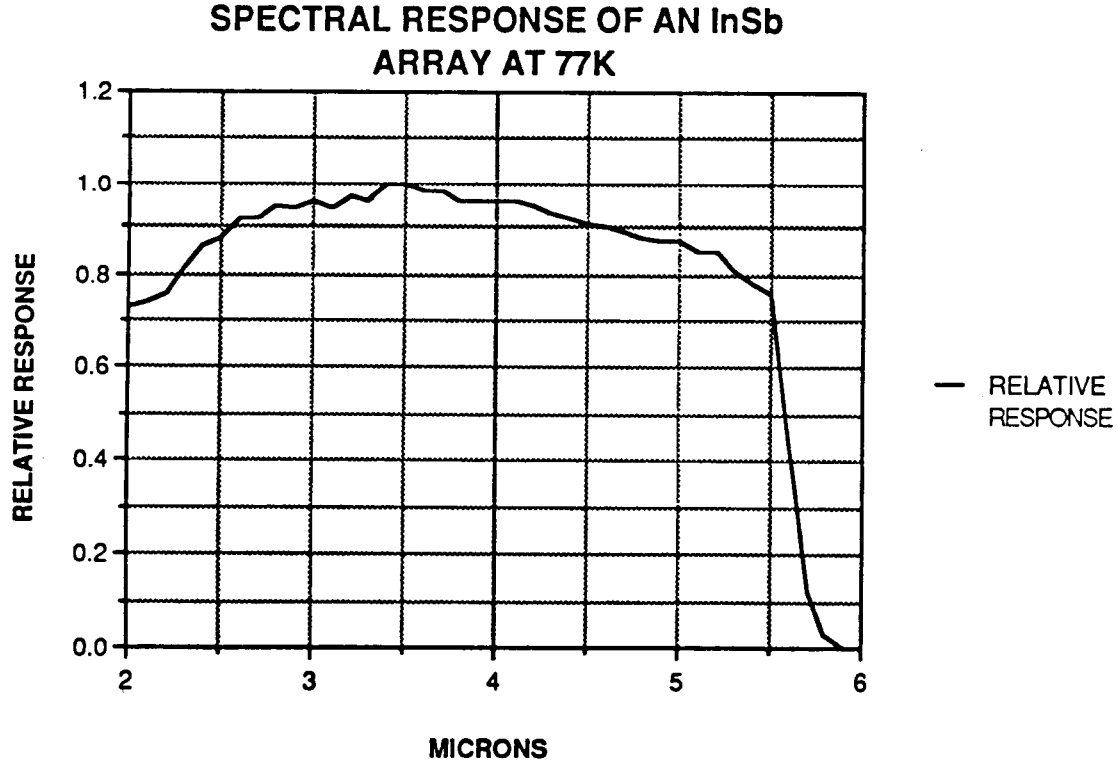

Figure 3–17. Relative Spectral Response of an Anti-Reflection Coated InSb Array at 77°K.

4.0 BAND II ARRAY DETECTOR RESEARCH

4.1 Overview of Test Results

Results with the Si:Ga array for Band II are sufficiently encouraging that, if necessary, an existing array could be flown and come very close to meeting present SIRTF performance requirements. Based on earlier GSFC tests[4] and recent tests on the Band III arrays at ARC,[5,6] the baseline conditions established for the tests performed were 43V bias and a temperature of 8°K. The Si:Ga array has a useful wavelength range of approximately $4-18\mu m$ with peak response at $15\mu m$. Test conditions have not yet been fully optimized for this array.

Under baseline conditions, responsivity is approximately 5.1 A/W and system-limited readout noise is about 190 μV (100 e^-) (Figure 4-1). Typical noise equivalent power (NEP) measurements are 2.0×10^{-17} W/root-Hz for a 0.205 s integration at the same temperature and bias. Signal-to-noise continues to improve up to the highest bias voltage available in the current test setup (43V). The temperature dependence at lower bias (10V) has been measured at 0.2 A/W at 5°K and 0.5 A/W at 11°K where the dark current becomes unacceptably high. Dark current as a function of temperature is displayed in Figure 4-2 where the slope corresponding to Sb impurity generation-recombination is included for comparison. Table 4-1 summarizes these results.

Dark current, though higher than that observed in the InSb and Si:Sb arrays, is still excellent at 30 aA at 8°K. The uniformity of this array is excellent: 8% (1 σ/mean) over a contiguous 58 × 59 region of the array. Sense node capacitance was measured to be 0.07pF, slightly higher than that of the Si:Sb arrays.

4.2 Transient Response

Initial studies of the transient response of the Si:Ga array (see Figure 4-3) have shown some of the irregular behavior often exhibited by bulk photoconductors under low background conditions. In response to a step input of IR, the array does not settle to its final value until 20–40 s after application of the step input, depending upon background level.

4.3 Power Dissipation

Power dissipation of the array is less than 1 mW under the stated operating conditions with VGGUC at 0.6V.

Array Designator: Type:	"Goddard Array" - Si:Ga		IRD ------ Req'mt
Tested by:	Goddard	Ames	(SAO)
Test Temperature (°K)	5.4	6 - 10	4 - 12
Dark Current (aA) @ 8 K	50	30	< 1.6
Read Noise (e-)	255	100	< 100
Detector Capacitance (pF)	0.1*	0.07	---
Quantum Efficiency (%)	---	---	---
Operability (%)	---	>99.5	99.5
Responsivity (A/W)	4.7	5.1	2.2
Responsivity Uniformity (%)	---	8	5
NEP (Watts/Root-Hz) @ T_i=0.2 s	---	2.0E-17	---
Well Size (e-)	---	>5.0E+05	>5.0E+05
AR Coated	No	No	---

All values means unless otherwise indicated

*Assumed

Table 4–1. Band II Array Test Data and Design Goals

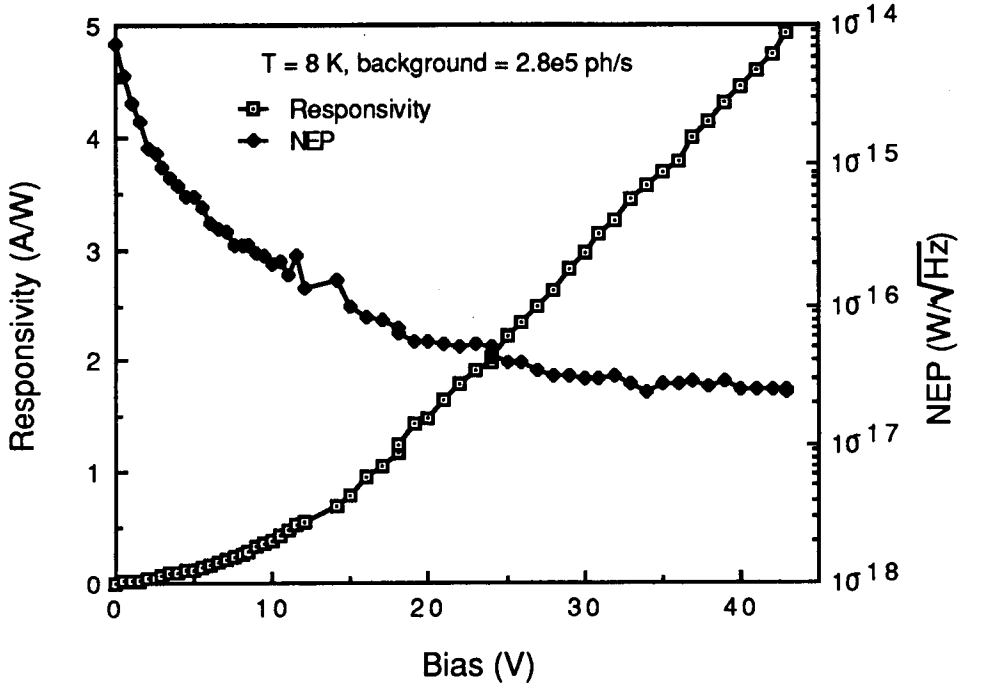

Figure 4–1. Si:Ga Responsivity, Noise Equivalent Power vs. Bias Voltage

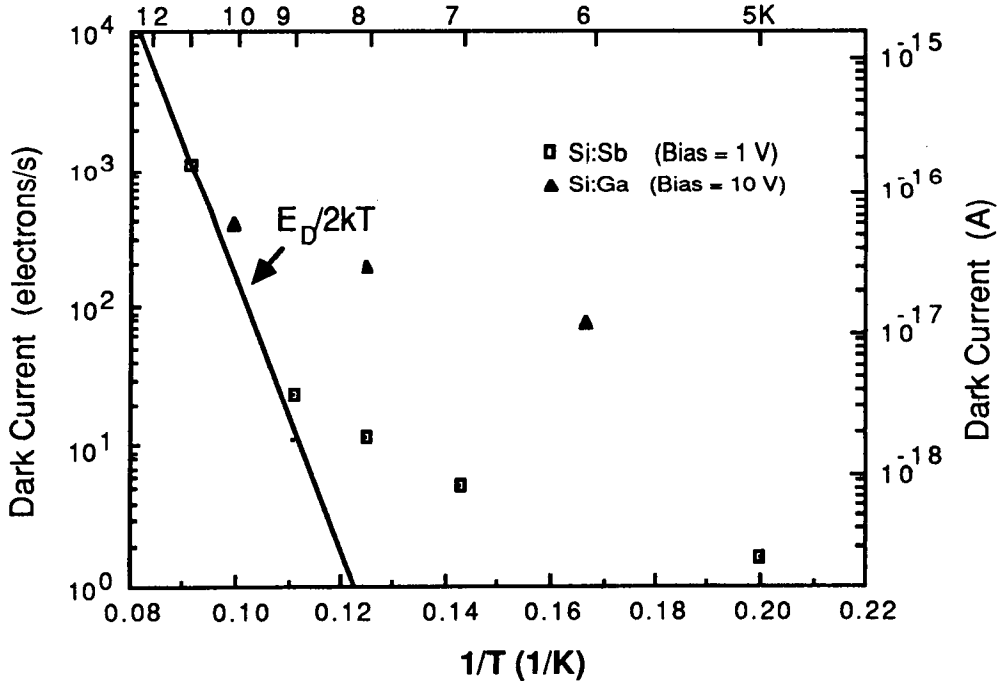

Figure 4–2. Si:Sb and Si:Ga Dark Current vs. Temperature.

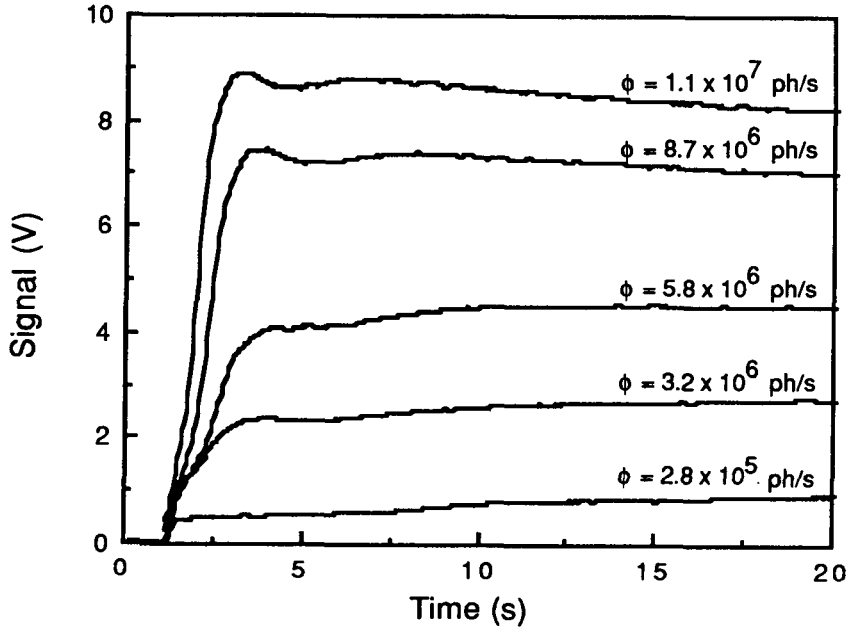

Figure 4–3. Response of One Si:Ga Array Pixel to Step Change in Incident Flux.

5.0 BAND III ARRAY DETECTOR RESEARCH

5.1 Overview of Test Results

As with the Band II Si:Ga array, the Si:Sb arrays evaluated for Band III showed excellent performance, performance which virtually meets SIRTF requirements. The Si:Sb arrays are useful over the wavelength range from about 15 to 31μm with peak response at 27μm.

Optimum operating conditions, in terms of signal-to-noise ratio, were found to be at a temperature of 8°K and an applied bias of 2V[5,6]. Under these conditions, peak-wavelength responsivity is 3.8 A/W, average dark current is 2.1 aA (13 e^-/s), and the (system-limited) readout noise is about 220 μV rms (100 e^-) for a 0.205 s integration. Table 5-1 summarizes these results; Figure 5-1 shows responsivity and NEP as a function of temperature. Noise was studied as a function of integration time (Figure 5-2) and shows only a factor of 2 increase at 200 s over the noise at 0.2 s. A typical NEP for this integration time is 2.7×10^{-17} W/root−Hz.

Dark current levels in these devices can be very small (about 0.3 aA at 5°K), and integrations of 30 minutes and longer have been achieved with the array blanked off without approaching well capacity. As temperature increases above 8°K dark current increases rapidly, reaching 175 aA by 11°K.

5.2 Measurement of Detector Capacitance

Measurement of the input capacitance of the sense node was made by monitoring the current on the reset line (VRSTUC) as a function of signal and resulted in a value of 0.061pF. Corroborating measurement of the capacitance through the current vs. signal voltage characteristic in the detector substrate line (DETSUB) and through a noise-squared vs. signal plot were also made and reasonable agreement obtained (Figure 5-3). The resulting value is less than the 0.1pF value predicted by Hughes, although this was based on their experience at higher temperatures.

Capacitance measurements were also made on the Si:Ga array (Figure 5-4) which yielded a value of 0.069pF.

Array Designator:	**SBRC 1**	**-- IRD --**
Type:	**Si:Sb**	**Req'mt**
Tested by:	Ames	(SAO)
Test Temperature (°K)	5 - 12	4 - 12
Dark Current (aA)	2.07	< 1.6
Read Noise (e-)	100	< 100
Detector Capacitance (pF)	0.06	- - -
Quantum Efficiency (%)	- - -	- - -
Operability (%)	>99.5	99.5
Responsivity (A/W)	3.8	3.4
Responsivity Uniformity (%)	- - -	5
NEP (Watts/Root-Hz) @ T_i= 0.2 s	2.70E-17	- - -
Well Size (e-)	2.0E+05	>5.0E+05
AR Coated	No	- - -

All values means unless otherwise indicated

Table 5–1. Band III Array Test Data and Design Goals

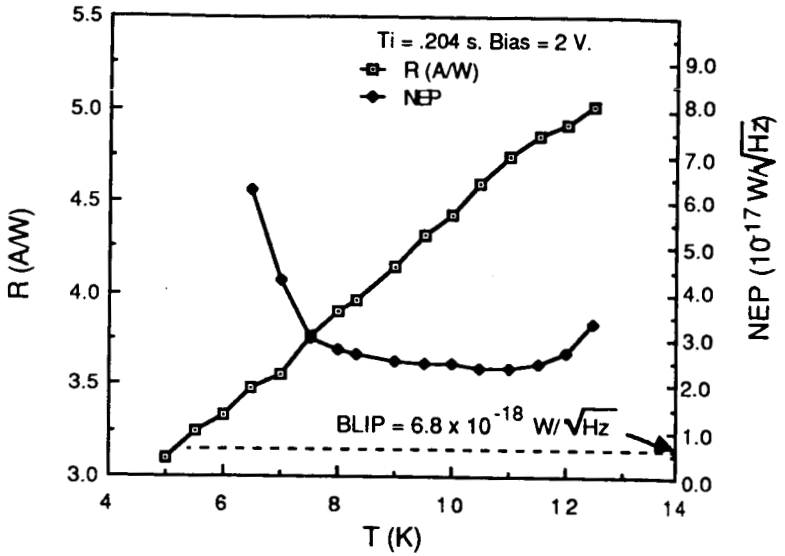

Figure 5-1. Si:Sb 58 × 62 Responsivity, Noise Equivalent Power vs. Temperature

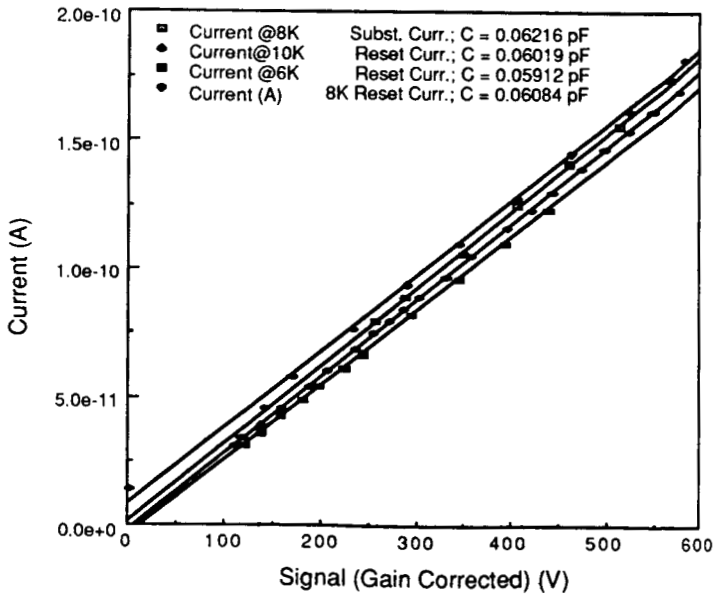

Figure 5-3. Si:Sb Capacitance Determination

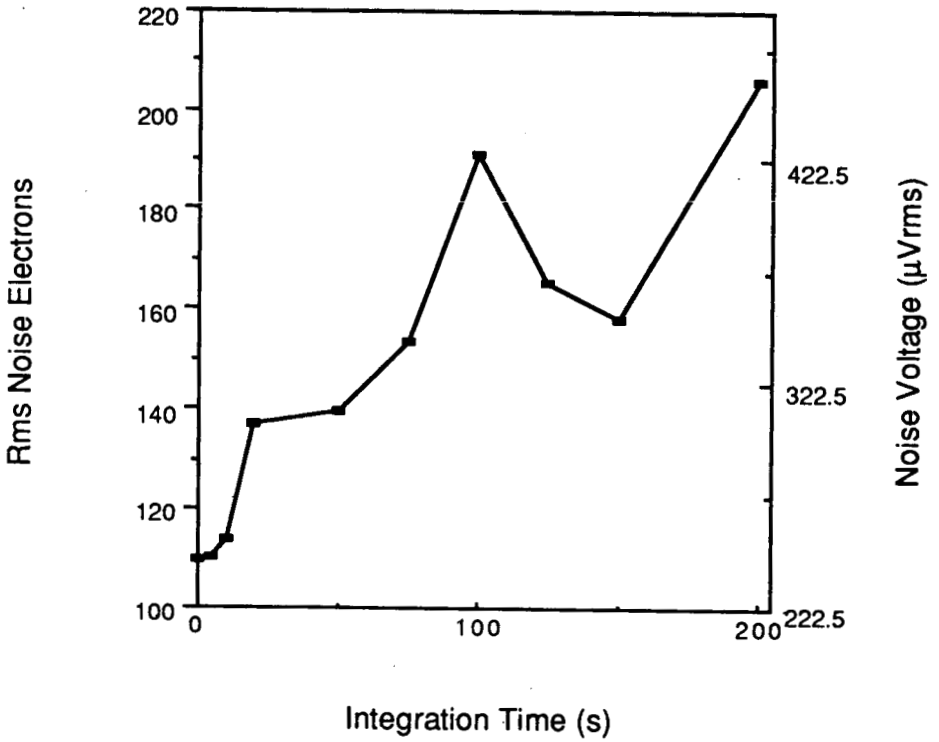

Figure 5-2. Si:Sb Noise vs. Integration Time

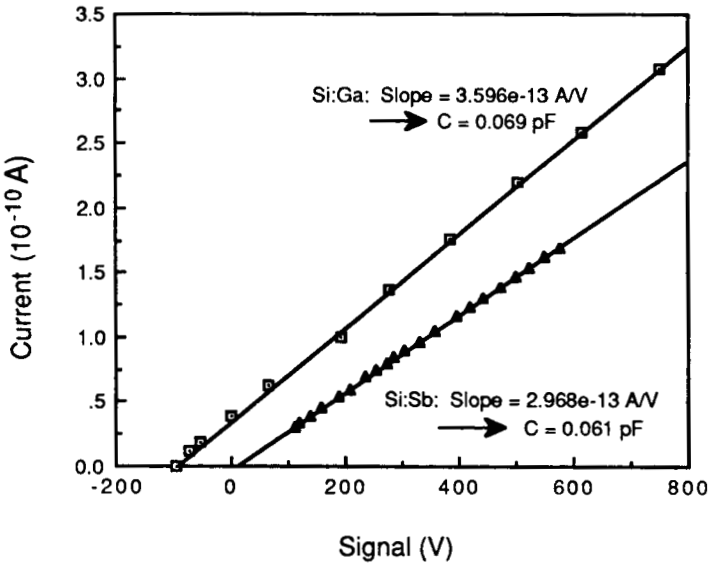

Figure 5-4. Si:Ga Measurement of Sense Node Capacitance

5.3 Linearity and Well Capacity

Measurement of the well capacity of Si:Sb and Si:Ga arrays was made by plotting the variation in the output signal as integration time was increased (Figure 5-5). Assuming a responsive QE of 0.25 and a photoconductive gain of 0.5, the first significant departure from linearity is seen at an integrated flux of about 1.4×10^6 photons which corresponds to a well size of 2×10^5 e^-. Figure 5-5 also shows the results of measurements made on the Si:Ga array which showed a larger well capacity of $>5 \times 10^5$ e^-. Note that the array could be operated with up to twice the integrated flux before hard saturation is reached.

5.4 Effect of Guard Ring Potential on Uniformity

Bright edge effects are displayed by these arrays under certain conditions. The guard ring potential (VGRNG or VGATE) was found to be effective in controlling these effects. By setting the guard ring potential to its optimum value, the excellent uniformity figures achieved (8% in Band II and 15% in Band III) are realized (Figures 5-6 and 5-7).

5.5 Power Dissipation

Array power dissipation is primarily determined by the voltage applied to the output FET's (VDD) and the unit cell FET's (VGGUC) (Figure 5-8). By operating the arrays at low VGGUC, at 0.6V, power dissipation in both the Si:Ga and Si:Sb arrays can be held below 1 mW without degrading performance over that obtained at higher values of VGGUC.

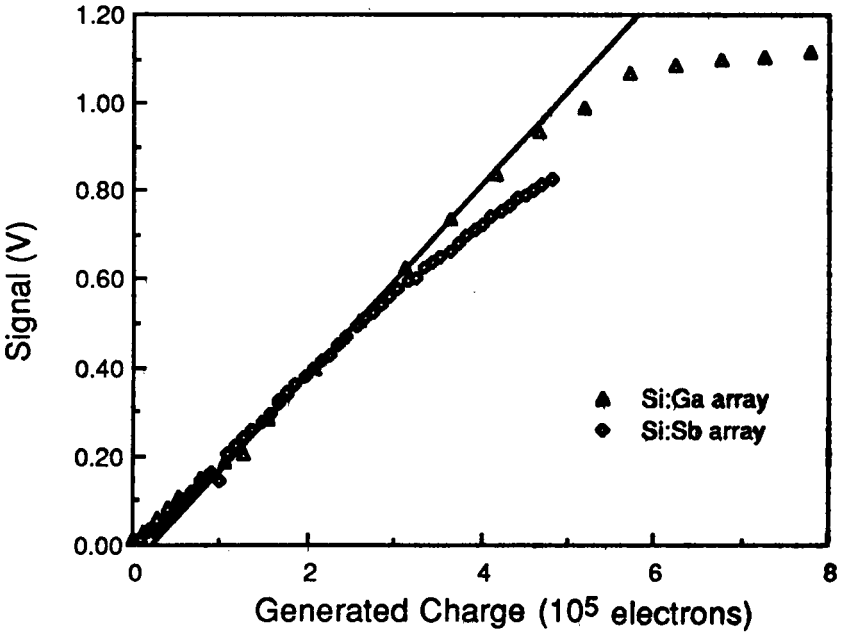

Figure 5–5. Linearity, Well Capacity of Si:Sb and Si:Ga Arrays

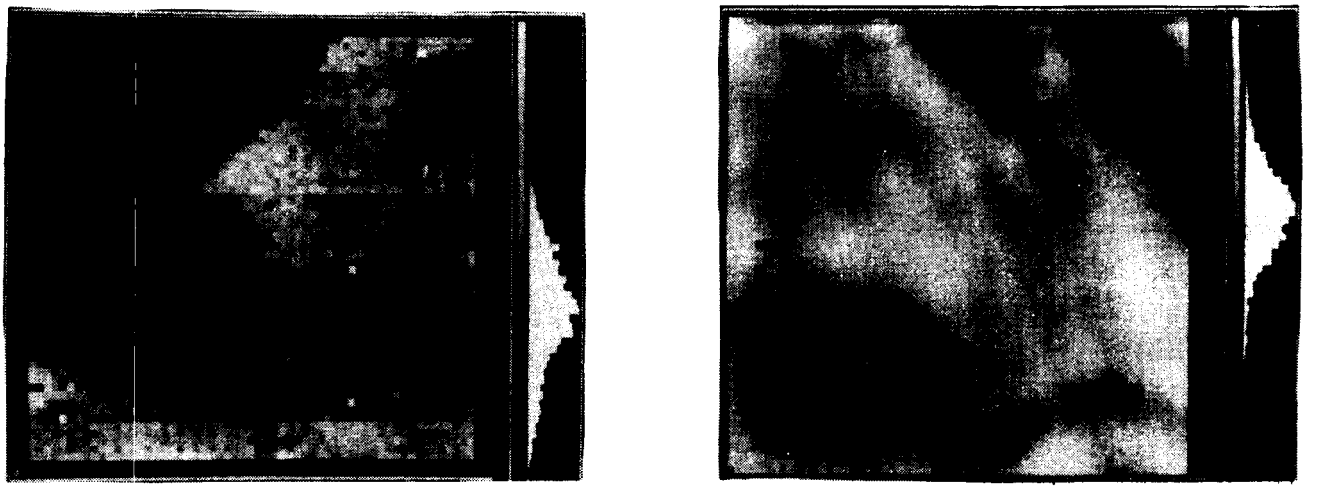

SBRC Si:Sb array

Si:Ga array

Figure 5–6. Unprocessed Array Output for Si:Sb Array (left) and Si:Ga Array (right)

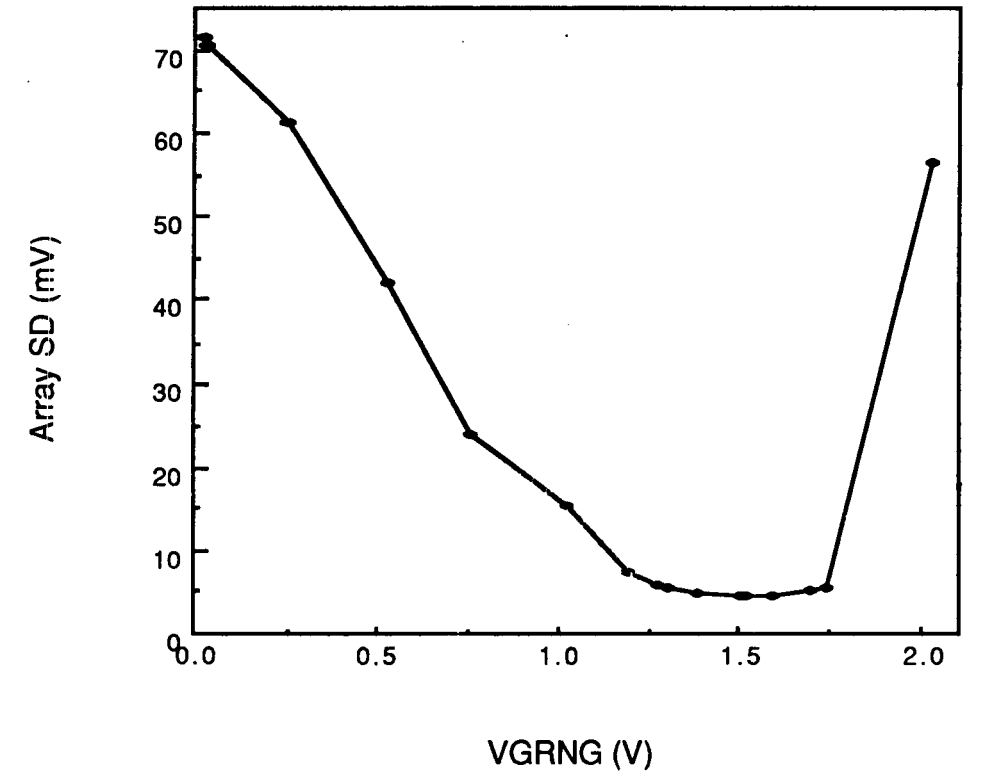

Figure 5-7. Array Uniformity vs. VGRNG

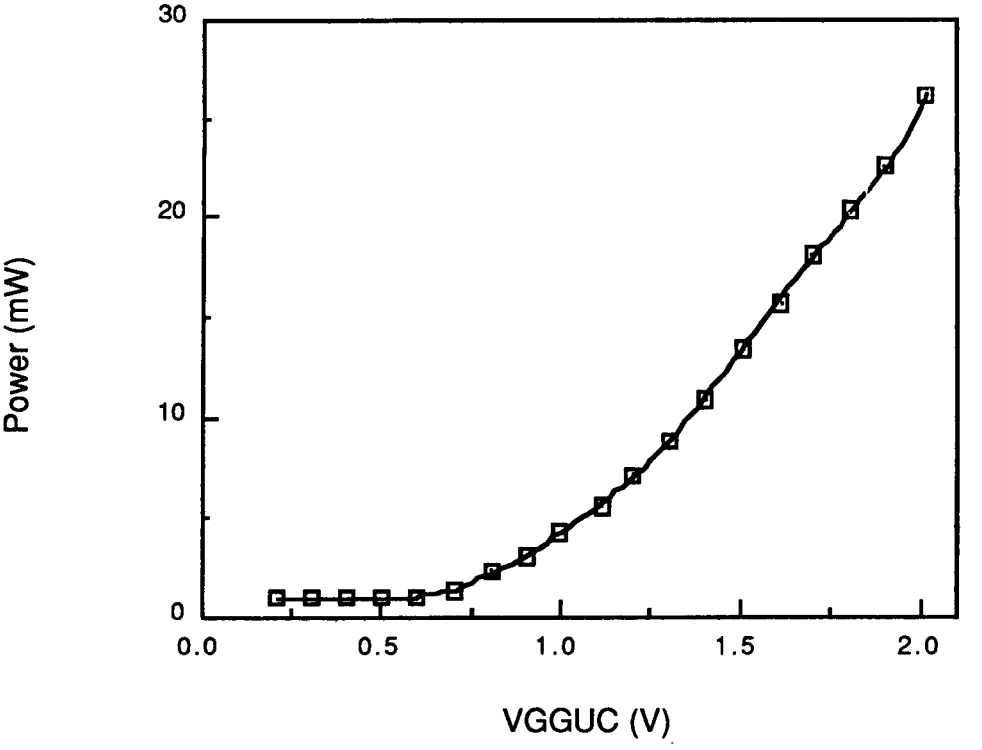

Figure 5-8. Si:Sb Array Power Dissipation vs. VGGUC

6.0 BEAMSPLITTER RESEARCH

6.1 Introduction

The Infrared Array Camera utilizes two dichroic beamsplitters for the separation of the incident infrared energy into three wavelength ranges. The performance of these elements is a key determinant of the overall performance of the camera.

A pair of beamsplitters for the 28–30μm range was designed and fabricated by the Optical Coating Laboratory, Inc. (OCLI) to the IRAC specifications shown in Table 6-1.

The purpose of this effort[7] was to design appropriate coatings for beamsplitters 1 and 2, followed by trial deposition of the coatings on cadmium telluride (CdTe) substrate material. Measurements of the transmission in the wavelength bands of interest would then allow a realistic performance level to be set for these elements.

Beamsplitter	Wavelength Range	Design Goal
1	1–5.0μm	R $\geq$ 90% average
	5.2–30.0μm	T $\geq$ 55% average
2	5.0–18μm	R $\geq$ 90% average
	18.5–30.0μm	T $\geq$ 55% average

Table 6–1. IRAC Beamsplitter Specifications for 1.0–30.0μm

6.2 Theoretical Performance

The calculated performance of the coating design for beamsplitters 1 and 2 are shown in Figures 6-1 and 6-2. In both cases, the performance levels exceed the design goal specifications; however, the model does not include losses due to absorption in the thin film structure. Past experience dictates that the realized performance will be lower than projected, especially in the transmission regions due to unmodelled interactions between the layers, random errors in the coating deposi-

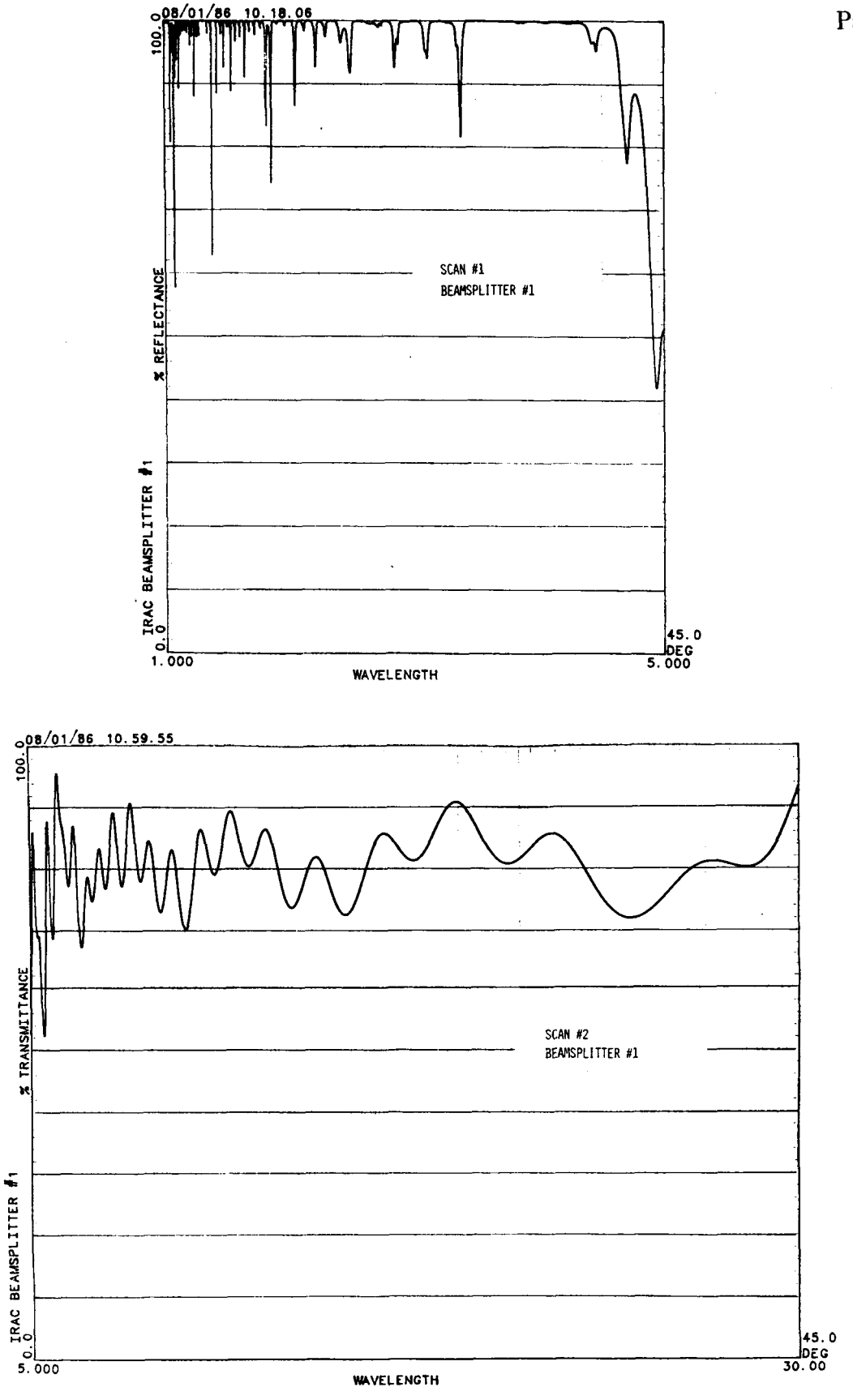

Figure 6–1. Calculated Performance for Beamsplitter 1

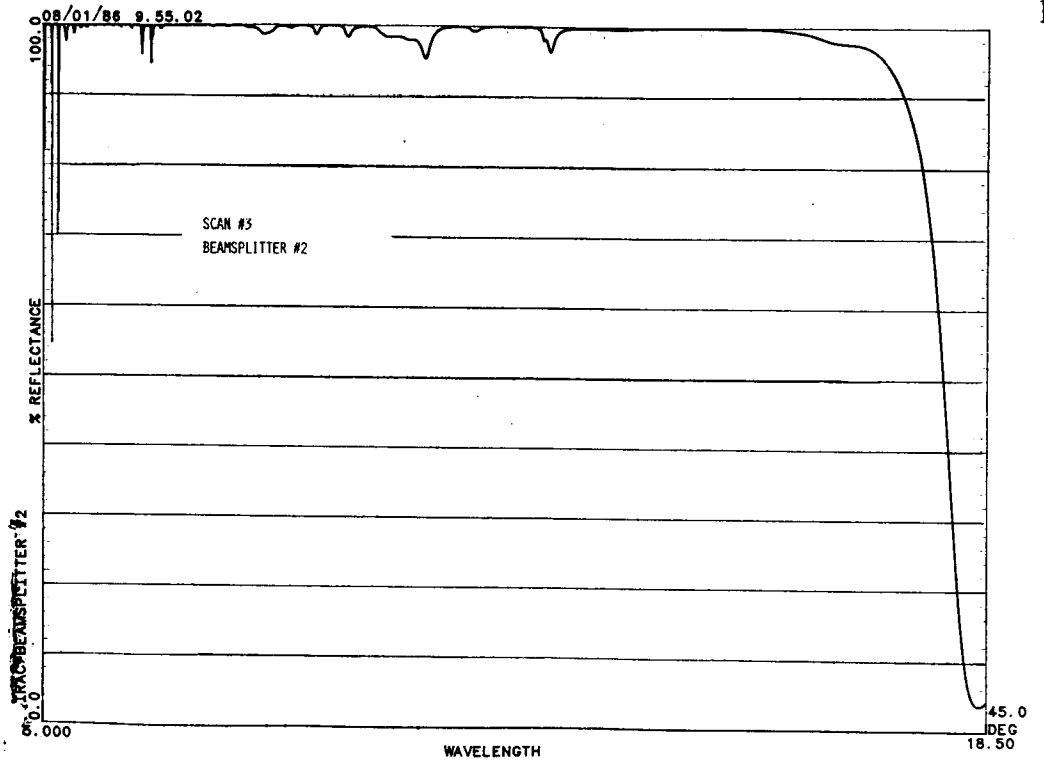

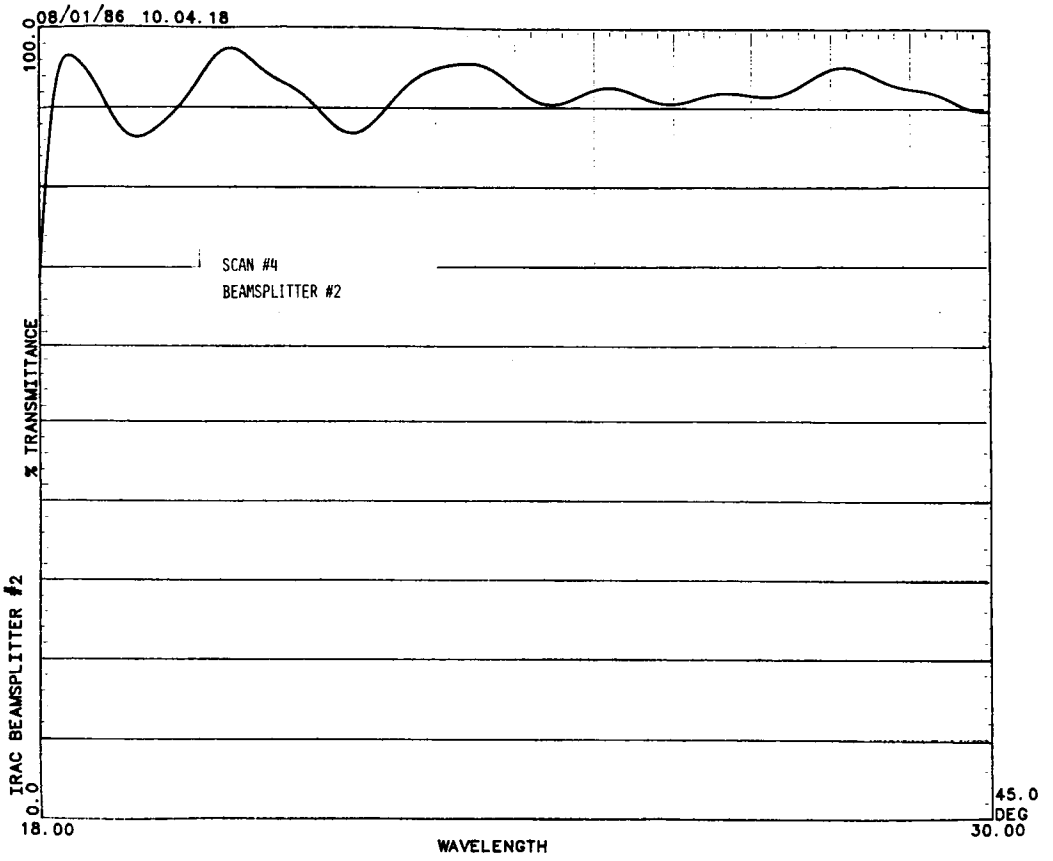

Figure 6–2. Calculated Performance for Beamsplitter 2

tion, and the fact that accurate absorption coefficients for thin film materials at the operation temperature are not known.

The broad wavelength ranges (from 1.0μm to 5.0μm for beamsplitter 1 and from 5.2μm to 18.0μm for beamsplitter 2) over which reflectance is required result in reasonably complex designs.

6.3 Experimental Results

Both beamsplitter designs were calibrated in the OCLI coating chamber and then deposited on CdTe substrate. Following the deposition an analysis was made of the spectral and environmental performance that resulted. Since OCLI does not have the capability to measure reflectance at cold temperatures, the performance cold has been inferred from the ambient temperature data. Future tests at the University of Arizona will verify these cryogenic temperature figures. At cold temperature the absorption of the thin films is reduced, and therefore the reflectance at this temperature is expected to be equal to or greater than the performance at ambient temperature. This section includes test data taken by both OCLI and the University of Arizona.[8] OCLI test data plots may be found in their Final Report on this work.[7]

6.3.1 Beamsplitter 1

The spectral characteristics of beamsplitter 1 were measured at both ambient temperature and 15K in accordance with the parameters listed in the table below and appended to the OCLI Final Report.[7]

Scan	Range	Type	Angle	Instrument	Temperature
1	1.0–2.5μm	R	45°	DK-2	Ambient
2	2.5–30μm	R	45°	PE-983	Ambient
3	2.5–30μm	T	0°	PE-983	Ambient
4	2.5–30μm	T	0°	PE-983	15 Kelvin
5	2.5–30μm	T	45°	PE-983	Ambient

From this spectral information, the actual performance of the dichroic at 45° is estimated by OCLI to be:

Wavelength Range	Design Goal	Measured Performance
1–5.0μm	R $\geq$ 90% Average	84.3% (Ambient)
5.2–30μm	T $\geq$ 55% Average	65.6% (Ambient)
		76.7% (Calculated at 15K*)

The previously identified technical concern regarding transmission from 5.2 to 30.0μm is alleviated by this dichroic design. However, further effort needs to be made in the 1.0 to 5.0μm reflectance region. Examination of the spectral test data[7] indicates the loss in reflectance is due to absorption dips between the reflectance multilayer stack centers. This has been verified by measurement. The transmission level in this region is virtually zero. Absorption coefficients for the thin film materials were estimated and included in the computer design. This performance is plotted in Figure 6-3 and indicates behavior similar to the actual performance.

For manufacture of acceptable flight dichroics, a more complex coating design may be required. By adding thin film structures to the design these absorption dips may be minimized. However, the increase in coating thickness material will lower the in-band transmission. An alternate approach to consider is moving some of the reflectance stacks to the rear surface of the beamsplitter in order to decouple the interference effects which emphasize these dips. Unfortunately this would complicate the optical design of the camera.

As part of this study, the coating was also tested for environmental performance at OCLI with the following results:

Test		Result
24-Hr. Humidity	per MIL-C-675A	Pass
Slow Tape	per MIL-M-13508B	Pass
50 Rub Cheesecloth	per MIL-M-13508B	Pass

Subsequently, beamsplitter 1 was retested at the University of Arizona.

Figures 6-4 and 6-5 give the OCLI beamsplitter 1 transmission from 5 to 35μm at 0° and 45° incident angle respectively as measured by UA. Figure 6-6 shows the 0° measurements with the OCLI test measurement data superimposed

*Cold temperature transmission at 45° is calculated as follows:

$$\frac{45^\circ \text{ T at } 15K}{45^\circ \text{ T at Amb}} = \frac{0^\circ \text{ T at } 15K}{0^\circ \text{ T at Amb}}$$

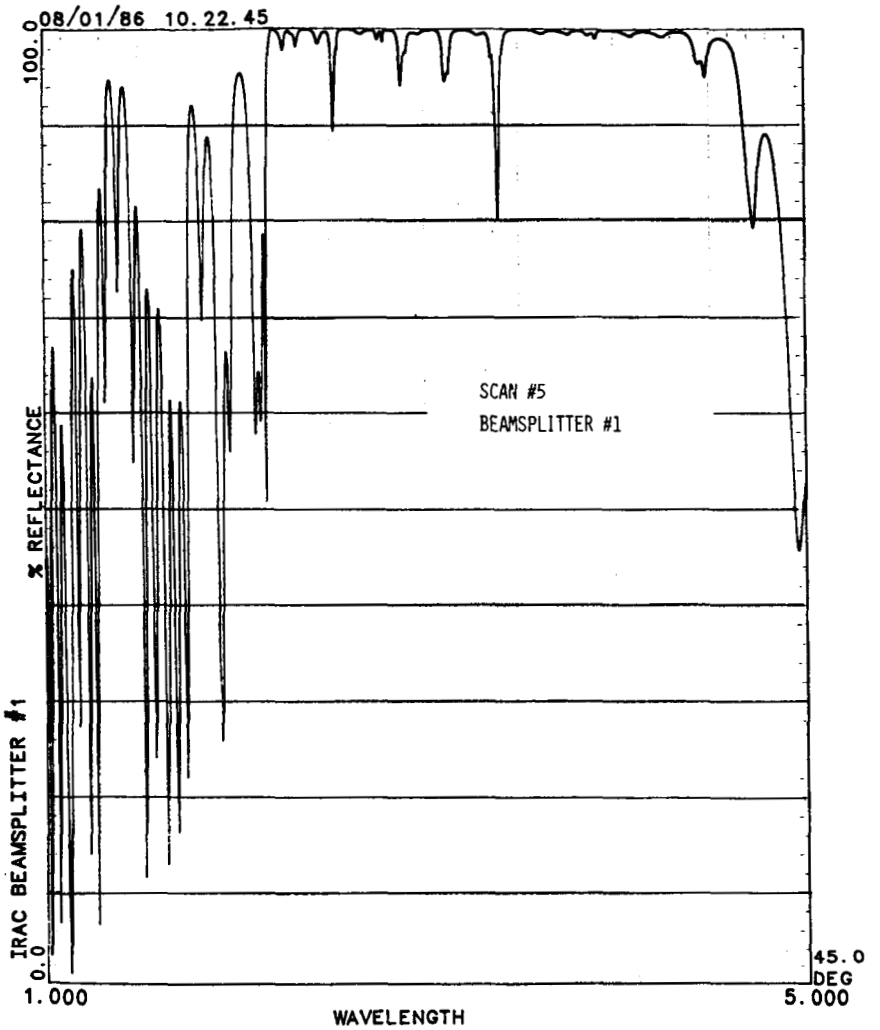

Figure 6–3. Beamsplitter 1 Calculated Performance with Thin Film Absorption Losses Included

as a dashed line. There is excellent agreement between the curves.

Figure 6-7 shows beamsplitter 1 transmission with IRAC Band II broadband filters superimposed as hatched columns. The height of the columns represents the percent transmission of the individual filters.

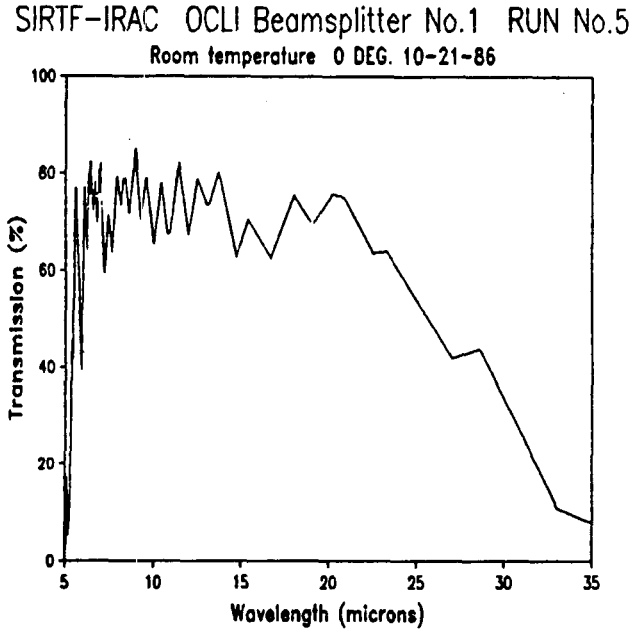

Figure 6-4. Beamsplitter 1 Room Temperature Transmission, 0° Angle of Incidence

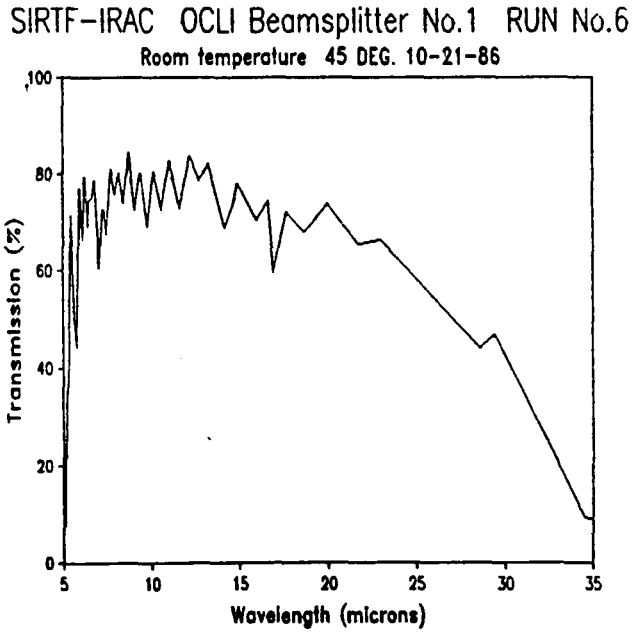

Figure 6-5. Beamsplitter 1 Room Temperature Transmission, 45° Angle of Incidence

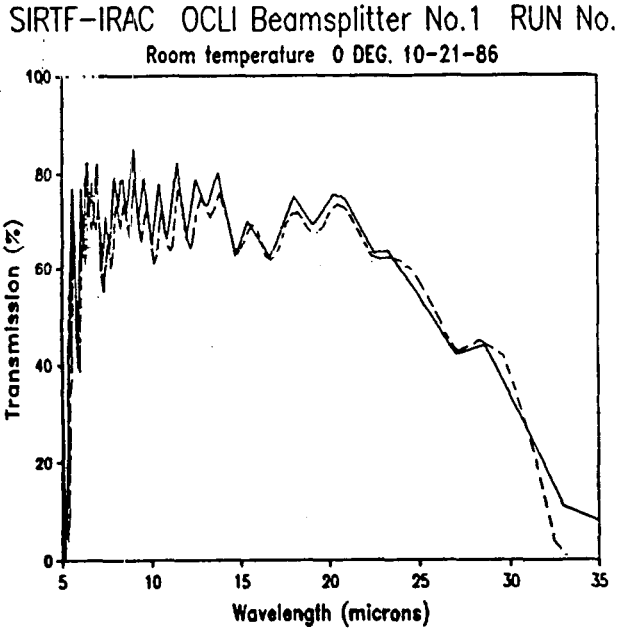

Figure 6-6. Beamsplitter 1 Room Temperature Transmission, 0° Angle of Incidence. UA (solid) and OCLI (dashed) Test Data Superimposed.

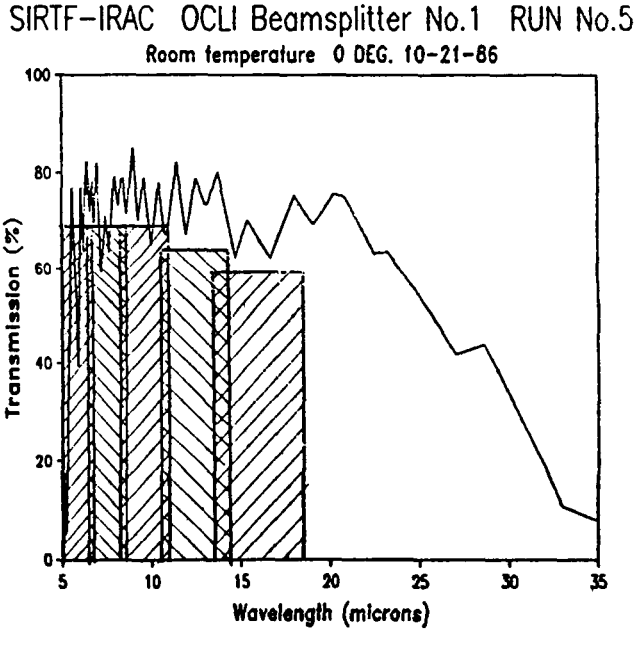

Figure 6-7. Beamsplitter 1 Room Temperature Transmission, 0° Angle of Incidence. IRAC Broadband Band II Filters Superimposed.

6.3.2 Beamsplitter 2

The spectral performance of beamsplitter 2 was measured in a manner analogous to beamsplitter 1, and is summarized in the table below and in the OCLI Final Report.[7]

Scan	Range	Type	Angle	Instrument	Temperature
1	2.5–30.0μm	R	45°	PE-983	Ambient
2	2.5–30.0μm	T	0°	PE-983	15 Kelvin
3	2.5–30.0μm	T	0°	PE-983	Ambient
4	2.5–30μm	T	45°	PE-983	Ambient

From this information, the actual performance of the dichroic at 45° can be estimated as follows:

Wavelength Range	Design Goal	Measured Performance
5.0–18.0μm	R ≥ 90% Average	88.4% (Ambient)
18.5–30.0μm	T ≥ 55% Average	58.8% (Ambient)
		62.7% (Calculated at 15K*)

As in the case of beamsplitter 1, the lower than desired reflectance from 5.0 to 18.0μm is due to absorption losses in the thin film structure. This effect has been modelled in Figure 6-8. The effect of adding additional coating material to the design to correct the observed deficiencies is riskier than for beamsplitter 1 since the physical thickness of the layers is greater at these long wavelengths. Thus the effect of such changes on transmission needs to be considered thoroughly and there is the additional risk that the stress buildup in this thicker coating could lead to adhesion failures.

Beamsplitter 2 was evaluated for environmental durability with the following results:

*Cold temperature transmission at 45° is calculated as follows:

$$\frac{45^\circ \text{ T at } 15K}{45^\circ \text{ T at Amb}} = \frac{0^\circ \text{ T at } 15K}{0^\circ \text{ T at Amb}}$$

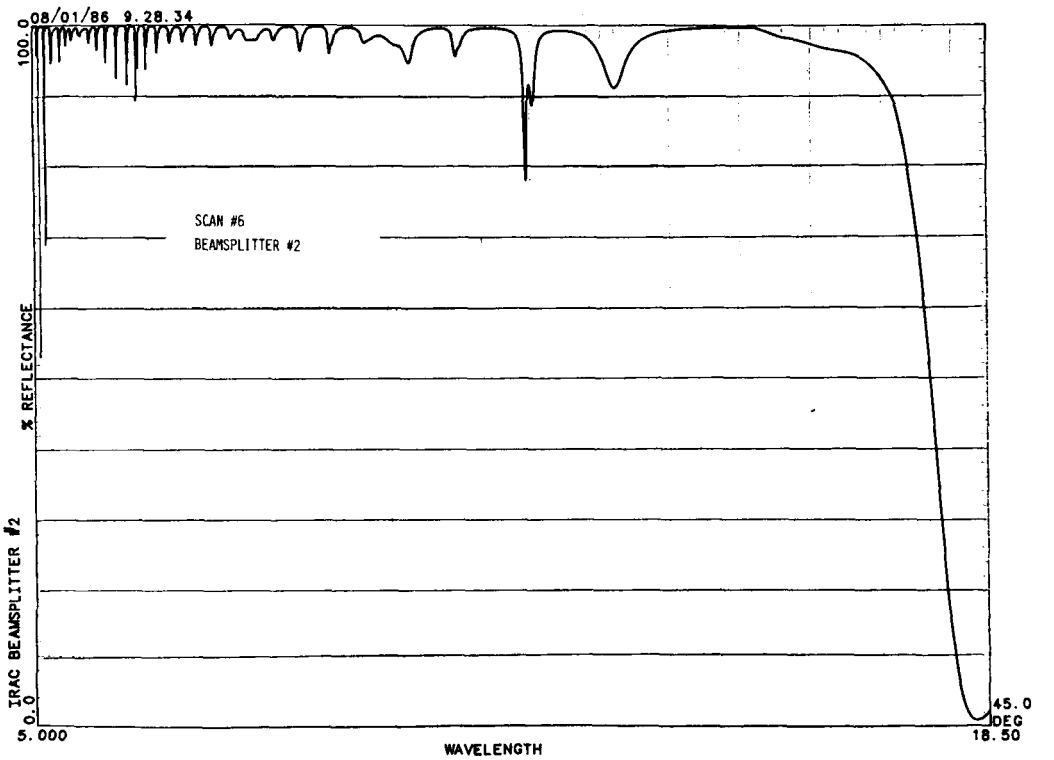

Figure 6–8. Beamsplitter 2 Calculated Performance with Thin Film Absorption Losses Included

Test		Result
24-Hr. Humidity	per MIL-C-675A	Pass
Slow Tape	per MIL-M-13508B	Pass
50 Rub Cheesecloth	per MIL-M-13508B	Pass

Corroboration of these results at the University of Arizona produced the data displayed in Figures 6-9, 6-10, and 6-11.

Figures 6-9 and 6-10 give the transmission of OCLI beamsplitter 2 transmission from 10 to 35μm at 0° and 45° incident angle respectively. Figure 6-11 shows the 0° measurements with the OCLI measurement superimposed with a dashed line. There is also very good agreement with the exception of a slight wavelength shift. Before making additional measurements, UA will recalibrate the spectrophotometer wavelength scale against a reference absorption cell.

Figure 6-12 shows the product of the transmission of beamsplitters 1 and 2 with two Band III broadband filters superimposed as hatched columns. It is clear that the transmission through both beamsplitters between 25 and 30μm is undesirably low.

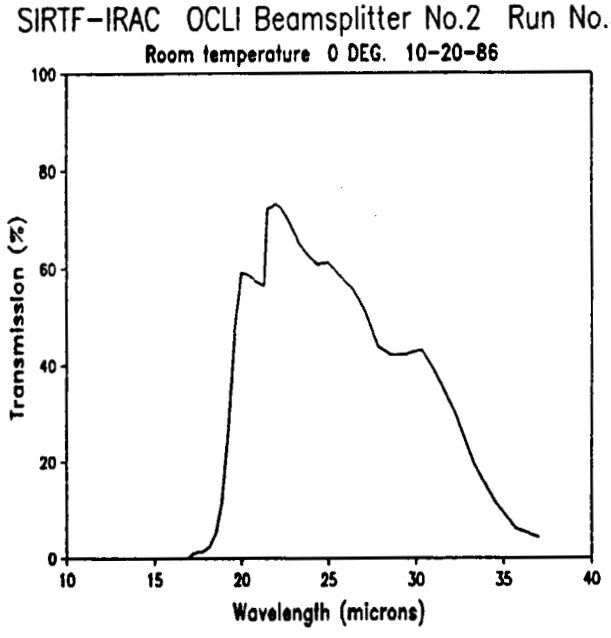

Figure 6-9. OCLI Beamsplitter 2 Run No. 3: 0° Angle of Incidence

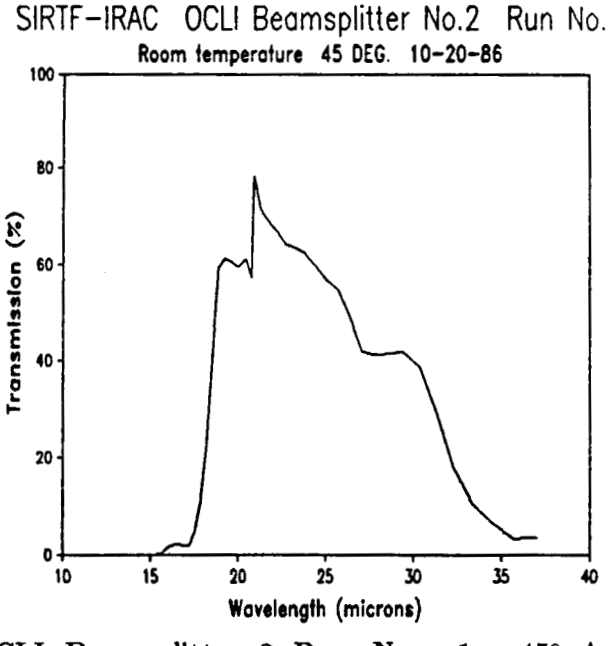

Figure 6-10. OCLI Beamsplitter 2 Run No. 1: 45° Angle of Incidence

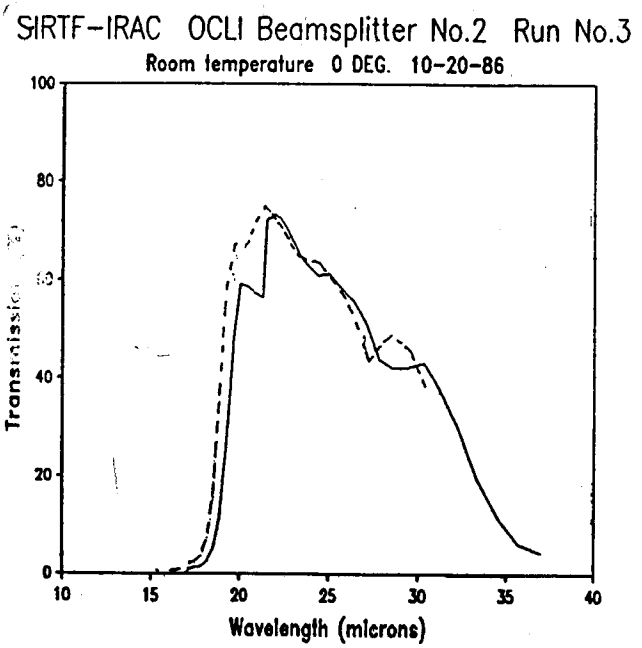

Figure 6-11. OCLI Beamsplitter 2 Run No. 3: 0° Angle of Incidence

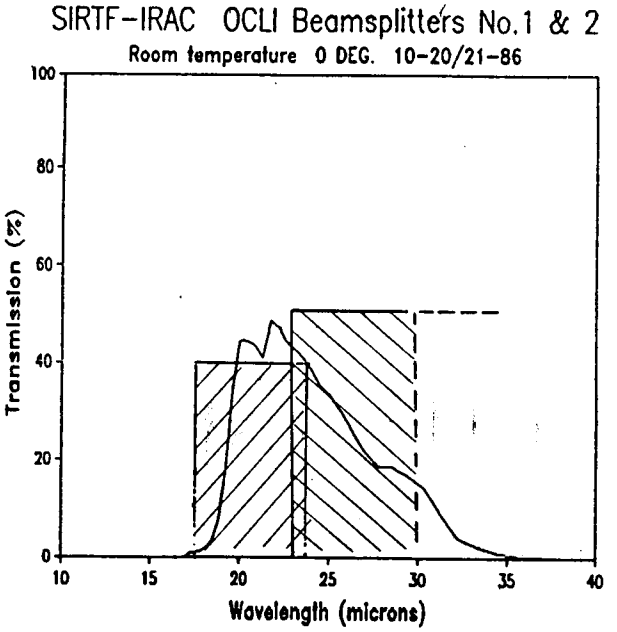

Figure 6-12. OCLI Beamsplitter 2 Run Nos. 1 & 2; 0° Angle of Incidence

6.4 Observing Efficiency with Beamsplitters

The purpose of the beamsplitters is to permit simultaneous observation of the same focal plane in the three IRAC bands. There are four advantages to simultaneous versus sequential imaging in the three bands: 1) certain positional registration in the three bands; 2) fewer instrument moving mechanisms; 3) reduced instrument mode changes and spacecraft maneuvering; and 4) more efficient use of observing time. In this section the question of whether or not, given the transmissions and reflection losses of the beamsplitter, the beamsplitter approach does indeed make more efficient use of observing time.

Given:

$\epsilon_1, \epsilon_2, \epsilon_3$	are efficiencies of each band with the beamsplitters.
T_1, T_2, T_3	are the required integration times with sequential (no beamsplitters) observations.
τ_1, τ_2, τ_3	are the required times for switching beams and stabilizing (no beamsplitters).
n_1, n_2, n_3	are 1 for detector readout or sky background noise 2 for dark current noise

For T_i, the integration time to reach a required signal-to-noise ratio without the beamsplitters, and T, the time to reach a required signal-to-noise ratio with the beamsplitters, we find:

Detector readout noise limited: $T = T_i/\epsilon_i$

Background noise limited: $T = T_i/\epsilon_i$

Dark current noise limited: $T = T_i/\epsilon_i^2$

In general: $T = \dfrac{T_i}{\epsilon_i n_i}$

Then the ratio of observing time with the beamsplitters to the time for sequential observations is:

$$\frac{T(\text{Beamsplitters})}{T(\text{Sequential})} = \frac{\text{maximum of } \left(\dfrac{T_1}{\epsilon_1 n_1}, \dfrac{T_2}{\epsilon_2 n_2}, \dfrac{T_3}{\epsilon_3 n_3} \right)}{T_1 + T_2 + T_3 + \tau_1 + \tau_2 + \tau_3}$$

Table 6-2 gives the beamsplitter efficiencies as measured by UA and OCLI in various filter bands.

Band	Filter	λ	No. 1	No, 2	Product
1	3	1-3	.84 (R)		
	8	3-4	.84 (R)		
	11	4-5.3	.84 (R)		
2	12	5.1-6.9	.69 (T)	.84 (R)	.58
	15	6.5-8.8	.81 (T)	.84 (R)	.68
	16	8.5-11.2	.82 (T)	.84 (R)	.69
	18	10.7-14.5	.83 (T)	.84 (R)	.70
	22	13.8-18.6	.77 (T)	.84 (R)	.65
3	23	17.6-23.8	.65 (T)	.60 (T)	.39
	26	22.8-30	.55 (T)	.50 (T)	.28

Table 6-2. Beamsplitter Efficiency for Given Filter Band Pass

The following are three examples comparing the beamsplitter to sequential times. In each example, the switching and recovery times (τ_1, τ_2, τ_3) are taken to be zero so the resulting ratio is an upper limit. The beamsplitter approach takes less observing time when the ratio is less than 1.

In the first example, equal sequential time in all broadband filters is required, i.e., $T_1 = T_2 = T_3 = T_o$

Configuration	1	2	3	4	5
Band			Filters		
1	3	3	8	11	11
2	15	16	18	12	22
3	23	23	23	26	26

Then,

$$\frac{T_{split}}{T_{seq.}} = \frac{T_o\ (1/.68 + 1/.69 + 1/.70 + 1/.58 + 1/.65)}{T_o\ (10)} = 7.6/10 = .76$$

In the second example sequential times equal to 4 T_o in Band I, filter 11,* T_o in Band II, filters 15, 16, and 18, and T_o in Band III, filters 23 and 26, are used.

Then,

$$\frac{T_{split}}{T_{seq.}} = \frac{T_o(1/.39 + 1/.28)}{T_o\ (4 + 3 + 2)} = 6.1/9 = .68$$

In the third example equal sequential times T_1, = T_2 = T_3 = T_o are used in one filter and each band.

Then,

Band	1	Filter 11	4 - 5.3μ
	2	18	10.7 - 14.5
	3	26	22.8 - 30

$$\frac{T_{split}}{T_{seq.}} = \frac{\max\ (T_o/.84,\ T_o/.70,\ T_o/.28}{3\ T_o + (\tau_1 + \tau_2 + \tau_3)} \leq 1.19$$

6.5 Conclusions

Coating designs for the dichroic beamsplitters of the IRAC camera have been produced and experimental depositions have been performed. Test results at OCLI and UA indicate that the transmission requirement of beamsplitter 1 has been achieved, but that the reflectance at the shorter wavelengths must be improved. Beamsplitter 2 demonstrated acceptable reflectance at the shorter wavelengths but less than desirable transmission. Within the confines of this study, extensive attempts could not be made to tune the coating deposition for maximum reflected performance. A certain amount of improvement can be expected from that effort when it is undertaken later in the program. Transmission improvement beyond 23μm is highly desirable and short wavelength reflectivity must be improved but not at the expense of long wavelength transmission.

---

*References are to filters defined in IRAC-202, "IRAC Instrument Requirements Document."

Further work should concentrate on refinements in the design that will enhance the broadband reflectance. In addition, through dialogue with the system designer certain critical spectral ranges can be identified and the performance in those areas maximized over other less critical regions.

An analysis of the dichroic approach showed that it is more efficient than sequential measurements when data must be taken in three bands. Taking instrument settling times, ignored in this simple calculation, into consideration makes the advantage of the dichroic approach even greater.

7.0 OPTICAL ANALYSIS

7.1 Introduction

The GSFC Optical Design Section working in conjunction with Dr. William Hoffmann of the University of Arizona has performed conceptual baseline optical analyses for IRAC. This analysis modelled refractive, reflective, and catadioptric configurations and evaluated them for system performance by utilizing computer-aided ray tracing techniques (ACCOS V).[9]

7.2 IRAC Optical Specification Status

The pixel sizes originally chosen for IRAC were 50μm (128 $\times$ 128) for Band I and 100μm (64 $\times$ 64) for Bands II and III. Pixel size is being reconsidered in an ongoing tradeoff study being performed at SBRC. The current baseline pixel size is 75μm for all three bands.

Image quality for IRAC is specified in terms of Encircled Energy (EE). Each specification applies over the entire wavelength band and field of view of the instrument. For the wide field of view, 80% of the point spread function energy must fall either within a single pixel or within a circle defined by the Airy Disk diameter (D = 2.44 λ/f). For the narrow field of view, 80% of the same function must fall within a circle of diameter equal to or greater than two pixels so as to avoid undersampling. It also must fall within a circle defined by the Airy Disk diameter.

7.3 Refractive Work

At the onset of the IRAC optical analysis effort for FY1986, the refractive cesium iodide singlet design initially proposed was evaluated. The image quality suffered from astigmatism, chromatic aberration, and curvature of field. This was especially true in Band I. Optimization was performed such that the geometric wide-field spot sizes for Bands II and III met the spec for a 100μm pixel size at 300°K. The Band I singlet could not be optimized to meet the wide-field specification. No other material was found that performed better than cesium iodide for all three bands. Therefore a silicon/germanium air-spaced achromatic doublet was designed for Band I for a 50μm pixel size at 300°K. Geometric ray tracing has been performed on these designs for the wide- and narrow-field cases. This was done by tracing 300 rays through the system for each particular field angle. The geometric image quality for all three bands met specification for both the wide- and narrow-field modes.

To determine the idealized performance of these IRAC designs, a diffraction image quality analysis has been performed for both the wide- and narrow-field modes for all three bands for this system. A diffraction analysis determines if the performance of the system is limited by diffraction and determines the real spot sizes and MTF's of the system.

An investigation into broadband antireflection coatings for the Band I achromatic air-space doublet at room temperature was also performed. A triple-layer AR coating of MgF_2, CeO_2 and Si each was assumed on a substrate of germanium. The coating increased the transmittance from 46% to about 92% with maximum transmittance values of 95% at 2.35μm and 98% at 5.2μm. A similar AR coating can be produced on a substrate of silicon. An investigation at the 4°K operating temperature has not been performed yet.

The 4°K operating temperature of IRAC will cause the refractive index, element thickness, and element spacing to change from the baseline (room temperature) values. This in turn will cause the image to go out of focus as the instrument is cooled down. The depth of focus for Bands I, II and III are respectively $\pm 86\mu$m, $\pm 236\mu$m, and $\pm 170\mu$m. This was determined by defocusing the image plane until the worst case geometric 80% Encircled Energy Spot Diameter (EESD) exceeded the specification. Thermally induced focus shifts that exceed these values would have to be corrected by actively refocusing the lens or detector. Passive compensation for thermal focus shifts would require the knowledge of the cryogenic optical properties of the lens material. Unfortunately cryogenic data of optical properties of infrared materials at 4°K are rare.

7.4 Catadioptric Work

Catadioptric designs were considered only briefly due to the success of the all-reflective two aspheric mirror design concept. No viable catadioptric design had been identified.

7.5 Reflective Work

7.5.1 Review of Work Done

Reflective IRAC designs were looked at initially out of concern for chromatic aberration and cryogenic uncertainties of refractive indices and thermal expansion coefficients at 4°K. A number of two-mirror concepts were studied using Dr. Hoffmann's original spherical tilted collimator. All of these designs suffered from first order limitations. Most of these limitations were due to image inaccessibility and/or obscurations. Tilting and decentering the mirrors to avoid these first order

limitations resulted in poor image quality. No feasible all-reflective approach emerged for the Band I 50μm pixel size configuration.

An unobscured two off-axis aspherical design was always within the realm of possibility for Bands II and III (100μm pixel), but it was once again revisited for use in Band I due to a change in the baseline pixel size to 75μm for all three bands. The collimator was allowed to be an aspheric mirror and was increased in focal length. A baseline unobscured two off-axis parabola system design with fold mirrors was generated for the baseline 75μm pixel case for all three bands. This design accommodated both wide- and narrow-field modes. Space for beamsplitters and filter wheels were also allotted. Figure 7-1 is an optical schematic of this reflective IRAC system design.

The first parabola serves as a collimator for all three bands. There is a second parabola for each band which serves as an imager. A 134 $\times$ 134* baseline pixel array was used. This resulted in a 10.05mm detector array size and a corresponding IRAC wide-field magnification of 0.339 (F/8.129) for the baseline pixel size of 75μm. Figure 7-1 also shows that space has been allotted for a fourth band (60μm $\rightarrow$ 120μm) beamsplitter between the wide-field primary and first wide-field fold mirror. Therefore Band IV would only operate in the wide-field mode. If Bands II, III, and IV have larger pixel sizes than the baseline 75μm (therefore different size arrays) then the specific magnification required for each band will be accommodated by each band's secondary focal length.

7.5.2 Implementation of Magnification Change

The magnification switch from wide- to narrow-field mode or vice versa is accomplished by moving the following optical components via a mechanism:

(1) Wide-Field Fold Mirror – following the wide-field primary (collimator).

(2) Narrow-Field SIRTF Fold Mirror

(3) Narrow-Field Fold Mirror – following the narrow field primary (collimator)†

(4) Narrow-Field Pupil Stop†

*Allows for six inactive pixels between four 64 $\times$ 64 arrays butted together.
†In the current design (January 1988) only two mirrors must be moved to effect the mode change.[10]

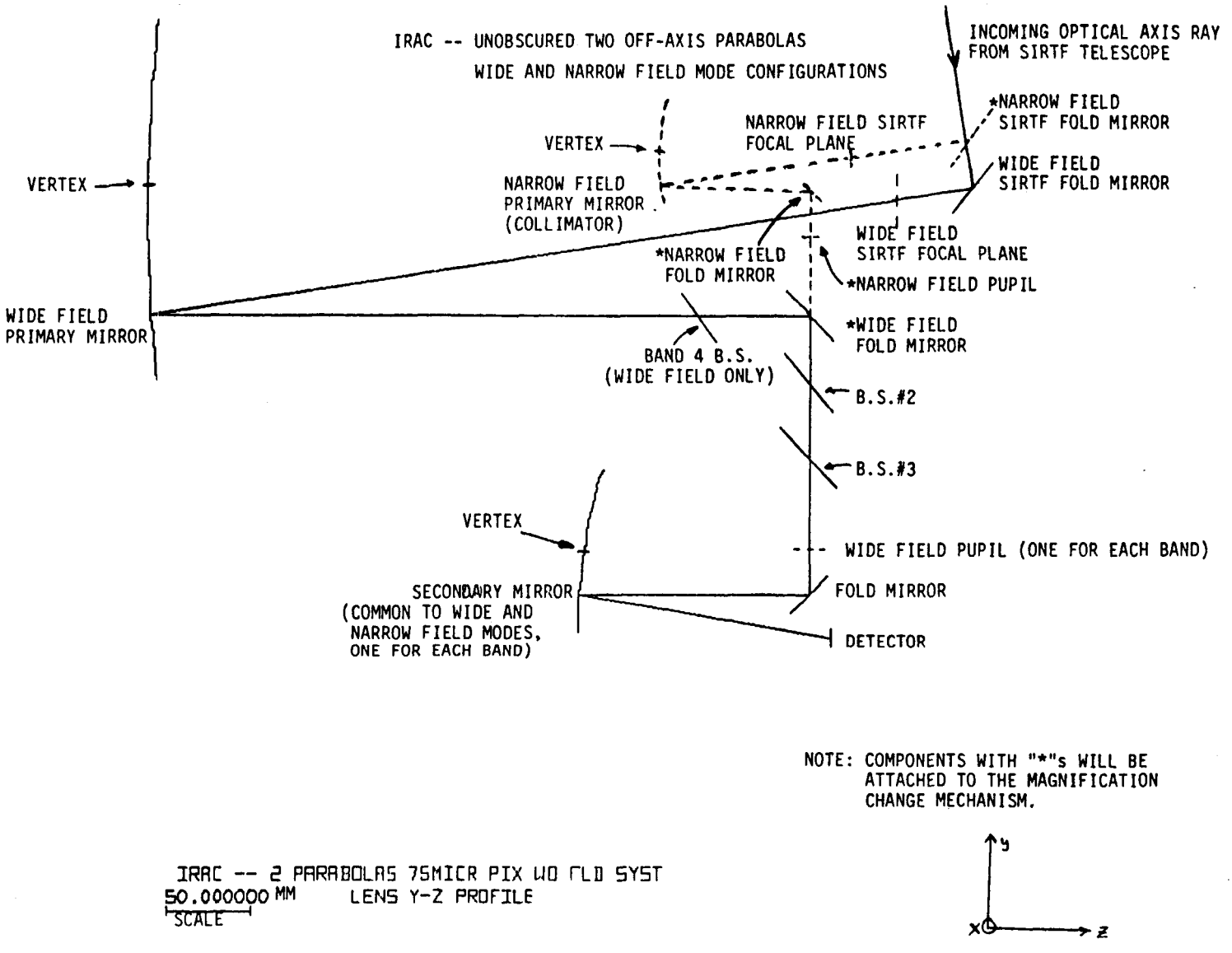

Figure 7–1. Optical Schematic of Reflective IRAC System Design

7.5.3 Physical Layout Consideration

A conclusion can not be made on the space availability for the three beamsplitters, four filter wheels, and the detector until this design has been laid out within the MIC. Space must be allotted for mounts and alignment adjustments. The beamsplitters and filter wheels are placed in collimated light (between the primary mirror and secondary mirror of each band where there would be no wavelength spread in the passband of an interference filter for any one point on the focal plane). The filter wheels probably could not be located on the image side of the secondary mirror. This is due to the design being slightly non-telecentric (approximately two degrees in the narrow field). There is one narrow-field pupil which is common to all three bands. To insert the narrow-field mode into the system along with the wide-field mode necessitated having a separate wide-field pupil for each of the four bands (4 pupil stops). This will be a problem if it is necessary to place the calibration sources at the edge of the wide-field pupils. The alternative is to have these calibration sources placed at the center of the SIRTF secondary (aperture stop). This is where they could serve all of the SIRTF experiments.

7.5.4 Analytical Results

The first step in determining this design's performance was to perform a geometrical analysis. This was done by simply tracing 300 rays through the system for each particular field angle. Table 7-1 lists the geometric 80% EESDs for the wide- and narrow-field modes respectively. All tables are based on a Band I array size of 134 $\times$ 134 pixels.

A diffraction image quality analysis was performed to determine the real spot sizes and MTF's of the system. Tables 7-2 and 7-3 list the diffraction 80% EESDs for the Band I wide- and narrow-field modes respectively. Figure 7-2 shows the worst case (corner of field) radial energy distribution plots for the BandI wide-field case. Band I does not meet the wide-field specification for wavelengths between 2.76μm and 4.09μm. The Band I narrow-field specification is not met for wavelengths less than 2.63μm. Tables 7-4 and 7-5 list the worst case diffraction 80% EESDs for Bands II and III respectively for both the wide- and narrow-field modes. Both Bands II and III are well within the wide- and narrow-field specifications. The geometric and diffraction analyses represent the IRAC optical performance independent of the SIRTF telescope.

Further optimization of the design may achieve full Band I success. The Band I secondary mirror may have to be a nonparabolic asphere. An alignment sensitivity analysis is currently being performed as part of the optimization of this design. This involves misaligning each optical element, one at a time, until the worst case 80% EESD exceeds the specification.

Wide-Field Case (FOV=300 arcsec; F#=8.13)

X Field Angle (arcsec)	Y Field Angles (arcsec) -150 arcsec	0 arcsec	150 arcsec
0 arcsec	54.2μ	46.0μ	38.8μ
75 arcsec	54.6μ	46.5μ	40.1μ
150 arcsec	55.0μ	47.2μ	43.2μ

Narrow-Field Case (FOV=75 arcsec; F#=32.52)

X Field Angle (arcsec)	Y Field Angles (arcsec) -75 arcsec	0 arcsec	75 arcsec
0 arcsec	49.8μ	3.2μ	34.7μ
37.5 arcsec	55.4μ	15.1μ	35.2μ
75 arcsec	68.7μ	31.8μ	38.4μ

Notes: (1) Encircled Energy Values are for a flat and titled focal surface.
(2) Spot Sizes are symmetric about the Y−Z plane.
(3) These Geometric Spot Sizes are measured in reference to the optimized geometric focal-plane position.

Table 7−1. Geometric Analysis − 80% Encircled Energy Diameter (Microns)
Infrared Array Camera (IRAC) Optical Design Evaluation
Configuration: Two Off-Axis Unobscured Parabolas
For all 3 Bands: (Pixel Size = 75μ)

Band I: 75 Micron Pixel Optical Design Data
Wide-Field Case (FOV = 300 arcsec)
Diffraction Analysis

Band I ($2\mu - 5\mu$)	Wide-Field Diff. Limit.	Specification Requirement	X Field Angle (arcsec)	Y Field Angles (arcsec) -150	0	150
λ=2μ	39.7μ	<75.0μ	0	67.2μ	60.6μ	51.3μ
			75	67.0μ	60.2μ	51.8μ
			150	67.0μ	59.7μ	54.0μ
λ=2.76μm	54.8μ	<75.0μ	0	75.0μ	74.2μ	74.0μ
			75	69.4μ	69.4μ	69.6μ
			150	60.8μ	58.1μ	57.9μ
λ=3μ	59.5μ	<75.0μ	0	75.6μ	71.6μ	58.4μ
			75	76.1μ	71.4μ	58.4μ
			150	77.4μ	71.2μ	61.9μ
λ=4μ	79.3μ	<79.3μ	0	77.9μ	69.4μ	60.1μ
			75	78.4μ	67.3μ	60.0μ
			150	81.5μ	63.9μ	60.4μ
λ=4.09μ	81.1μ	<81.1μ	0	81.1μ	77.9μ	77.3μ
			75	62.1μ	65.9μ	68.2μ
			150	61.5μ	61.3μ	61.3μ
λ=5μ	99.2μ	<99.2μ	0	75.6μ	75.0μ	73.8μ
			75	75.5μ	74.7μ	73.8μ
			150	75.7μ	74.4μ	74.0μ

Notes:
(1) Encircled energy values are for a flat and titled focal surface.
(2) Spot sizes are symmetric about the Y−Z plane.
(3) These diffraction spot sized are measured in reference to the diffraction optimized focal-plane position.

Table 7−2. 80% EESDs for Band I (Wide Field)
Infrared Array Camera (IRAC) Optical Design Evaluation
Configuration: Two Off-Axis Unobscured Parabolas
Band I: (Pixel Size = 75μ; Wide Field F#=8.13)

Band I: 75 Micron Pixel Optical Design Data
Narrow-Field Case (FOV = 75 arcsec)
Diffraction Analysis

Band I (2μ--5μ)	Narrow-Field Diff. Limit.	Sampling Requirement	X Field Angle (arcsec)	Y Field Angles (arcsec) -75	0	75
$\lambda=2\mu$	$<158.7\mu$	$>150\mu$	0	117.5μ	114.5μ	115.5μ
			37.5	117.8μ	114.4μ	115.4μ
			75	119.4μ	115.2μ	115.7μ
$\lambda=2.63\mu$	$<208.7\mu$	$>150\mu$	0	153.0μ	150.4μ	151.0μ
			37.5	153.1μ	150.3μ	150.7μ
			75	154.1μ	150.8μ	150.8μ
$\lambda=3\mu$	$<238.0\mu$	$>150\mu$	0	174.0μ	171.7μ	171.8μ
			37.5	174.0μ	171.4μ	171.5μ
			75	174.8μ	171.7μ	171.5μ
$\lambda=4\mu$	$<317.4\mu$	$>150\mu$	0	230.8μ	228.8μ	228.4μ
			37.5	230.7μ	228.4μ	228.0μ
			75	231.2μ	228.4μ	227.7μ
$\lambda=5\mu$	$<396.7\mu$	$>150\mu$	0	288.0μ	286.1μ	285.2μ
			37.5	287.6μ	285.4μ	284.5μ
			75	287.8μ	285.2μ	284.1μ

Notes: (1) Encircled energy values are for a flat and titled focal surface.
(2) Spot sizes are symmetric about the Y−Z plane.
(3) These diffraction spot sized are measured in reference to the diffraction optimized focal-plane position.

Table 7−3. 80% EESDs for Band I (Narrow Field)
Infrared Array Camera (IRAC) Optical Design Evaluation
Configuration: Two Off-Axis Unobscured Parabolas
Band I: (Pixel Size = 75μ; Wide Field F#=32.52)

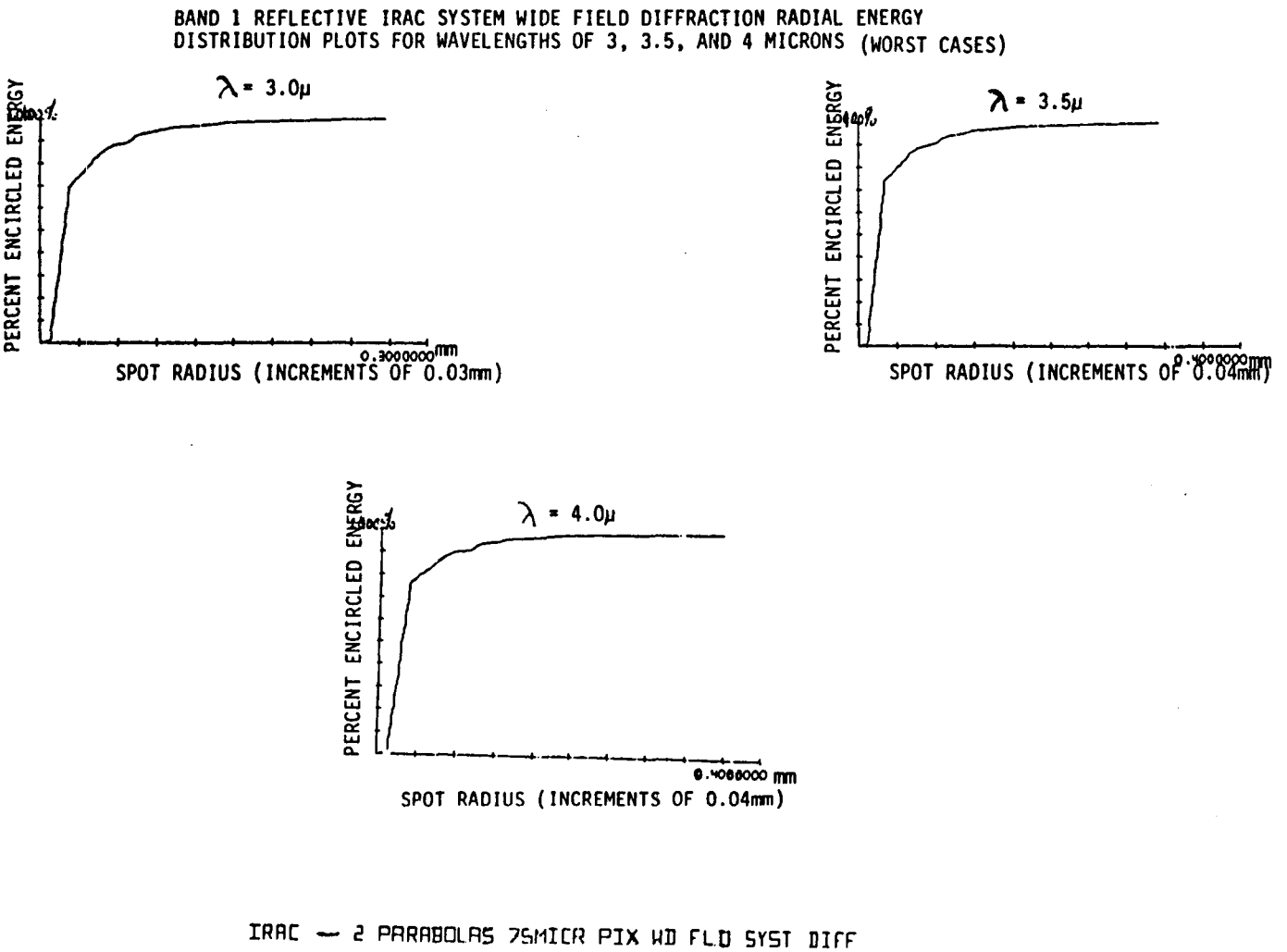

Figure 7–2. Worst Case Radial Energy Distribution Plots for Band I

Worst Case Diffraction

Band II (5μ->18μ)	Wide-Field Diff. Limit.	Specification Requirement	Wide-Field Case (FOV=300arcsec;F#=8.13) Worst Case Diffraction 80%EESD (microns)
λ=5μ	99.2μ	<99.2μ	75.7μ
λ=7μ	138.9μ	<138.9μ	103.2μ
λ=10μ	198.4μ	<198.4μ	145.6μ
λ=13μ	257.9μ	<257.9μ	188.2μ
λ=16μ	317.4μ	<317.4μ	231.1μ
λ=18μ	357.1μ	<357.1μ	259.7μ

Band II (5μ->18μ)	Wide-Field Diff. Limit.	Sampling Requirement	Narrow-Field Case (FOV=75arcsec;F#=32.52) Worst Case Diffraction 80%EESD (microns)
λ=5μ	<396.7μ	>150μ	288.0μ
λ=7μ	<555.4μ	>150μ	402.4μ
λ=10μ	<793.5μ	>150μ	574.3μ
λ=13μ	<1031.5μ	>150μ	746.3μ
λ=16μ	<1269.6μ	>150μ	918.1μ
λ=18μ	<1428.3μ	>150μ	1033.0μ

Notes:
(1) Encircled energy values are for a flat and titled focal surface.
(2) Spot sizes are symmetric about the Y−Z plane.
(3) These diffraction spot sized are measured in reference to the diffraction optimized focal-plane position.

Table 7−4. Worst Case Diffraction 80% EESD (Band II)
Infrared Array Camera (IRAC) Optical Design Evaluation
Configuration: Two Off-Axis Unobscured Parabolas
Band II: (Pixel Size = 75μ)

Worst Case Diffraction

Band III (18μ->30μ)	Wide-Field Diff. Limit.	Specification Requirement	Wide-Field Case (FOV=300arcsec;F#=8.13) Worst Case Diffraction 80%EESD (microns)
λ=18μ	357.1μ	<357.1μ	259.7μ
λ=22μ	436.4μ	<436.4μ	317.0μ
λ=24μ	476.1μ	<476.1μ	345.7μ
λ=26μ	515.8μ	<515.8μ	374.4μ
λ=28μ	555.4μ	<555.4μ	403.2μ
λ=30μ	595.1μ	<595.1μ	431.8μ

Band II (18μ->30μ)	Wide-Field Diff. Limit.	Sampling Requirement	Narrow-Field Case (FOV=75arcsec;F#=32.52) Worst Case Diffraction 80%EESD (microns)
λ=18μ	<1428.3μ	>150μ	1033.0μ
λ=22μ	<1745.7μ	>150μ	1262.3μ
λ=24μ	<1904.4μ	>150μ	1377.1μ
λ=26μ	<2063.1μ	>150μ	1491.8μ
λ=28μ	<2221.8μ	>150μ	1606.5μ
λ=30μ	<2380.5μ	>150μ	1721.2μ

Notes:
(1) Encircled energy values are for a flat and titled focal surface.
(2) Spot sizes are symmetric about the Y−Z plane.
(3) These diffraction spot sized are measured in reference to the diffraction optimized focal-plane position.

Table 7−5. Worst Case Diffraction 80% EESD (Band III)
Infrared Array Camera (IRAC) Optical Design Evaluation
Configuration: Two Off-Axis Unobscured Parabolas
Band III: (Pixel Size = 75μ)

8.0 CONCLUSIONS

8.1 Array Detector Performance

The goals of the IRAC project and the results of the detector research carried out under this Grant are shown in Table 8-1 and summarized below. This table shows the best performance across the array achieved in each band.*

1. Read Noise: IRAC proposed goals (<100 e^-) have been demonstrated except in Band I where the best read noise measured to date is 240 e^- in low-doped InSb.

2. Dark Current: IRAC proposed goals (100e^-/s or 16 aA) have been demonstrated in all bands at 6°Kelvin. Bands I and III have demonstrated dark currents <2.1 aA at 8° Kelvin.

3. Responsivity: IRAC proposed goals have been met or exceeded in Bands II and III but are lower than required by a factor of 2 in Band I.

4. Power Dissipation: IRAC proposed goals (<26 mW per 64 × 64 array) have been demonstrated in all bands with 1 mW per array a typical value for the array alone. Additional power may be required for operation of heaters, temperature control circuits and line drivers.

5. Integration Time: IRAC proposed goals (1000 s, all bands) are within reach. Integration times up to 500 s have been demonstrated in Band I with no read noise increase and up to 30 minutes in Band III with read noise at 200 s only a factor of 2 higher than at integration times of 0.2 s.

6. Linear Range Well Capacity: IRAC proposed goals are within reach. Linear range well capacities of 2×10^5 e^- have been demonstrated in all bands.

7. Operating Temperatures: Optimum array operating temperatures have been determined to be in the 6°−10° kelvin range.

*At the time of the SIRTF Instrument Requirements Review (December 1987). Subsequent work in Bands II and III have demonstrated read noise results at the 60 e^- level.

IRAC Band	I	II	III
Detector Material Detector Type	**Low-doped InSb** **Photovoltaic****	**Si:Ga** **Photoconductor**	**Si:Sb** **Photoconductor**
Wavelength Range (μm)	1.4 - 5.3	5.3 - 14	14 - 30
Format	58 X 62	58 X 62	58 X 62
Pixel Size (μm)	75	75	75
Multiplexer	Direct Readout Switched MOSFET (CRC-228)	Direct Readout Switched MOSFET (CRC-228)	Direct Readout Switched MOSFET (CRC-228)
Capacitance/pixel (pF)	0.55	0.07	0.06
Quantum Efficiency* (%)	42 @3.3μm	30 (est.)	30 (est.)
Operability (%)	> 98	> 99	> 99
Responsivity (A/W)	1.2 @ 5μm	5.1 @ 11μm	≥ 3.8 @ 25μm
Responsivity Uniformity (%)	38	8	5
NEP*** (Watts/Root-Hz)	1.50E-17	2.00E-17	2.70E-17
Read Noise (e-)	240 (typ.)	100	100
Dark Current (aA)	0.2 @ 8° K	30 @ 8° K	2.07 @ 8° K
Well Size for Linear Range (e-)	1.5E+05	5.0E+05	2.0E+05
Manufacturer	SBRC	SBRC	SBRC
IRAC Contact	J. Pipher W. Forrest University of Rochester	C. McCreight Ames Research Center	C. McCreight Ames Research Center

* Not AR Coated. AR Coated Arrays RH2 and RH4 have shown QE values in the 50 - 77% range

** For SCA002

***Integration Time = 0.2 s

Table 8–1. IRAC Array Development Status

8.2 Beamsplitters

IRAC proposed goals have been demonstrated in all bands except in the $20-30\mu m$ range where improved transmission efficiency is required.

8.3 Optical Design

Table 8-2 summarizes the status of refractive and reflective design studies relative to meeting IRAC design specifications. After performing the diffraction analyses on the refractive designs, only the Band I silicon/germanium doublet design was able to meet the specifications for the $50\mu m$ pixel size case. The unobscured two off-axis parabola $75\mu m$ pixel size design met the wide- and narrow-field specifications for Bands II and III. With further optimization this reflective design should also meet specification for all of Band I for the $75\mu m$ pixel case. A $75\mu m$ pixel size refractive design for Bands I, II and III still needs to be generated. Therefore a direct comparison of the two designs can not be made at this time. A strong recommendation must be given to the reflective design if $75\mu m$ is the preferred pixel size due to its cryogenic and achromatic advantages. If there is a Band IV ($60\mu m \rightarrow 100\mu m$), it would be very difficult to design a refractive imager due to the lack of optical materials that both transmit in Band IV and have low dispersion across the band. From this design study it now appears that a pixel size smaller than $75\mu m$ will be very difficult to accommodate in this reflective design.*

*Current (January 1988) assessments indicate that the Bands II and III performance will be worse than stated due to a reduction in the physical sizes of the Band II and Band III arrays from those analyzed here. Pixel sizes are being reconsidered as part of on-going detector design work at SBRC. The latest projections of performance may be found in Reference 10.

Band	Field	REFRACTIVE DESIGNS		REFLECTIVE DESIGNS
		Hoffmann Design CsI	Achromatic Design Si/Ge	Parabolic Collimator and Parabolic Imager
#1	Narrow Wide	No No	Yes Yes	No No
#2	Narrow Wide	Yes No		Yes Yes
#3	Narrow Wide	Yes No		Yes Yes
pixel size	Spec (wide field) Band I Band 2 Band 3	DL or 50μm 100μm 100μm	DL or 50μm	Diffraction Limit or 75μm 75μm 75μm

A YES or NO addresses whether or not the specification is met. Issues such as how much "margin" exists for Yes answers is not quantified in the specification and therefore is not used as a specification requirement at this stage in the investigation. Optical margin will be examined in detail for feasible designs (i.e., designs that meet the top level specification).

Table 8–2. Status of Refractive and Reflective Design Studies

9.0 REFERENCES

1. "Technology Development of Band I Arrays for the Infrared Array Camera," Final Report, Contract SV5-55005, University of Rochester, Rochester, NY, May 1987.

2. "Fabrication and Testing of InSb 58 × 62 Element Multiplexed Infrared Detector Arrays and a Preliminary Investigation into Si:In Detector Arrays with the Same Configuration," Final Report Contract SO7-01338 (SBRC Report 71945), Santa Barbara Research Center, Santa Barbara, CA, December 1987.

3. "Band I Detector Testing Summary," University of Rochester, Rochester, NY, November 1987.

4. "IRAC Test Report Gallium Doped Silicon Band II Read Noise and Dark Current," G. Lamb, et al., NASA Technical Memorandum 87813 and IRAC-302, January 1987.

5. "Characterization of Direct Readout Si:Sb and Si:Ga Infrared Detector Arrays for Space Based Astronomy," McKelvey, et al., August 1987.

6. "Summary of ARC FY87 DRO Test Results," Ames Research Center, Moffett Field, CA, December 1987.

7. "SIRTF Beamsplitter Study," August 1, 1986, prepared by Optical Coating Laboratory, Inc., under Contract S06-08418.

8. "Pre-Definition Phase Activities for the Infrared Array Camera (IRAC)," January 1988, Final Report, Contract SV5-55002, University of Arizona, Tucson, AZ.

9. "FY86 Optical Design Activity by GSFC," P. Maymon, IRAC-402 Revision A, February 1987.

10. "Instrument Requirements Review Viewgraph Package," IRAC-114, December 1987.

APPENDIX A

SBRC Low-Doped InSb Array RH2 Test Data Histograms

Test Data Histograms

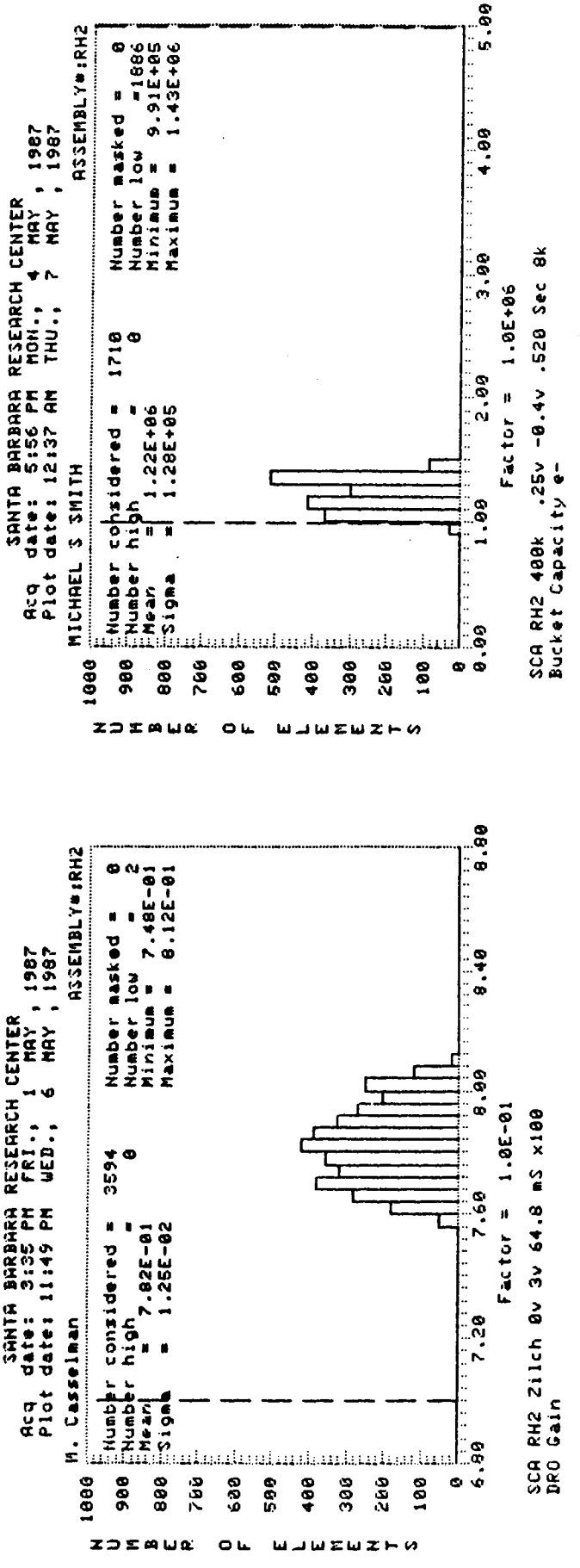

Figure A-1 Histograms of RH2 10K Source Follower Gain and Bucket Capacity

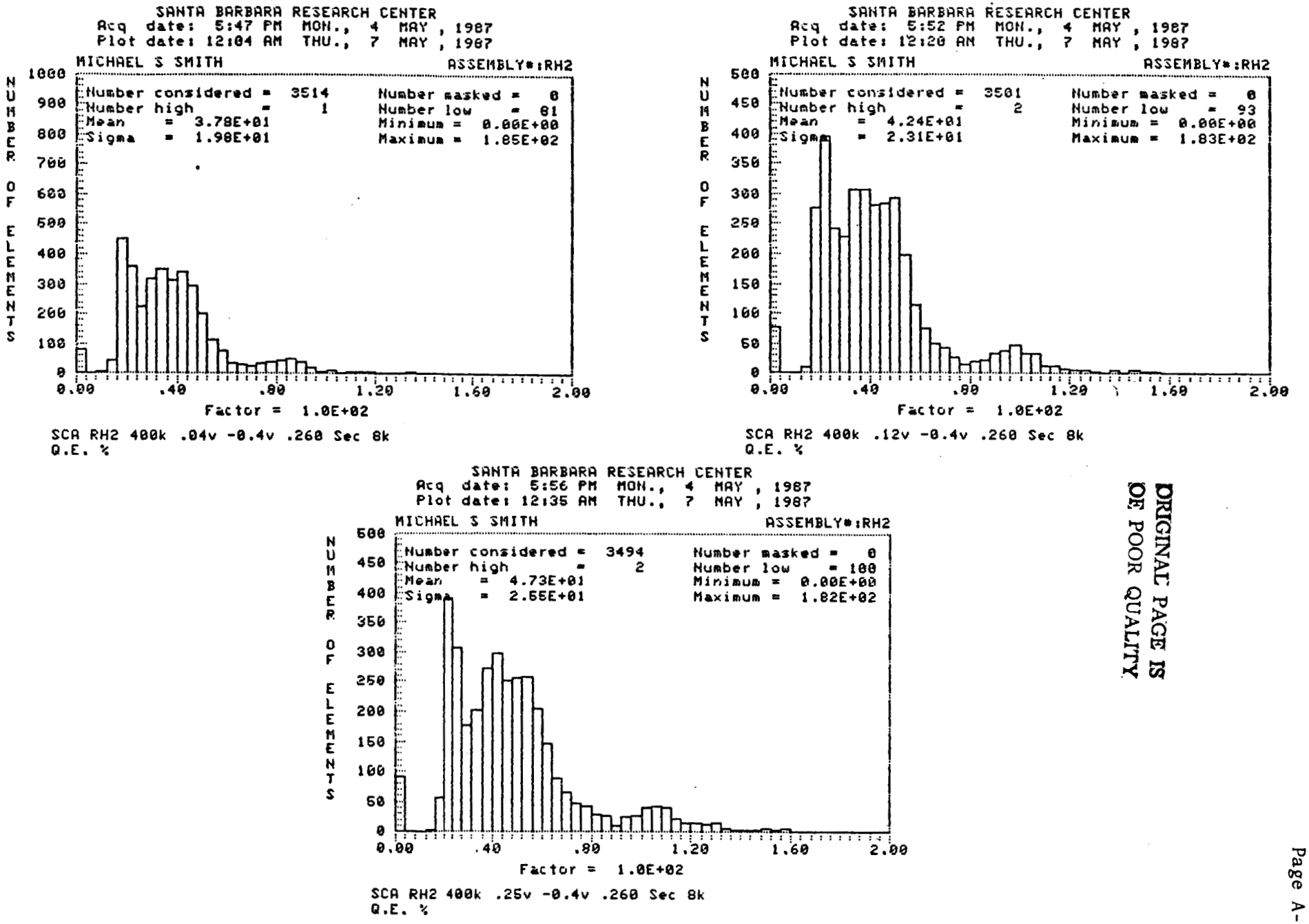

Figure A-2 Histograms of RH2 10K Quantum Eficiency

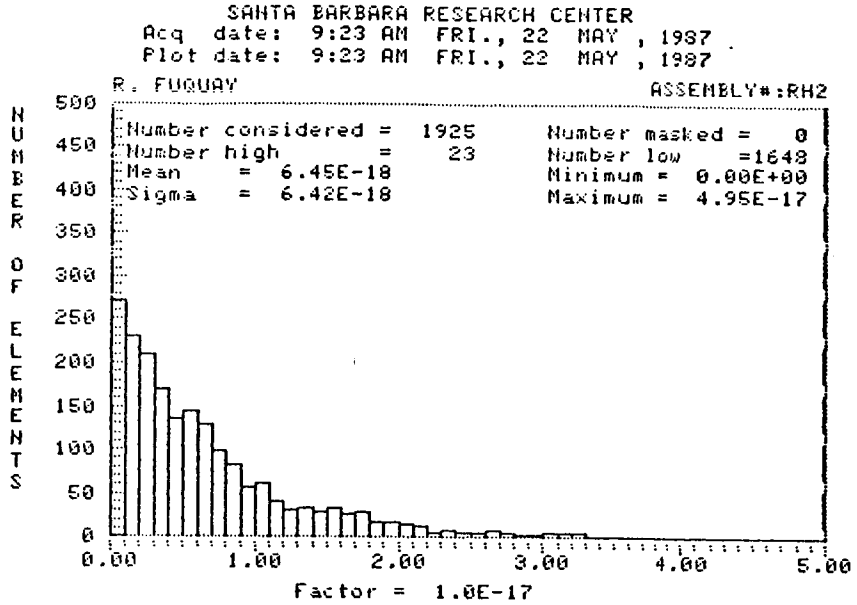

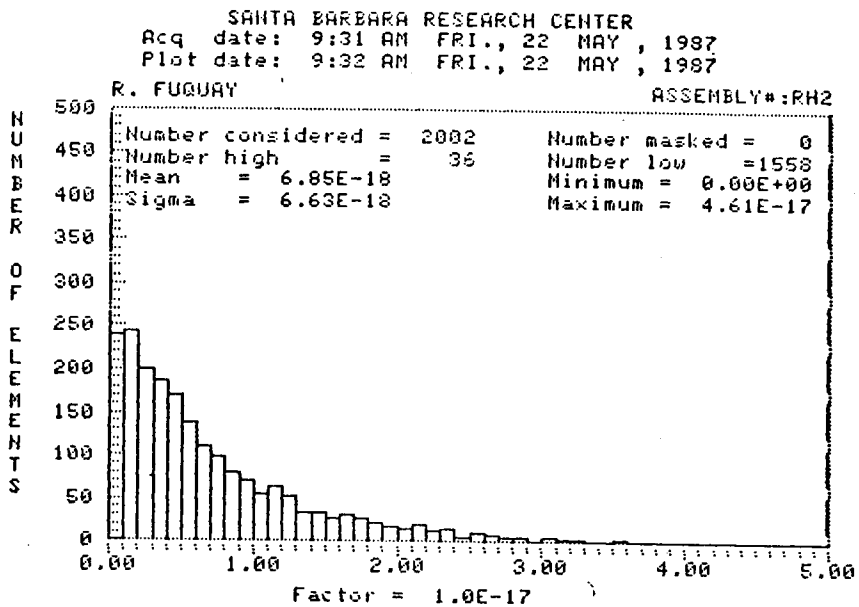

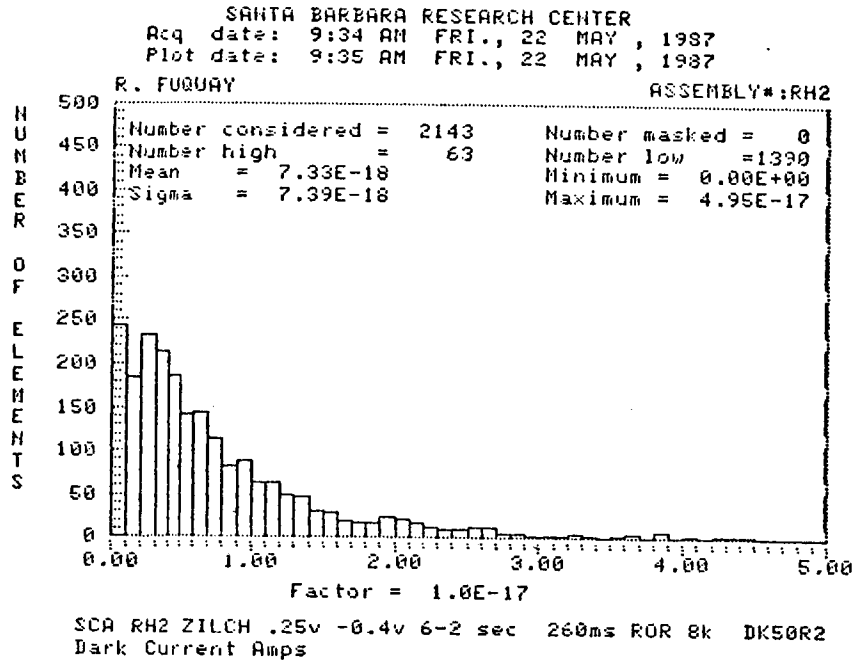

Figure A-3 Histograms of RH2 10K Dark Current - Burst Mode, 0-5 Scaling

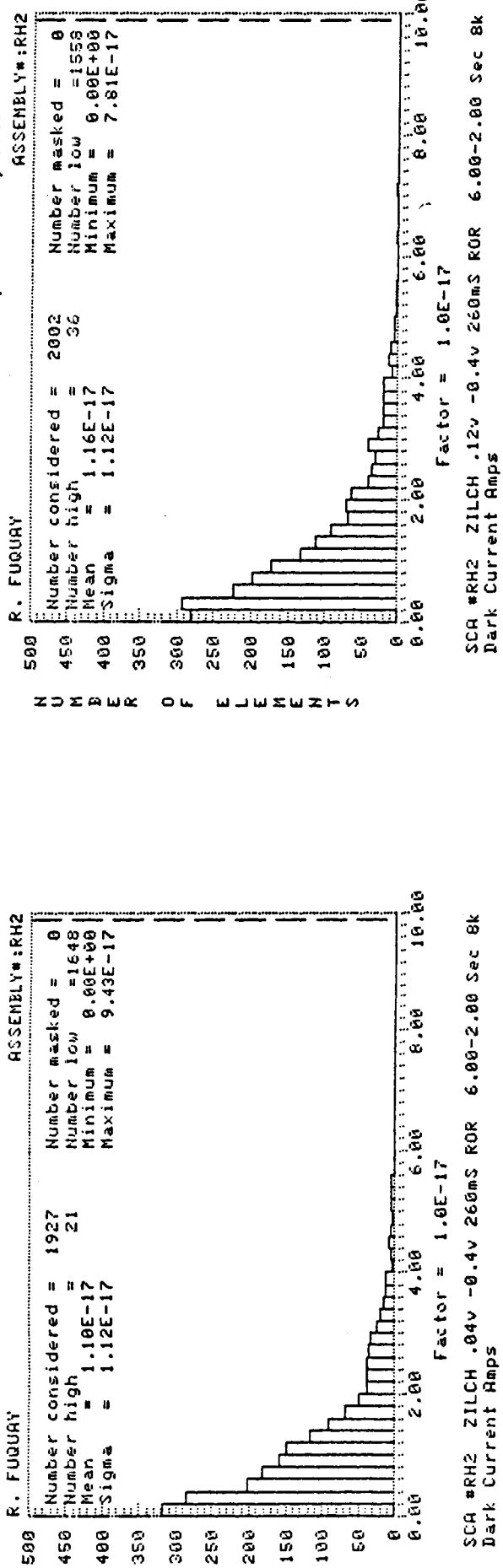

ORIGINAL PAGE IS
OF POOR QUALITY

Figure A-4 Histograms of RH2 10K Dark Current - Burst Mode, 0-10 Scaling

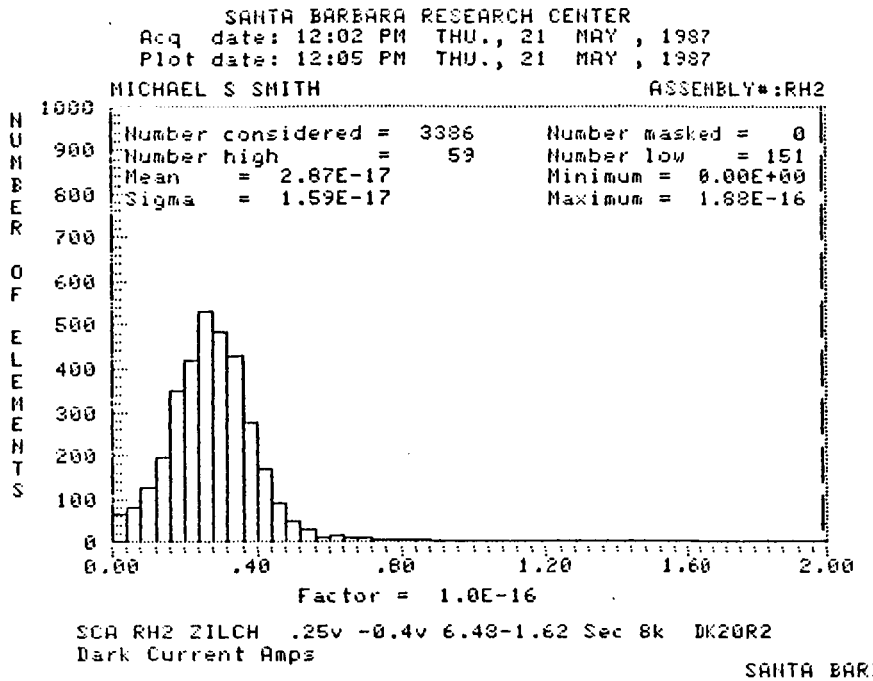

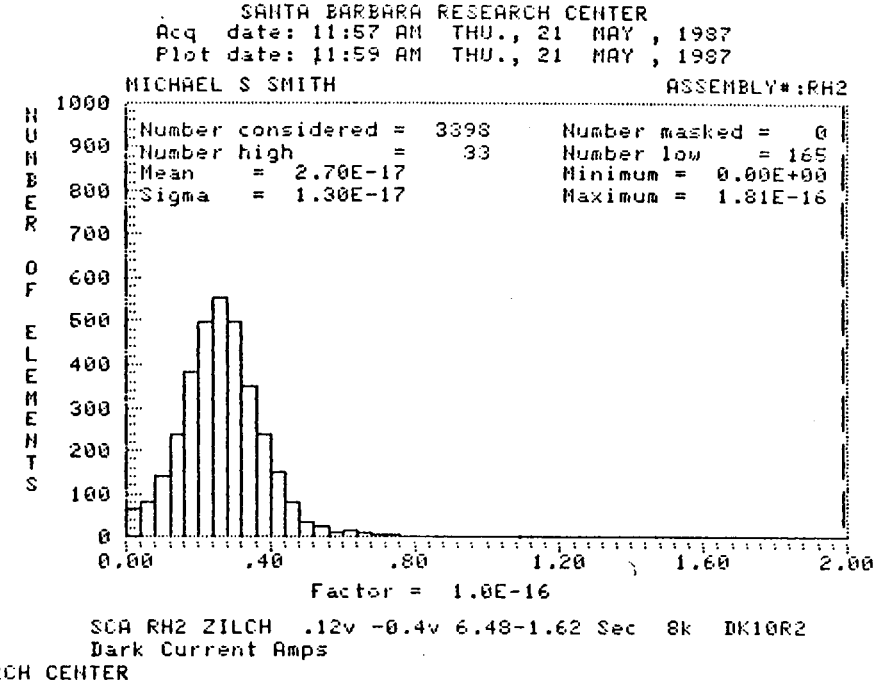

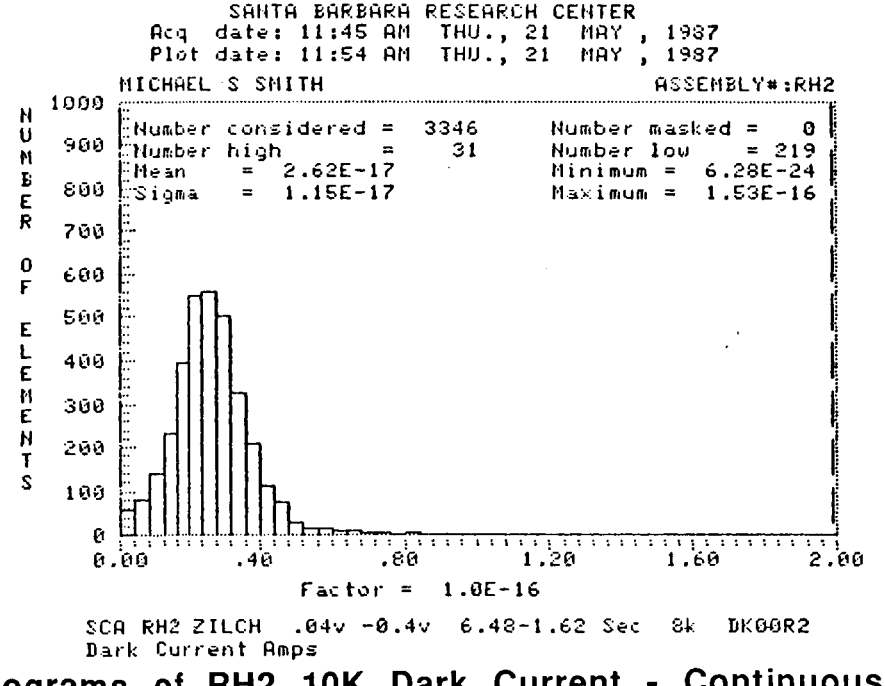

Figure A-5 Histograms of RH2 10K Dark Current - Continuous Mode, 0-2 Scaling

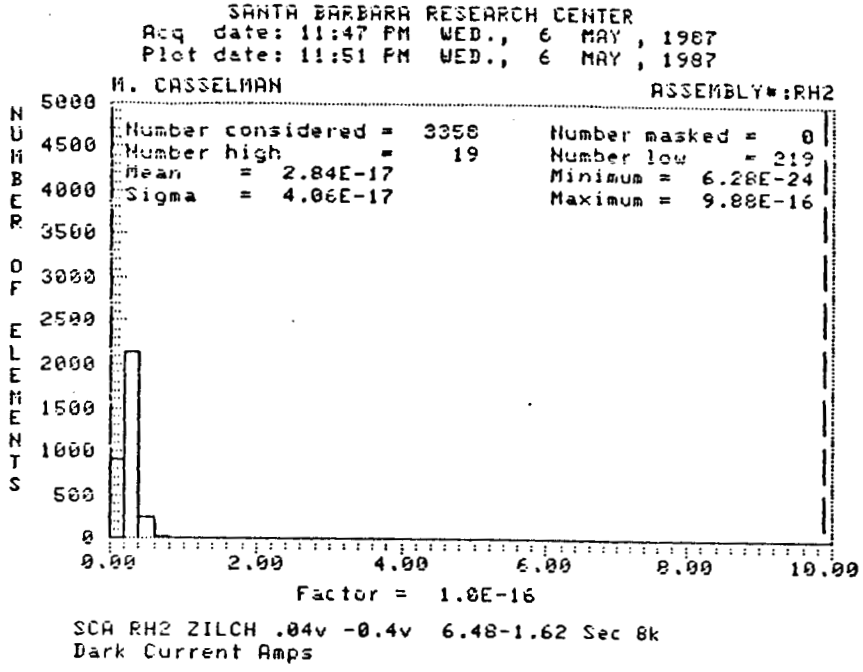

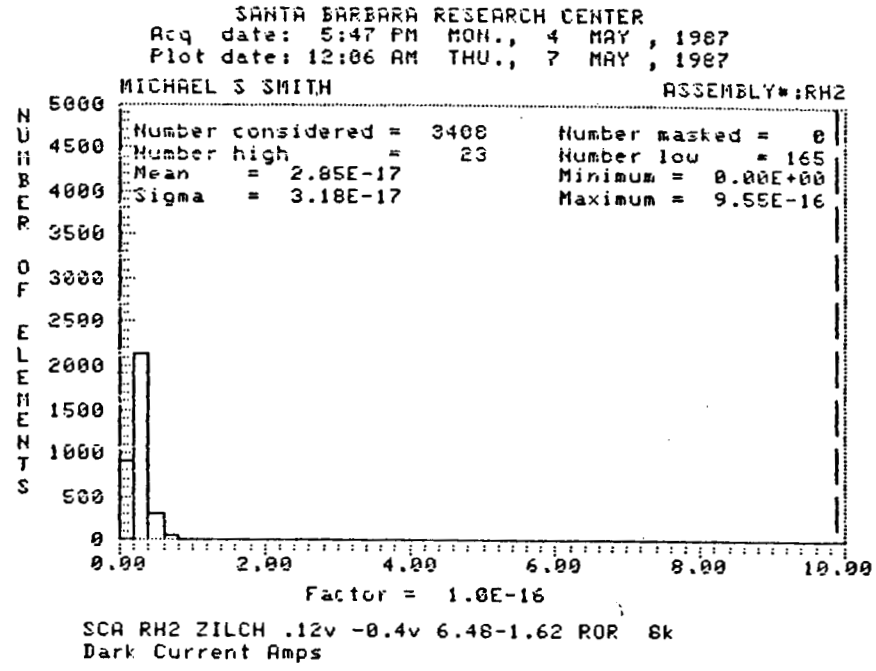

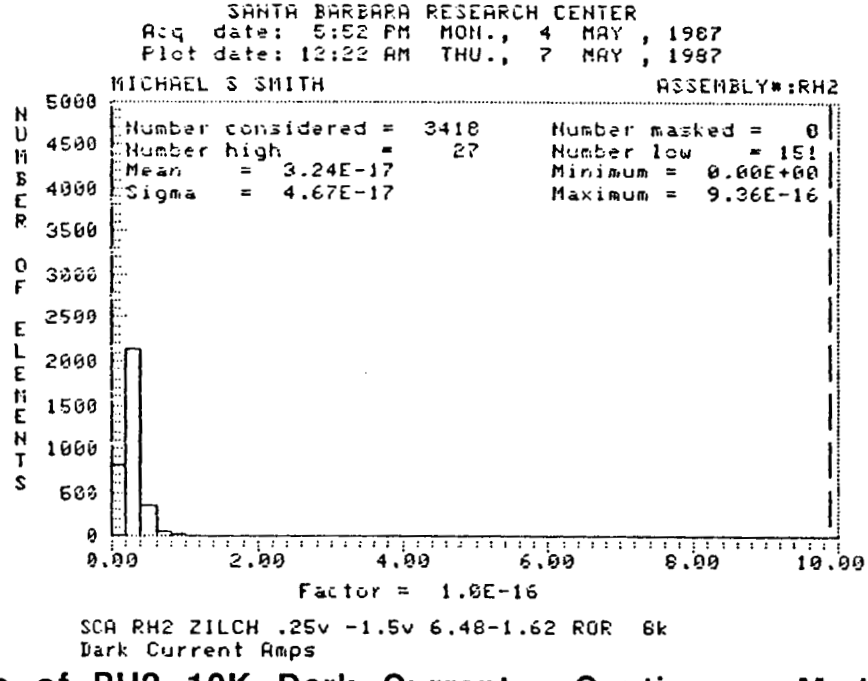

Figure A-6 Histograms of RH2 10K Dark Current - Continuous Mode, 0-10 Scaling

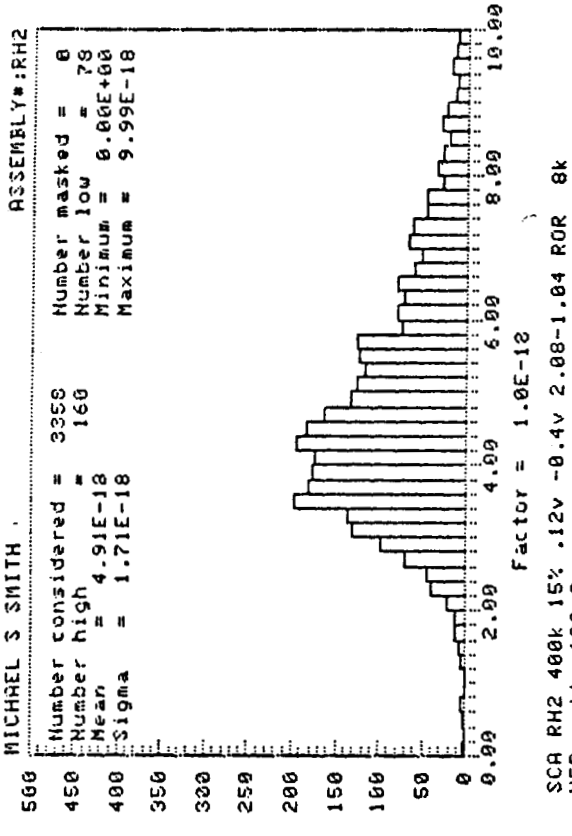

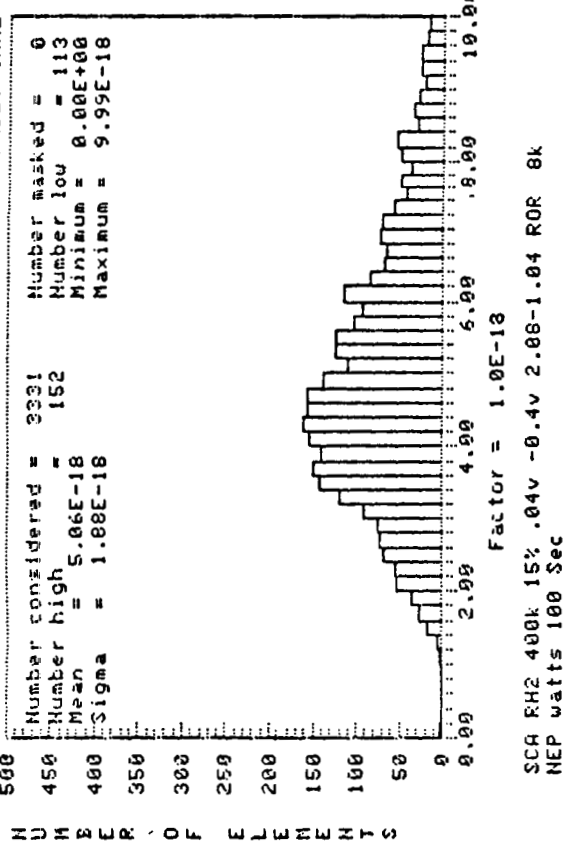

Figure A-7 Histograms of RH2 10K Noise Equivalent Power

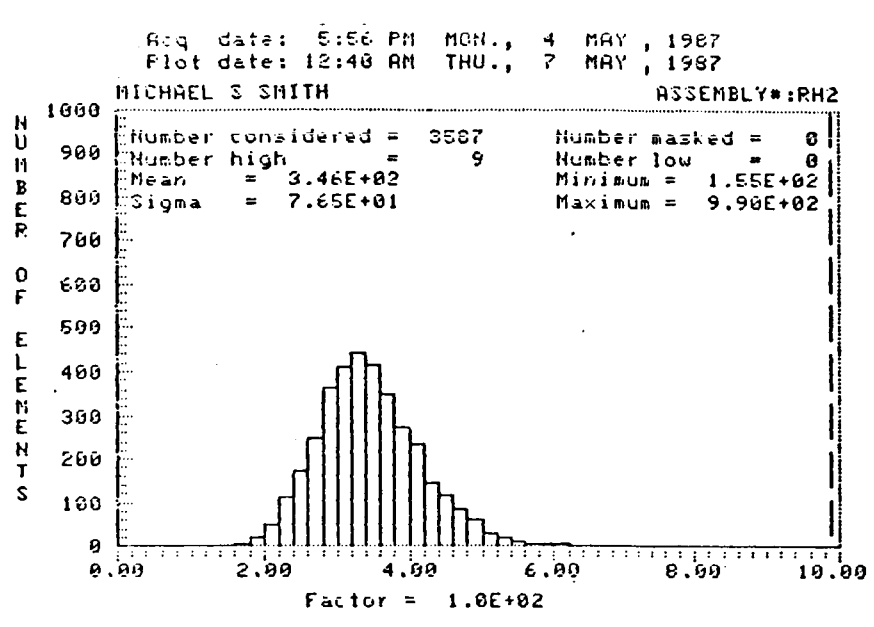

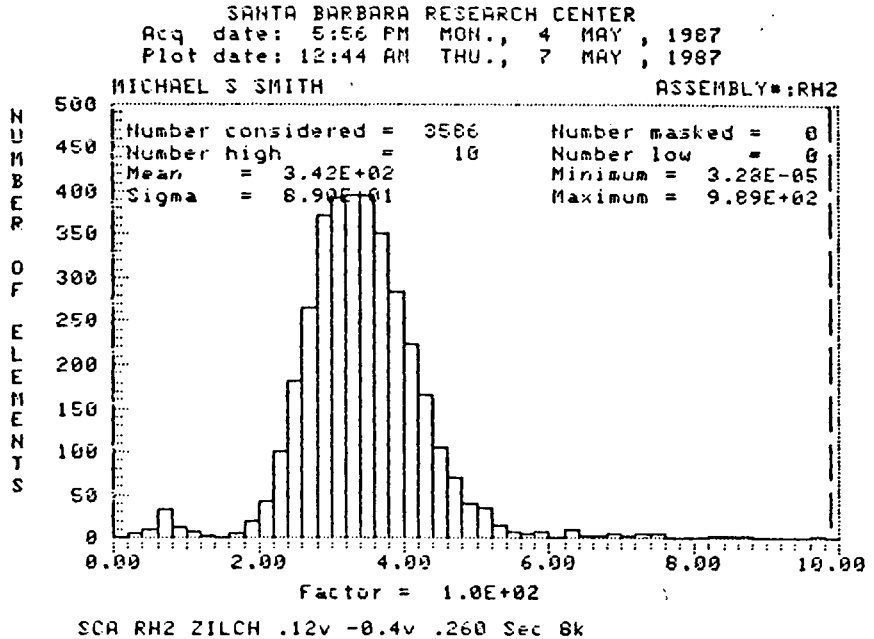

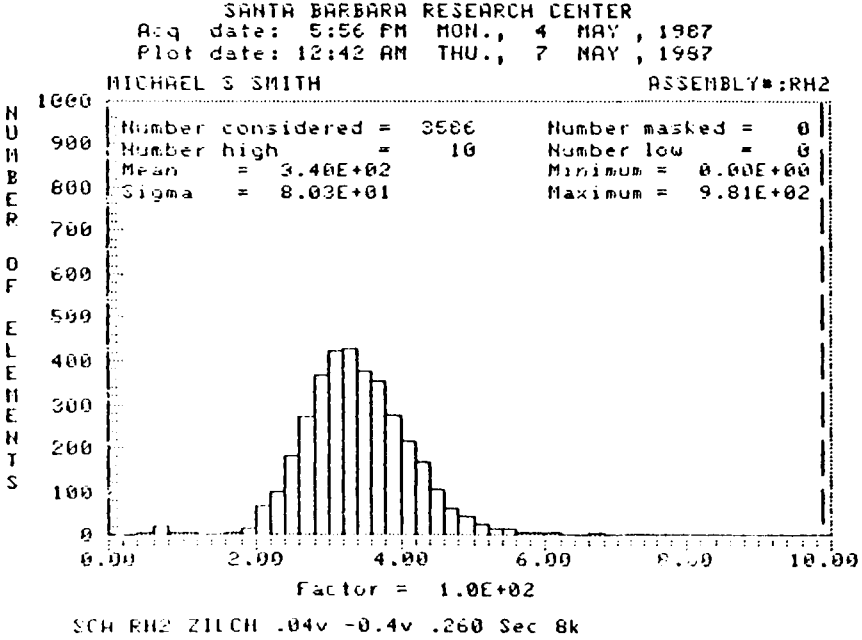

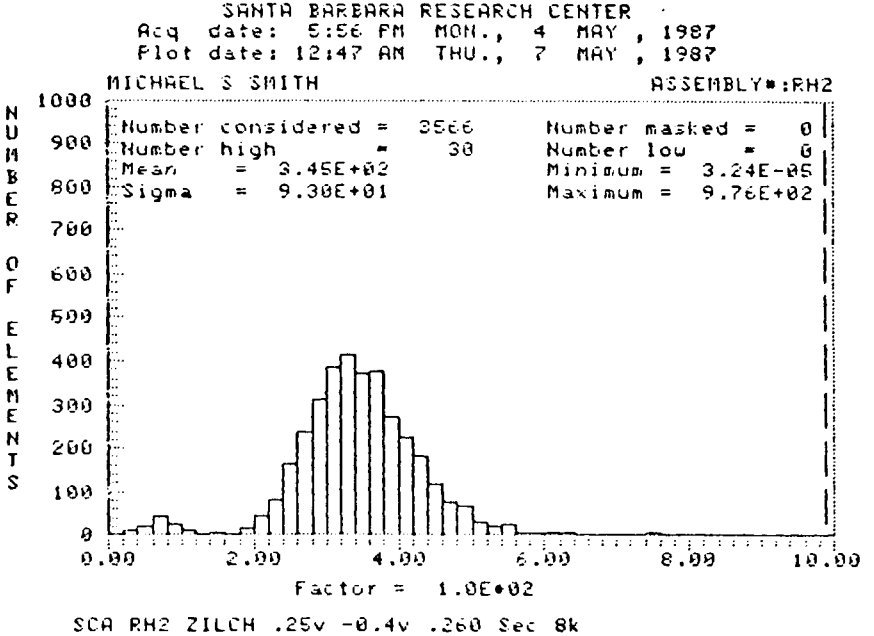

Figure A-8 Histograms of RH2 10K Noise Electrons

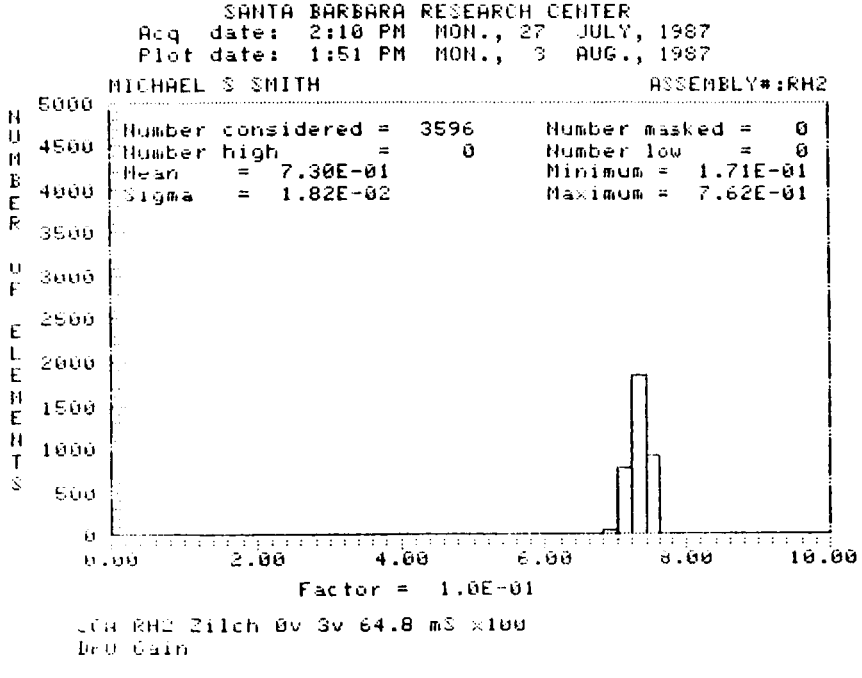

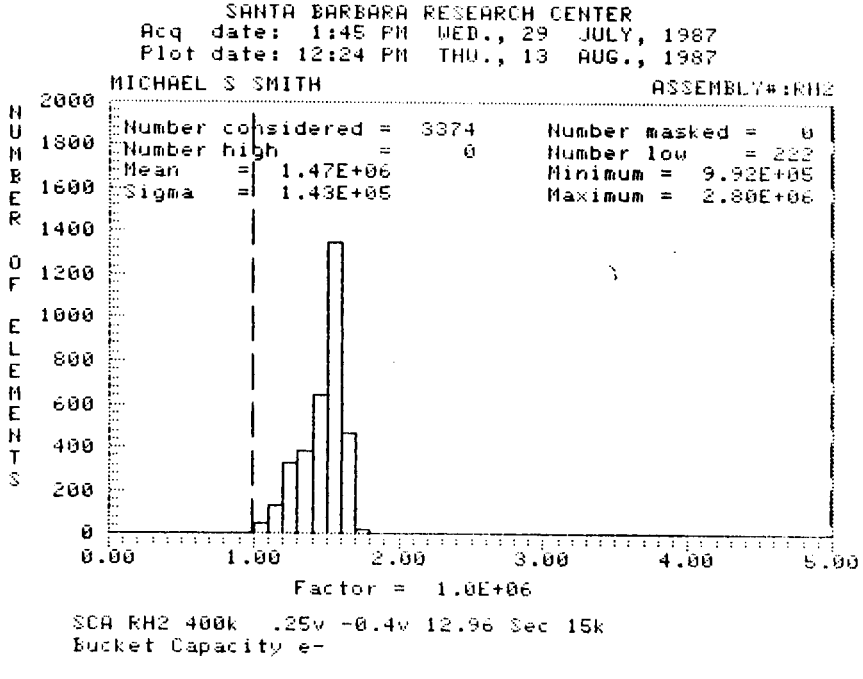

Figure A-9 Histograms of RH2 15K Source Follower Gain and Bucket Capacity

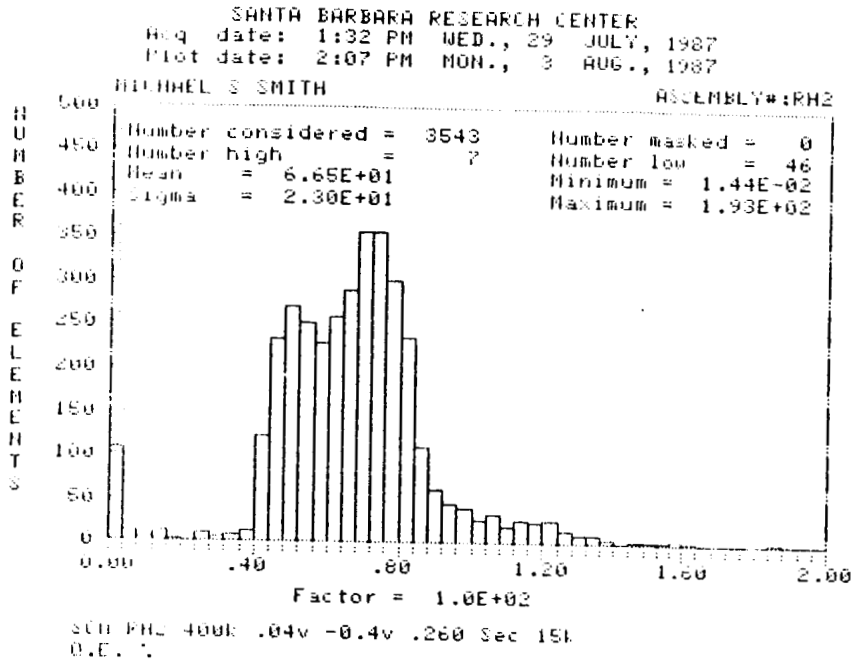

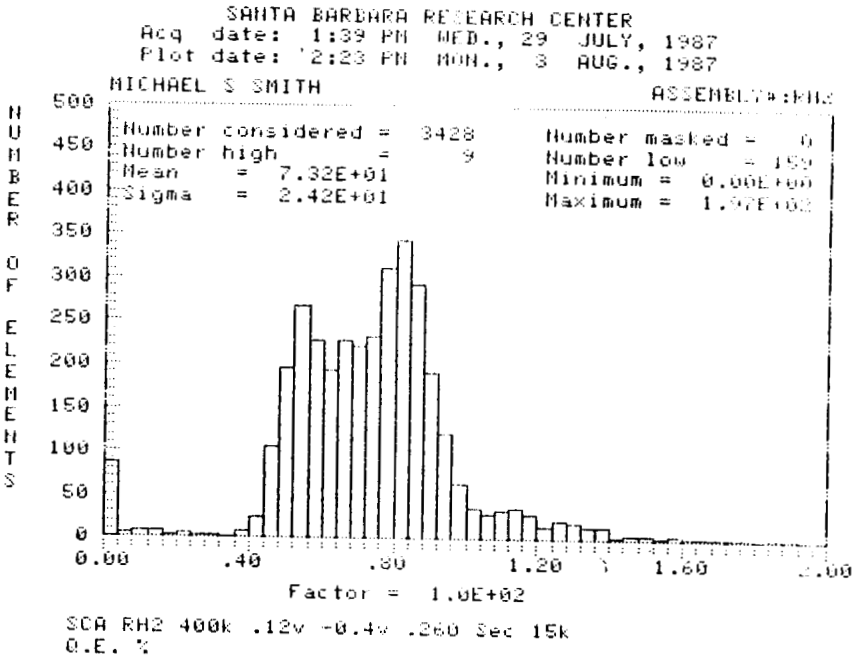

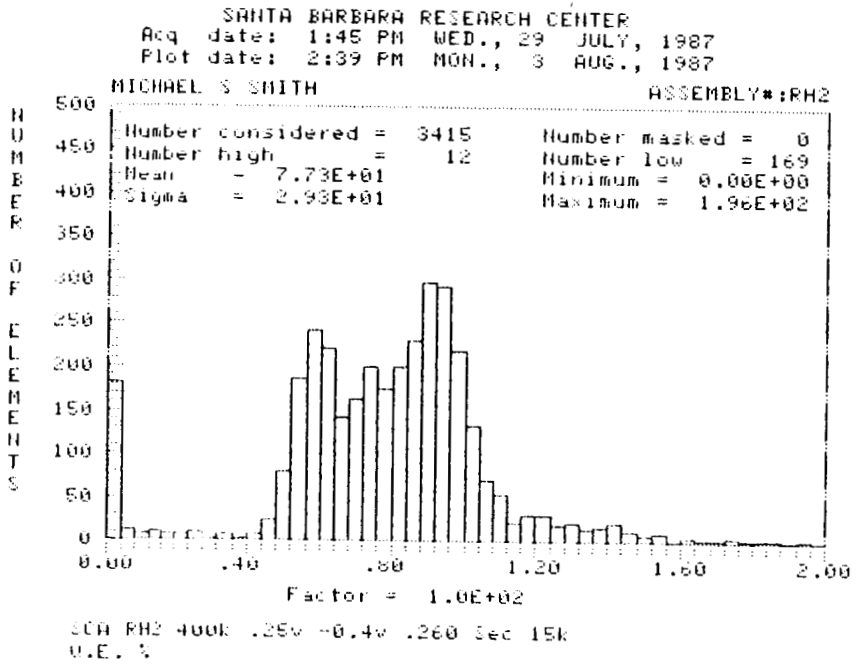

ORIGINAL PAGE IS
OF POOR QUALITY

Figure A-10 Histograms of RH2 15K Quantum Efficiency

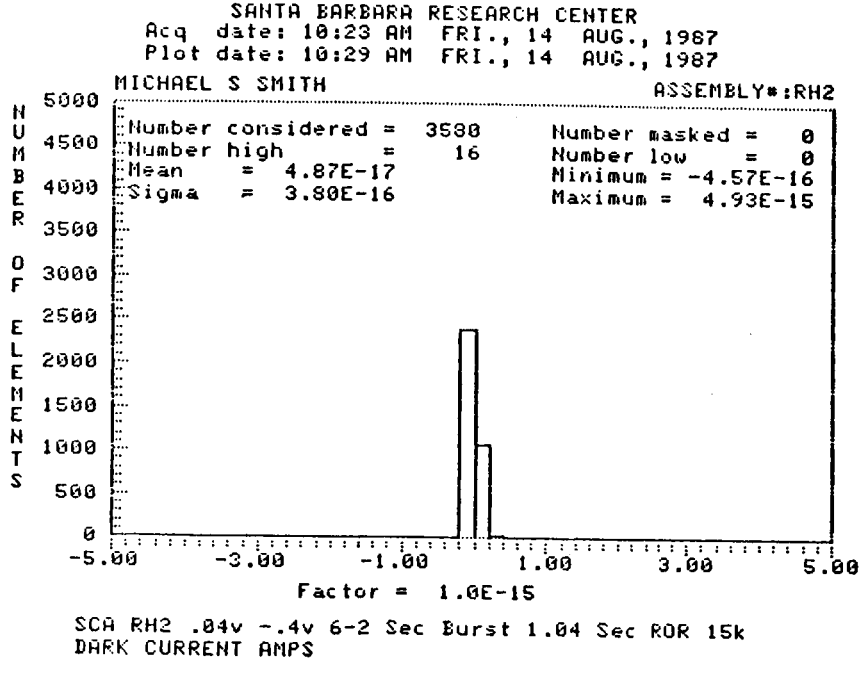

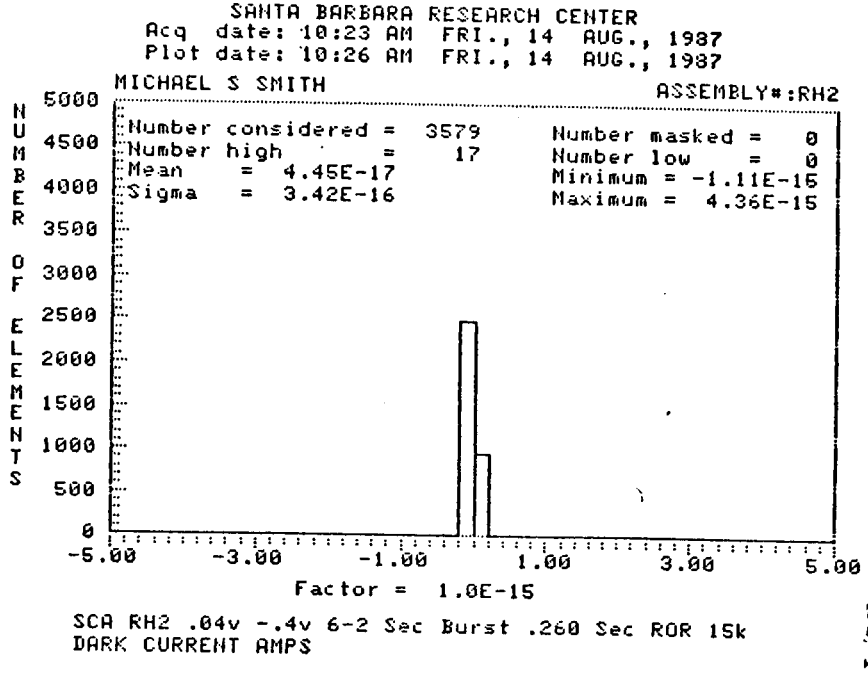

Figure A-11 Histograms of RH2 15K Dark Current - Burst Mode

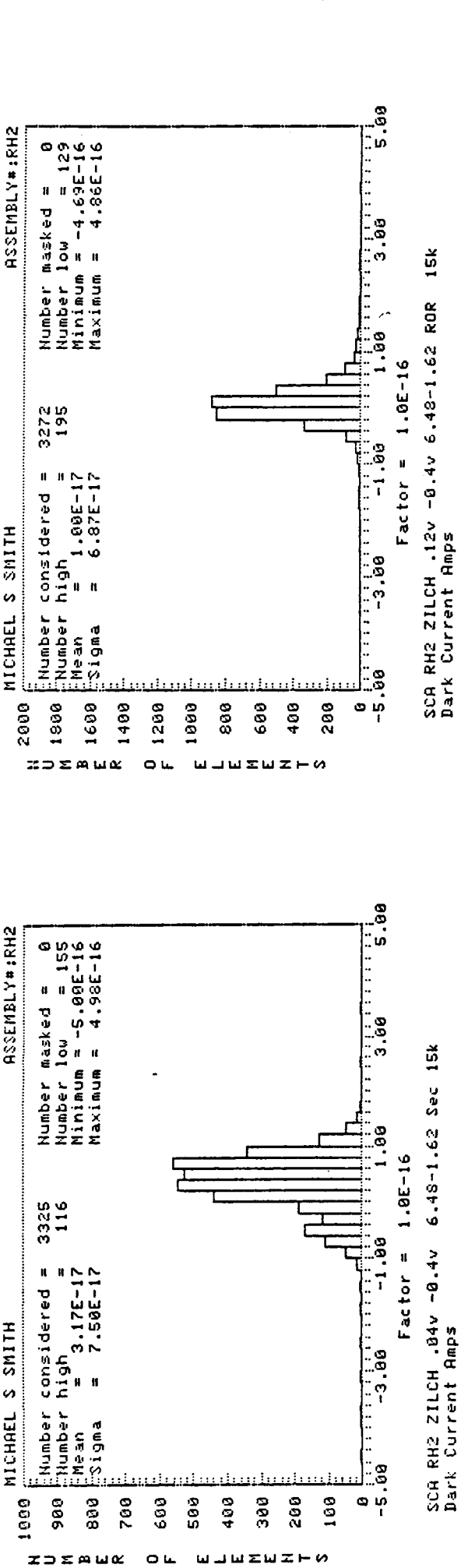

Figure A-12 Histograms of RH2 15K Dark Current - Continuous Mode, 0-2 Scaling

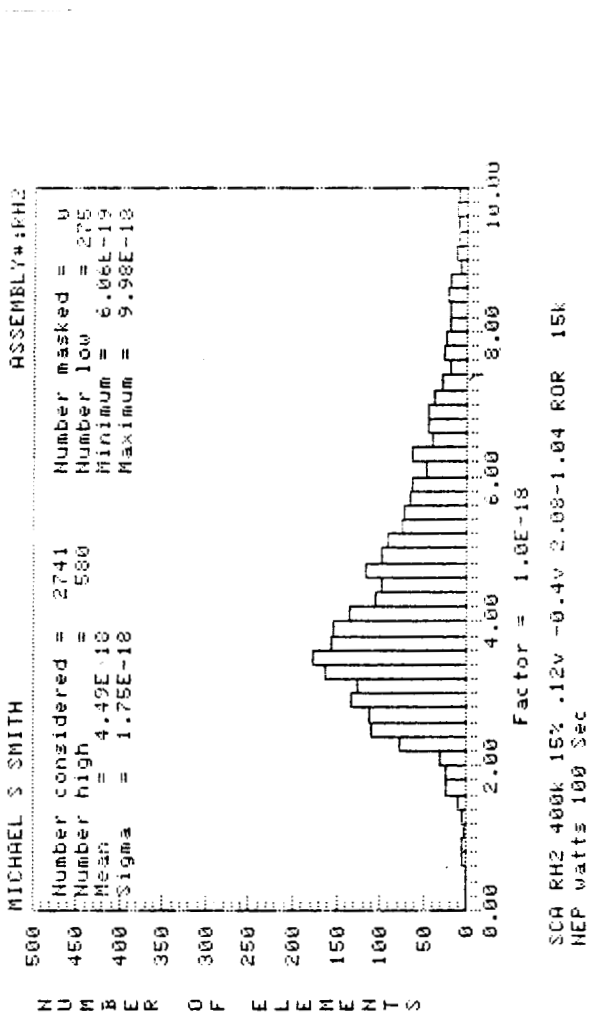

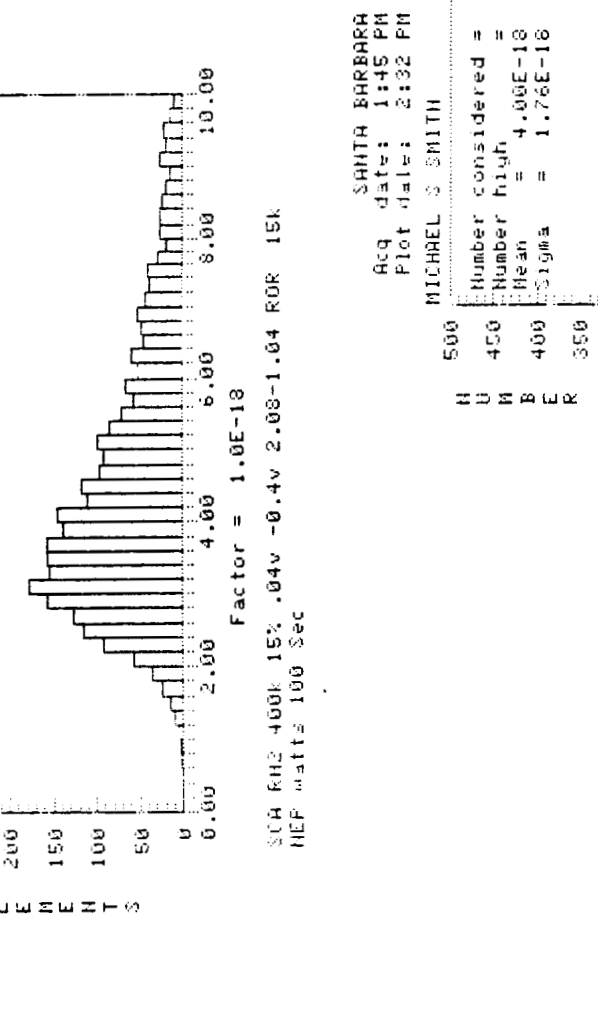

Figure A-13 Histograms of RH2 15K Noise Equivalent Power

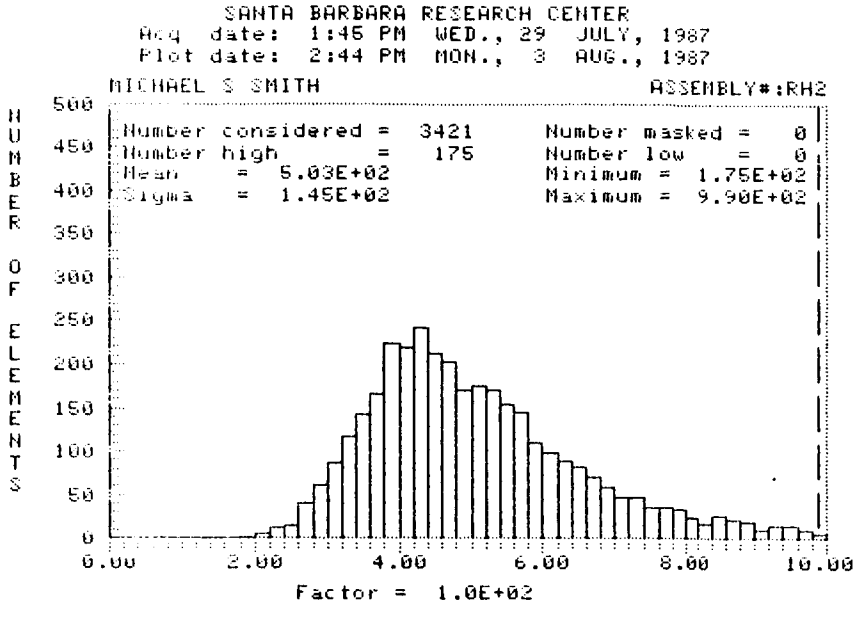

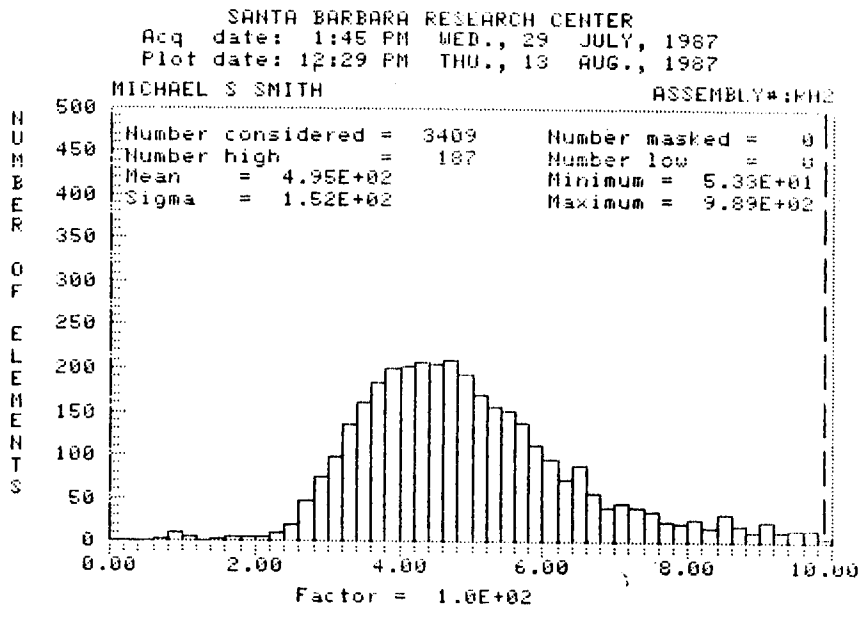

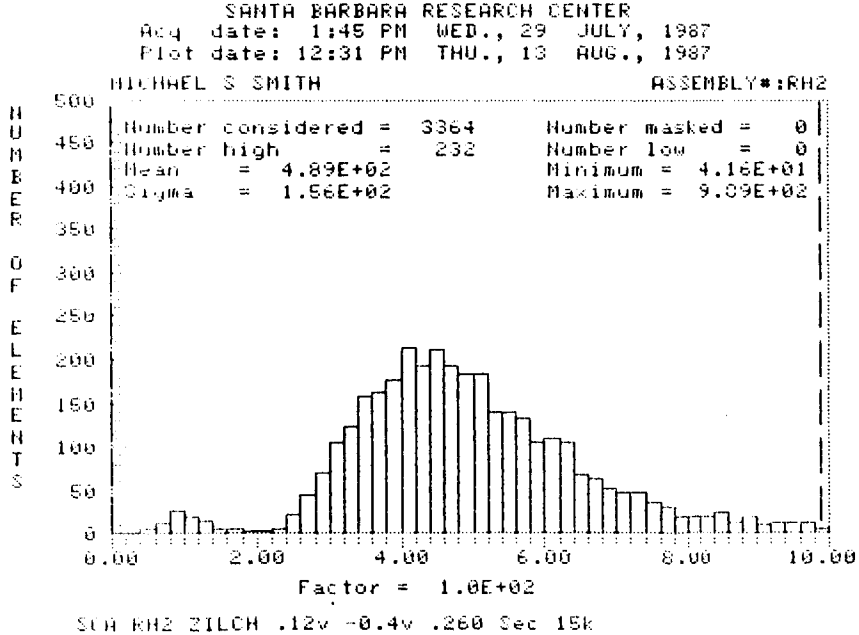

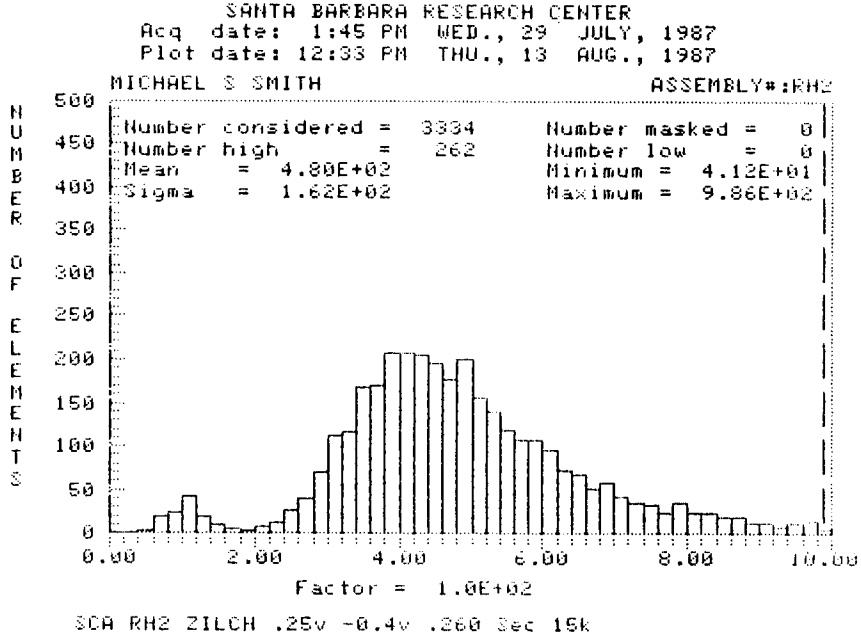

Figure A-14 Histograms of RH2 15K Noise Electrons

APPENDIX B

SBRC Low-Doped InSb Array RH4 Test Data Histograms

Test Data Histograms

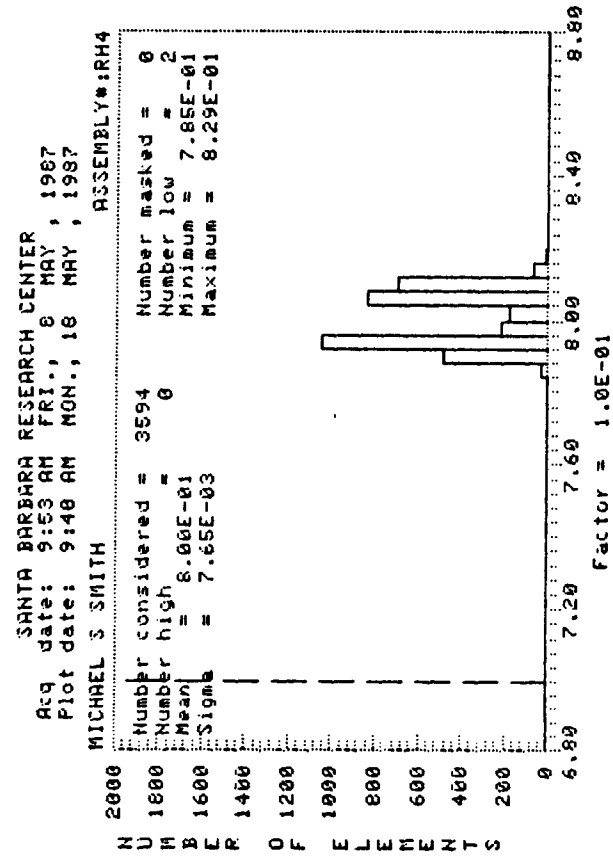

Figure B-1 Histograms of RH4 10K Source Follower Gain

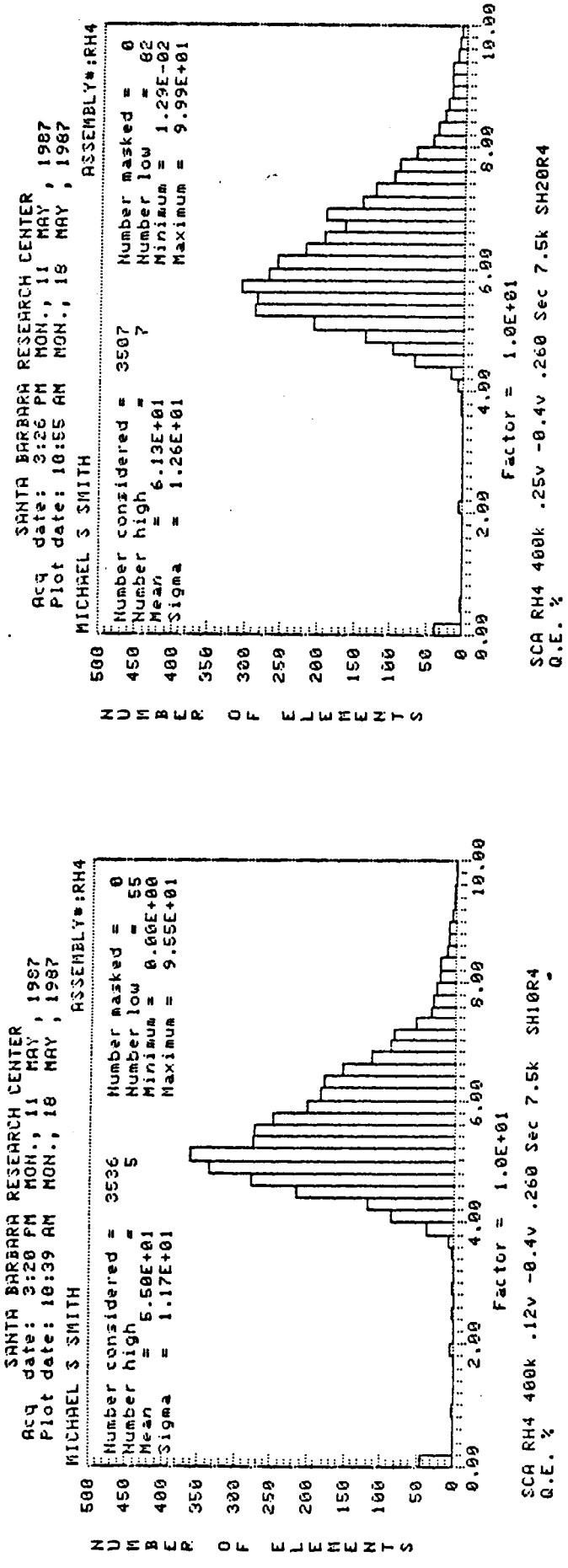

Figure B-2 Histograms of RH4 10K Quantum Efficiency

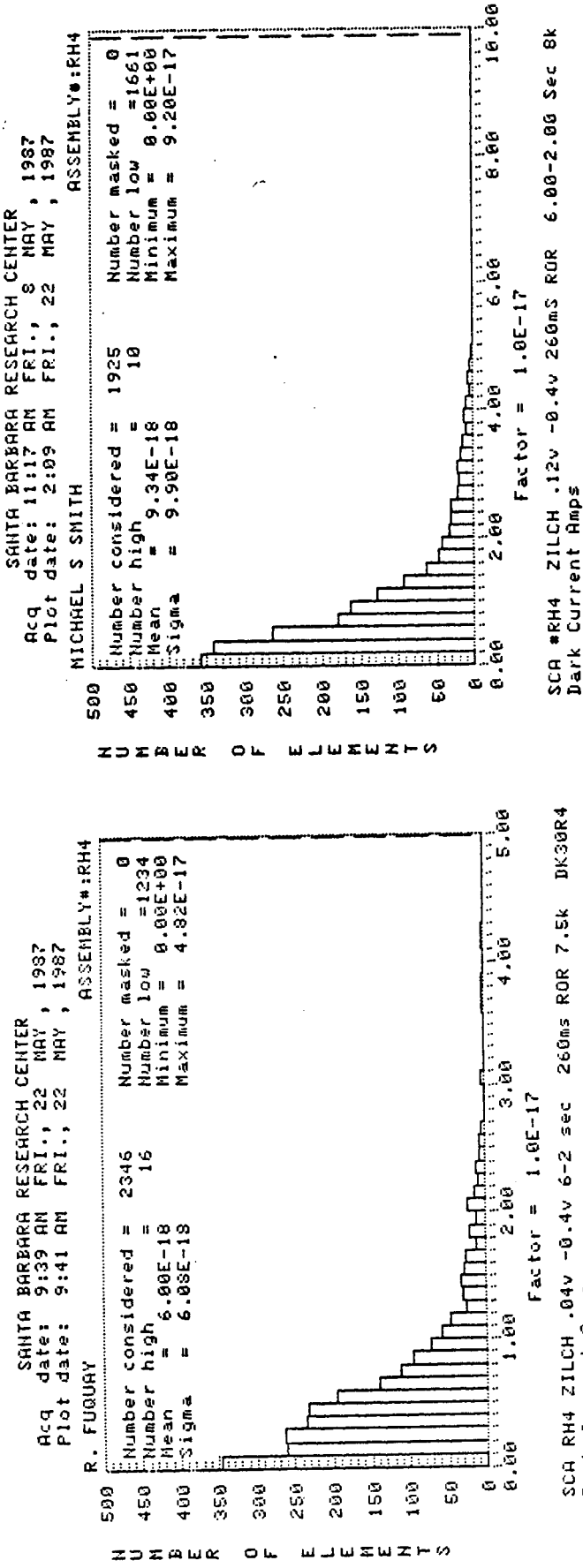

Figure B-3 Histograms of RH4 10K Dark Current - Burst Mode

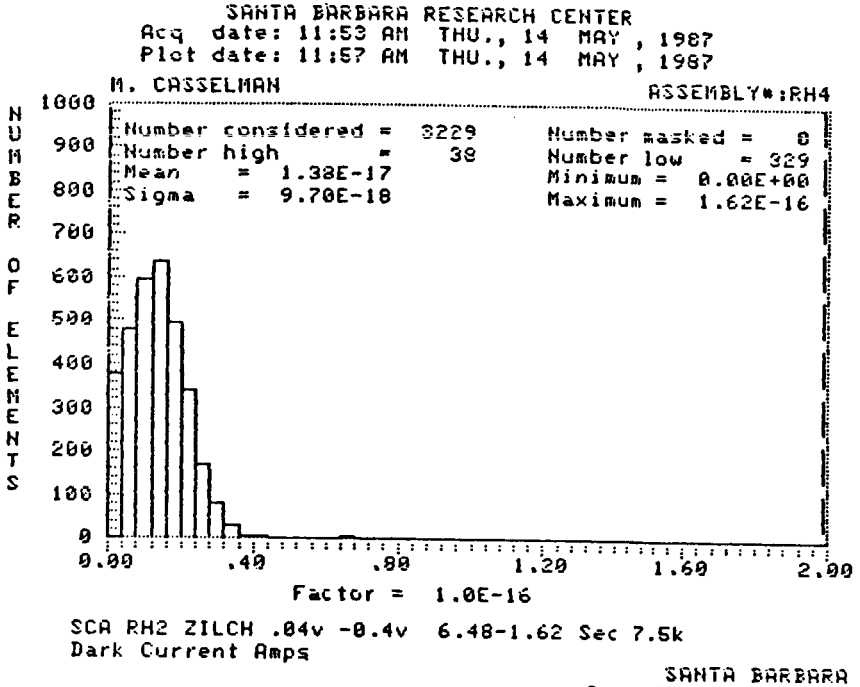

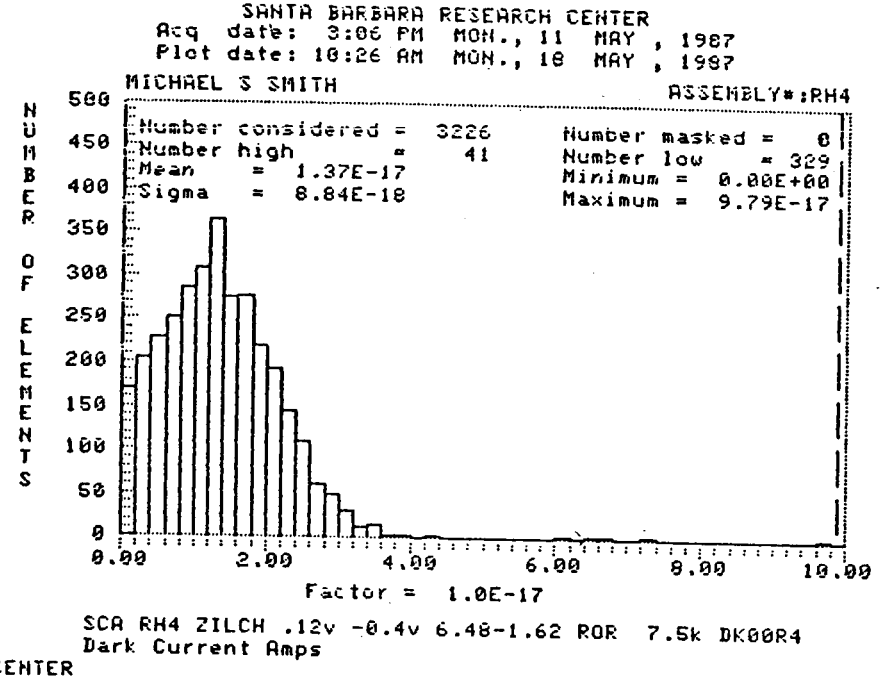

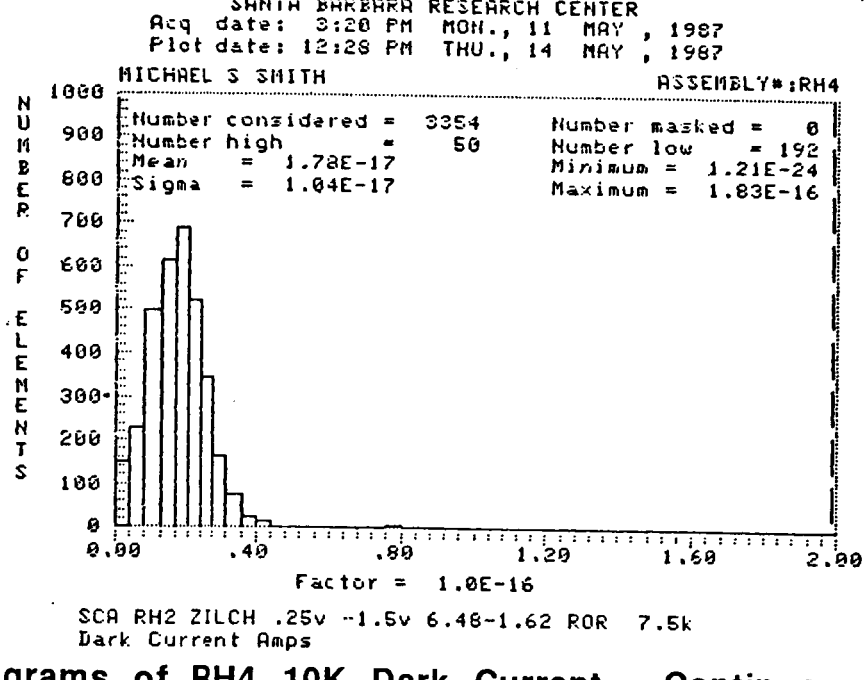

Figure B-4 Histograms of RH4 10K Dark Current - Continuous Mode, 0-2 Scaling

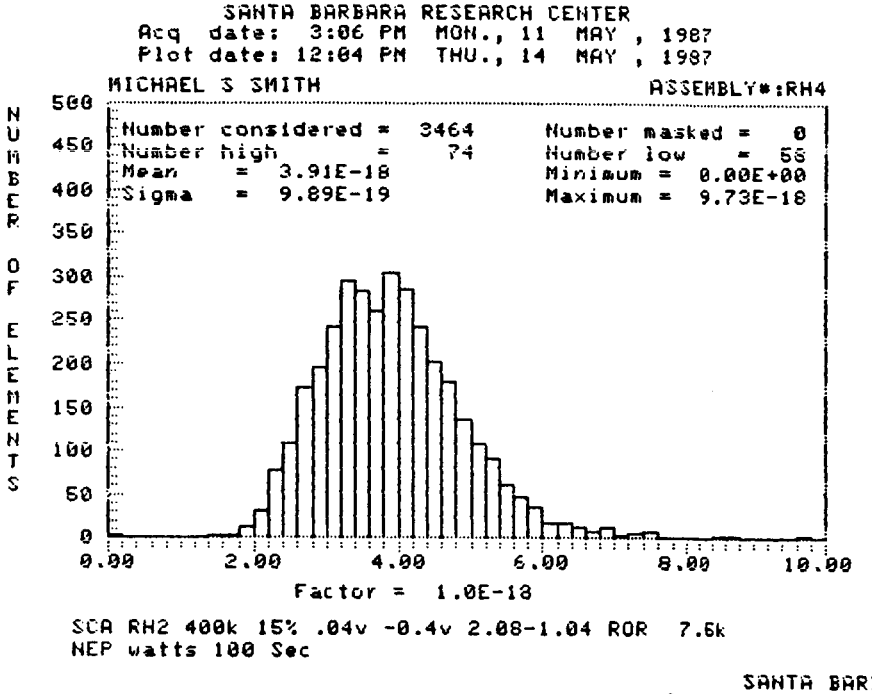

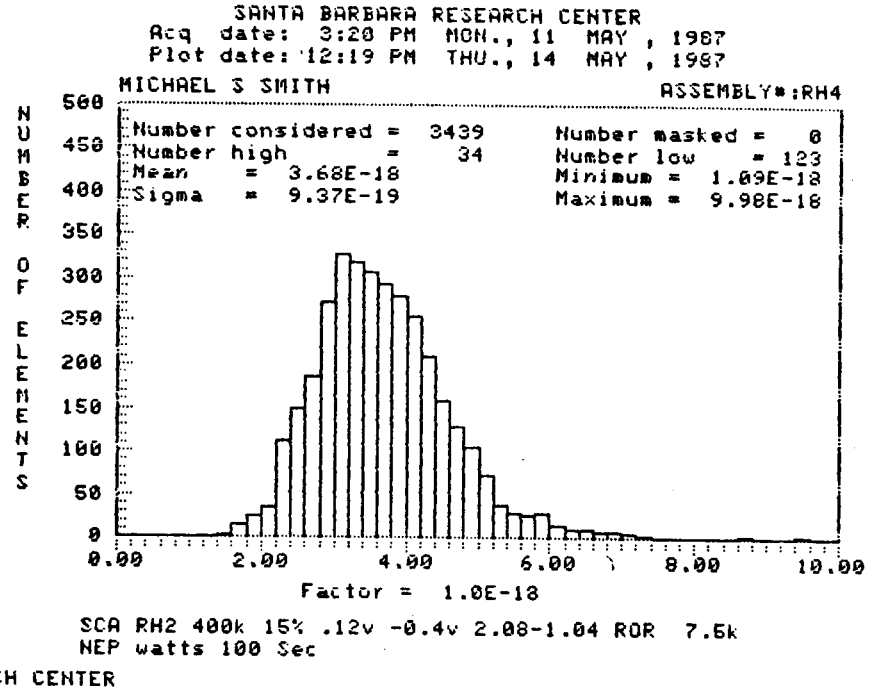

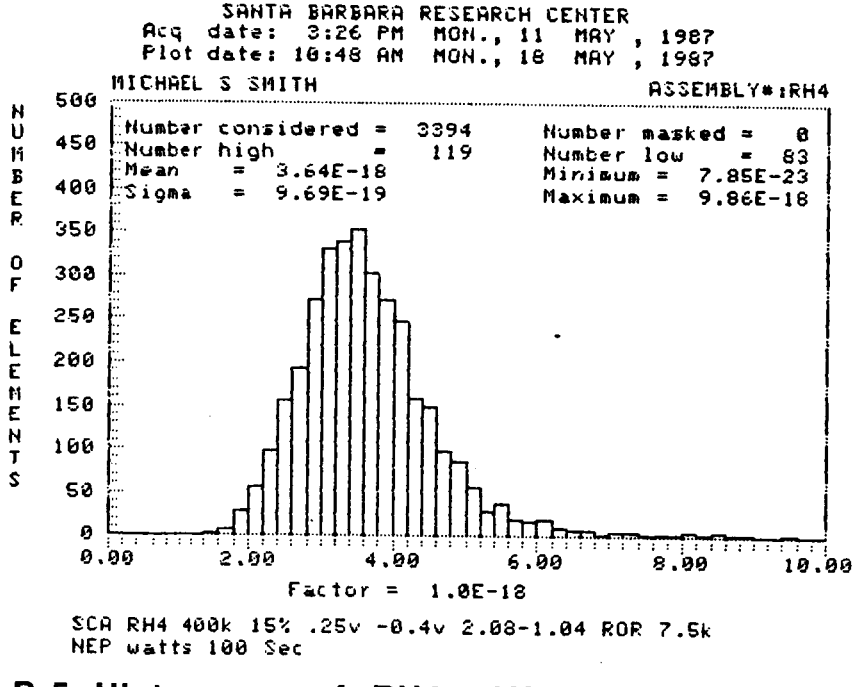

Figure B-5 Histograms of RH4 10K Noise Equivalent Power

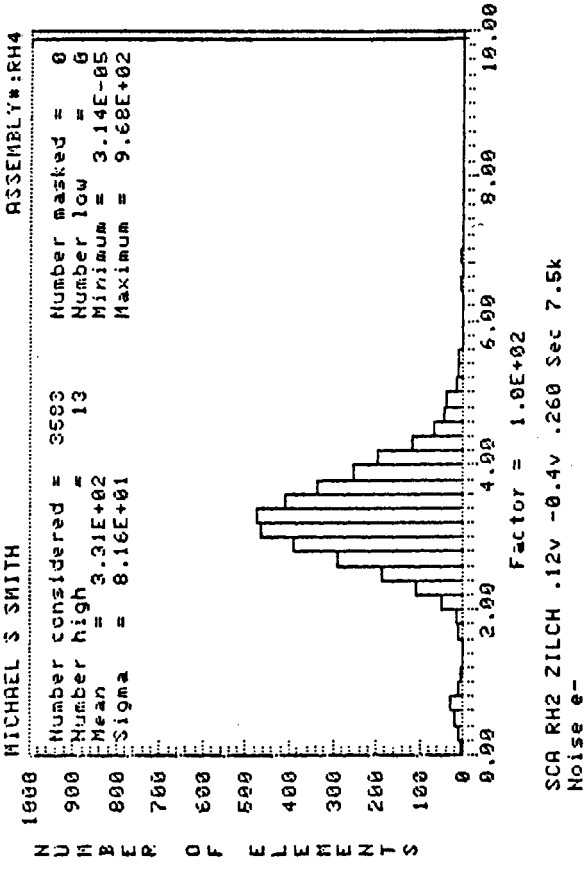

Figure B-6 Histograms of RH4 10K Noise Electrons

APPENDIX C

University of Arizona Test Facilities

II MID INFRARED SPECTROPHOTOMETER

For the beamsplitter measurements from 2 to 30 microns we arranged for the use of the National Optical Astronomy Observatories (NOAO) Beckman Acculab 6 Dual Beam Spectrophotometer. This spectrometer is a grating instrument specifically designed for room temperature transmission measurements. By rapidly "chopping" between the beam through the sample and a beam bypassing the sample and nulling the difference with a servo controlled aperture on the bypassed beam, the unit provides percent transmission measurements as a function of wavelength, relativity immune from drifts in source strength, detector sensitivity and amplifier gain.

Figure 1 shows the optical diagram of the Beckman Acculab 6 Spectrophotometer. The beamsplitter sample goes in the sample beam near the center line of the sample well. M12 is a movable mirror which permits directing the beam outside the spectrophotometer for use as a monochrometer. Figure 2 shows an unfolded ray diagram of the spectrophotometer in the vertical aspect. In the horizontal aspect, the beam size at the sample and slits S1 and S2 is considerably smaller. This diagram is unfolded in that it shows all reflecting elements as normal incidence transmitting elements.

The characteristics of the Acculab 6 are given in Table 1.

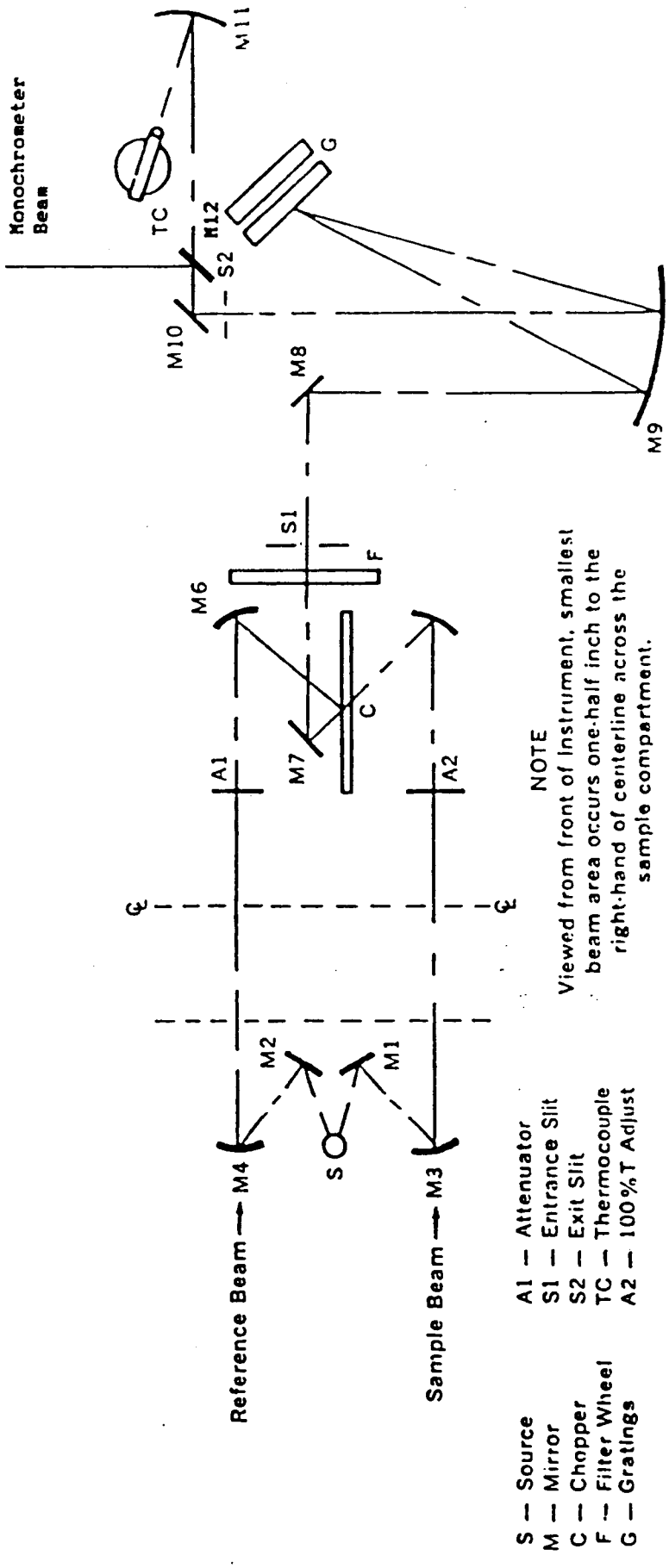

Optical Diagram of AccuLab 6

Figure 1.

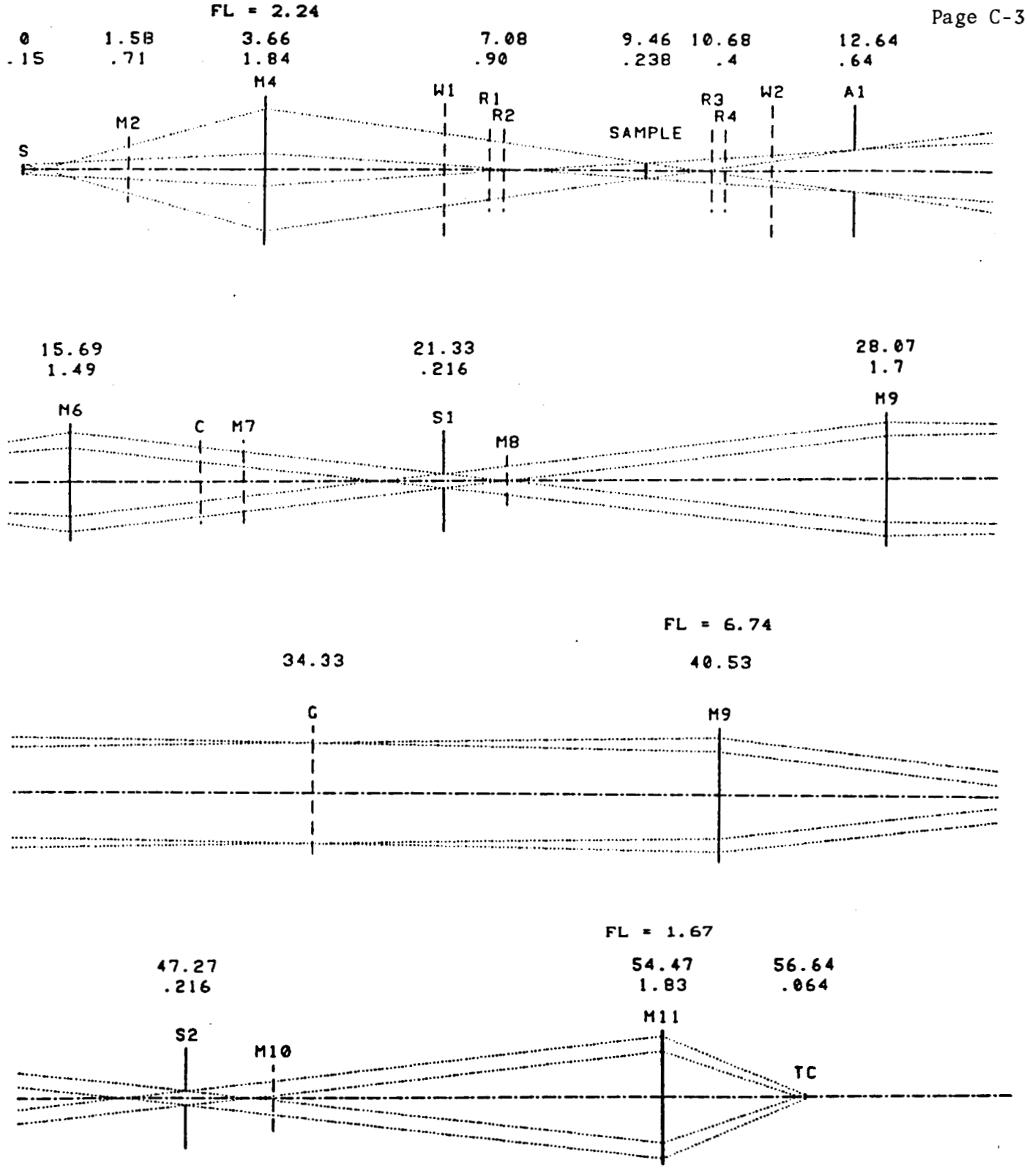

(DIMENSIONS IN INCHES - DISTANCE FROM SOURCE AND VERTICAL SIZE GIVEN)

BECKMAN ACCULAB 6 RAY DIAGRAM

VERTICAL UNFOLDED DUAL BEAM MODE

Figure 2.

TABLE 1 BECKMAN ACCULAB 6 SPECIFICATIONS

Spectral Range	4000 to 250 cm^{-1}
%T Range	0 to 100%T on integral recorder. Any desired portion of the 0 to 100%T range with span of 10%T or greater may be selected for expansion to fullscale on a 100-mv auxiliary recorder.
Scan Times	3.2, 9.5, or 28 minutes (60 Hz) 3.8, 11.4 or 34.2 minutes (50 Hz)
AccuSet Meter	Yes
Ordinate Expansion for Auxiliary Recorder	Yes
Purge Fitting	Yes
Weight	75 pounds
Wavenumber Accuracy	Better than 10 cm^{-1}, 4000 to 2000 cm^{-1} Better than 5 cm^{-1}, 2000 to 250 cm^{-1}
Wavenumber Repeatability	Better than 5 cm^{-1}, 4000 to 2000 cm^{-1} Better than 3 cm^{-1}, 2000 to 250 cm^{-1}
Resolution	Better than 5 cm^{-1} at 3000 cm^{-1} Better than 3 cm^{-1} at 1000 cm^{-1}
Slit Control	Two Programs: routine and high-resolution
Double-Beam 100% Line	±2%, 4000 to 600 cm^{-1}, excluding atmospheric absorption bands. ±3%, 600 to 300 cm^{-1}, excluding atmospheric absorption bands.
Formatted Chart Paper Presentation	5" x 13¾" grid 4¼" x 11" grid notebook (Optional)
Monochromator	1 rotating wedge filter, 100 line/mm and 40 line/mm gratings
Stray Light	Less than 1%, 4000 to 650 cm^{-1} Less than 3%, 600 to 300 cm^{-1}

OPERATING MODES
Automatic recording; double-beam optical null; linear transmittance versus linear wavenumber.
Linear transmittance versus time, at fixed wavenumber.

%T ACCURACY
Better than ±2%.

%T REPEATABILITY
Better than 1%.

SOURCE
Nichrome wire.

RECORDER
Flatbed, strip-chart. Repeating format.
Optional notebook-size format available.

CHART PRESENTATION
Percent transmission versus linear cm^{-1}.

DIMENSIONS
26 inches wide; 11 inches high; 24 inches deep.

RECOMMENDED OPERATING ENVIRONMENT
Less than 80% relative humidity; 15°C to 40°C.

III BEAMSPLITTER TEST CRYOSTAT

Since the beamsplitters must be tested at liquid helium temperature, it was necessary to design a cryostat for holding the beamsplitter samples which was compatible with the spectrophotometer sample wall.

We have therefore designed and constructed a beamsplitter test cryostat satisfying the following constraints. Two of the requirements, measuring reflection and measuring beyond 30 microns with a Fourier Transform Spectrometer, were added after the initiation of this contract.

- Sample temperature at room temperature and at ~ 15K
- Compatible with spectrophotometer sample well
- Compatible with fourier transform spectrometer sample area
- Test sample at 0° or 45° incident angle
- Sample size to 1 1/2 inch diameter
- Measure transmission and reflection
- Switch from sample to open (transmission) or gold reference mirror (reflection) to determine instrument baseline
- maintain reference mirror co-planar with sample

The cryostat was designed as a square addition to an existing Infrared Laboratories HR 8 vapor cooled radiation shield, liquid helium dewar.

During this contract the transmission only configuration was completed and successfully tested. The design changes for the reflection configuration were initiated.

Figure 3 shows the test dewar, transmission configuration for 45° incidence angle. The geometry is arranged so that the lower part of the dewar sits in the spectrophotometer sample well with the windows aligned with the spectrophotometer sample beam and the beamsplitter sample holder located at the spectrophotometer beam waist. In the direction into the paper, the windows and paddle are offset so that the dewar case clears the nearby spectrophotometer reference beam.

The dewar case windows are 1 inch diameter 2mm thick KRS5. The sample area and mechanism are enclosed in a helium temperature shield to maintain the low temperature of the sample holder. The interior surface of this shield is painted with Primer (3M Nextel Primer #911-P4 Light Grey) and black paint (3M ECP-2200 Solar Absorber Coating) to absorb the radiation entering through the dewar window. The inside of the dewar case, both sides of the vapor cooled shield and the outside of the helium shield are coated with aluminum foil. The vapor cooled shield and inner shield openings have baffle plates with openings approximately 1/8 inch x 1/2 inch.

Not shown is a mechanical feed-through mechanism which rotates the paddle in and out of the spectrophotometry beam. The support post and paddle have a second monitoring position for 0° incident angle.

The electrical header connects to seven temperature sensors listed in Table 2.

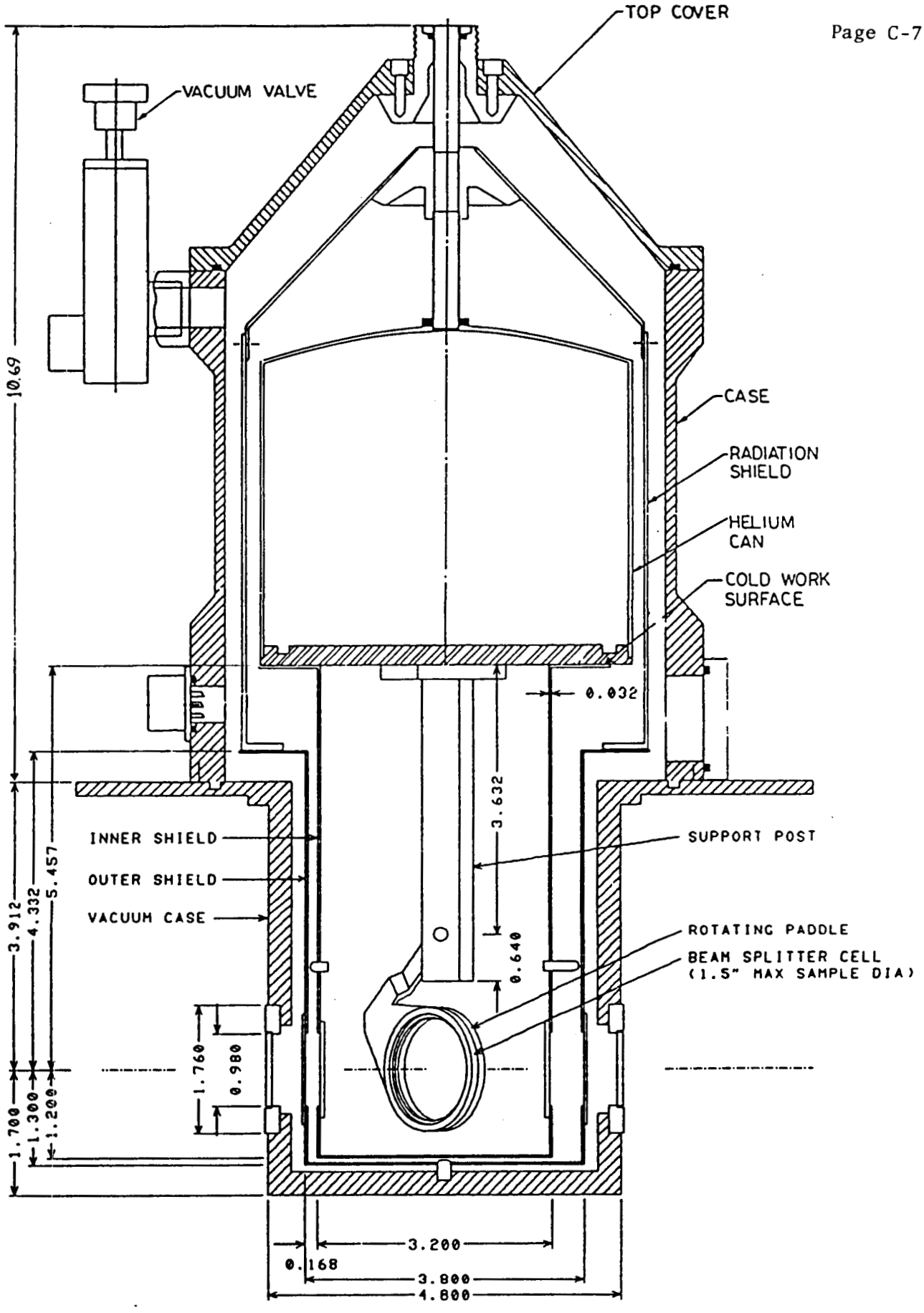

BEAM SPLITTER TEST DEWAR
45 DEGREE TRANSMISSION CONFIGURATION

Figure 3.

TABLE 2 TEMPERATURE SENSORS

Location	Type
1. Sample	Resistor (1K 1/8W Allen Bradley)
2. Sample Cell	"
3. Paddle	"
4. Post	"
5. Cold Work Surface	"
6. Inner Radiation Shield	Diode (1N4002)
7. Outer (Vapor Cooled) Radiation Shield	"

Figure 4 shows the dewar cool-down, with liquid helium after precooling with liquid nitrogen. The sample reaches equilibrium in 1 1/2 hours. The radiation shield takes ~ four hours to stabilize. The hold time after the second LHe fill is eight to twelve hours depending on the number of manipulations of the feed through mechanism and the time under the thermal load of the spectrophotometer beam.

Figure 5 shows the detailed thermal performance with a fused silica sample in the sample holder. The sample cooled to 7°K whether it was in or out of room temperature radiation entering the dewar. Its temperature rose to 14 degrees when exposed to the spectrophotometer beam.

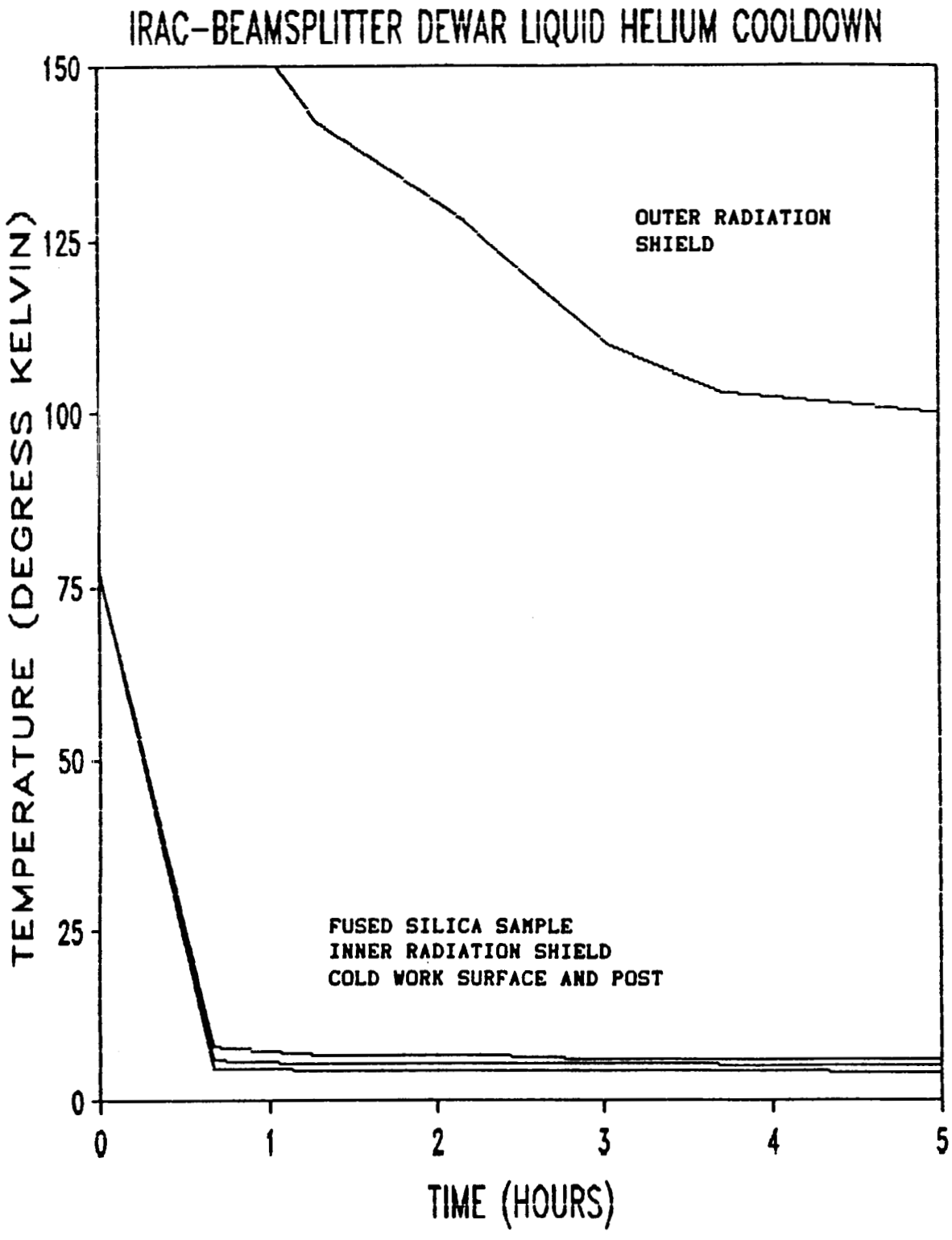
IRAC-BEAMSPLITTER DEWAR LIQUID HELIUM COOLDOWN
TEMPERATURE (DEGRESS KELVIN)
150
125
100
75
50
25
0
0
1
2
3
4
5
TIME (HOURS)
OUTER RADIATION SHIELD
FUSED SILICA SAMPLE
INNER RADIATION SHIELD
COLD WORK SURFACE AND POST

Figure 4.

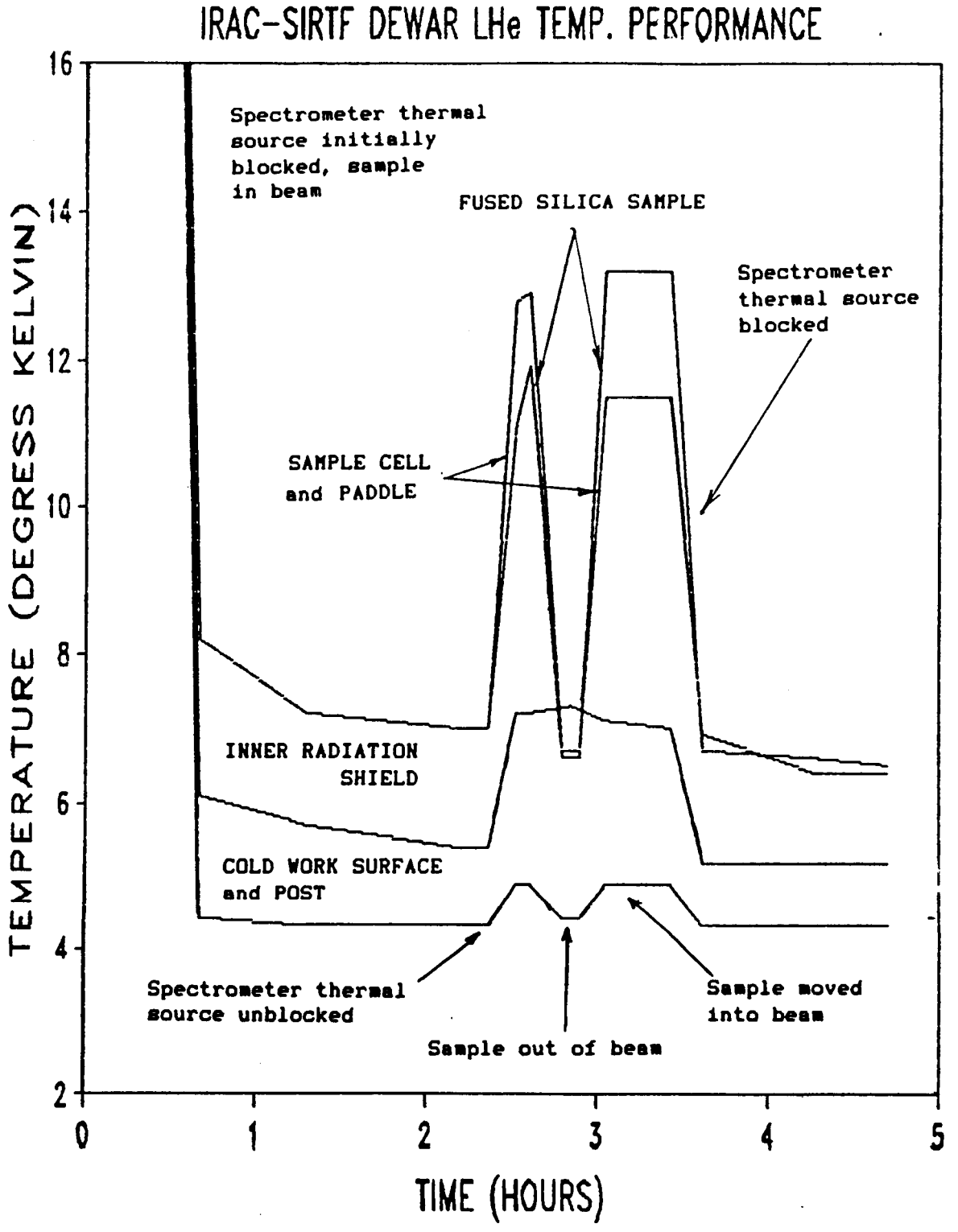
IRAC-SIRTF DEWAR LHe TEMP. PERFORMANCE
TEMPERATURE (DEGRESS KELVIN)
TIME (HOURS)
16
14
12
10
8
6
4
2
0
1
2
3
4
5
Spectrometer thermal source initially blocked, sample in beam
FUSED SILICA SAMPLE
Spectrometer thermal source blocked
SAMPLE CELL and PADDLE
INNER RADIATION SHIELD
COLD WORK SURFACE and POST
Spectrometer thermal source unblocked
Sample out of beam
Sample moved into beam

Figure 5.